LIGHT-ABSORPTION PROPERTIES OF COMBUSTION BROWN CARBON

by

ZEZHEN CHENG

(Under the Direction of Rawad Saleh)

ABSTRACT

Brown carbon (BrC) have significant but poorly constrained impacts on the climate. The major source of BrC is incomplete combustion of biomass fuels, where the combustion conditions (temperature and air-to-fuel ratio) are poorly controlled, leading to large variations in reported BrC light-absorption properties. In order to investigate the dependence of BrC light-absorption properties on combustion conditions, we performed controlled combustion experiments with model fuels (toluene and benzene) and obtained the mass absorption cross-section (MAC) and absorption Ångström exponent (AAE) of the BrC emissions at different combustion conditions. We found that more efficient combustion (higher temperature and/or higher air-to-fuel ratio) generated more absorptive (darker) BrC. Furthermore, regardless of fuel type and combustion conditions, the emitted aerosols exhibited a unified continuum of light-absorption properties that can be characterized by MAC at 532 nm ($MAC_{532}$) and AAE pairs. The pairs were well-correlated with the elemental carbon-to-organic carbon ratio (EC/OC), which is a proxy of combustion conditions.

BrC is subject to atmospheric processing by gas-phase oxidants such as the nitrate radical ($NO_3$). We investigated the evolution of chemical composition and light-absorption properties of BrC due

to heterogeneous reaction with $NO_3$. We generated BrC from the controlled combustion of toluene and oxidized it with $NO_3$ in an oxidation flow reactor. We found that the heterogeneous reaction of BrC with $NO_3$ led to significantly enhance BrC light absorption by the addition of chromophoric functional groups (e.g., nitro group). However, condensation of gas-phase PAH+$NO_3$ oxidation products that were less-absorbing than the particulate PAHs can counterbalance this enhancement.

Differences in online and offline optical measurement approaches could also lead to discrepancies between different studies. We generated BrC with variable light-absorption properties from the controlled combustion of toluene, isooctane, and cyclohexane, and compared the light-absorption properties of BrC aerosol retrieved from online method with those of their methanol and dichloromethane (DCM) extracts retrieved from offline method. We found that the DCM has higher extraction efficiency than methanol for the same BrC aerosols since DCM can extract more mass and darker BrC aerosol. Furthermore, we found that solvent-extraction techniques can substantially underestimate BrC light-absorption properties.

INDEX WORDS: Aerosols, combustion emissions, Brown carbon, PAHs, Nitro-PAHs, light-absorption properties, heterogeneous reaction, solvent-extraction

# LIGHT-ABSORPTION PROPERTIES OF COMBUSTION BROWN CARBON

by

ZEZHEN CHENG

B.S., Ohio State University, 2014

M.Che.E., Carnegie Mellon University, 2015

A Dissertation Submitted to the Graduate Faculty of The University of Georgia in Partial Fulfillment of the Requirements for the Degree

DOCTOR OF PHILOSOPHY

ATHENS, GEORGIA

2020

LIGHT-ABSORPTION PROPERTIES OF COMBUSTION BROWN CARBON

by

ZEZHEN CHENG

| | |
|---|---|
| Major Professor: | Rawad Saleh |
| Committee: | Brandon Rotavera |
| | Geoffrey Smith |
| | Jim Kastner |

Electronic Version Approved:

Ron Walcott
Interim Dean of the Graduate School
The University of Georgia
August 2020

# DEDICATION

To my beloved grandfather, who passed away in July 2018.

ACKNOWLEDGEMENTS

First and foremost, I would like to express my sincere gratitude to my major professor Dr. Rawad Saleh for his guidance, mentorship, and support during my doctoral study. I greatly appreciate the amount of time he has taken out for training me in multiple aspects such as instruments operation and maintenance, designing and conducting experiments, writing manuscripts, and presentation skills. Besides these solid skills, he all spends lots of time to help me form good study and research habits and the rigorous research attitude. With his profound knowledge and extreme patience, he led me out of every research bottleneck and encouraged me to continue my research work during my Ph.D. period. Without his guidance, this dissertation would not have been possible.

I sincerely thank my committee members, Dr. Brandon Rotavera, Dr. Geoffrey Smith, and Jim Kastner, for their guidance and encouragement in carrying out this project.

I also wish to express my gratitude to all the lab members who rendered their help during my research and made the lab environment cheerful and happy to work in.

Finally, I would like to thank my family for their long-lasting and selfless support.

TABLE OF CONTENTS

Page

LIST OF FIGURES

Page

# CHAPTER 1

# INTRODUCTION

## 1.1 background

Carbonaceous aerosols, including black carbon (BC) and organic aerosol (OA), account for a large fraction of atmospheric aerosols and have significant but poorly constrained impacts on the climate (Bond et al. 2013; Saleh 2020; Lin et al. 2015). BC, commonly known as soot, absorbs solar radiation efficiently, from ultraviolet (UV) into infrared (IR) (Bond and Bergstrom 2006; Moosmüller et al. 2009), and has been established as a leading climate-warming agent, potentially second only to $CO_2$ (Bond et al. 2013; IPCC 2013; Jacobson 2001). The OA interaction with solar radiation and its impacts on the climate are more complicated than those of BC. Most OA efficiently scatters visible radiation and absorbs IR and UV radiation strongly but are relatively nonabsorbing in visible (vis, 400−700 nm) and near-IR (700− 2500 nm) wavelengths, causing an overall cooling effect (Laskin, Laskin, and Nizkorodov 2015). However, some OA species absorb solar radiation efficiently in the near-UV (300−400 nm) and visible ranges and are dubbed brown carbon (BrC) (Andreae and Gelencsér 2006). This has been confirmed by numerous laboratory experiments (e.g., Saleh et al. 2014; Xie et al. 2017; Chakrabarty et al. 2010; Adler et al. 2019; Olson et al. 2015), field measurements (e.g., Kirchstetter et al. 2004; Lack et al. 2012; Devi et al. 2016; Zhang et al. 2017; Shamjad et al. 2016), and remote-sensing observations (e.g., Arola et al. 2011; Bahadur et al. 2012; Jethva et al. 2011; Wang et al. 2013; Zhang et al. 2017). Thus, BrC

plays a vital role alongside BC in the absorption of solar radiation by carbonaceous aerosols (Laskin, Laskin, and Nizkorodov 2015; Saleh 2020). Consequently, the radiative effect of light absorption by BrC has been the focus of several global-climate calculations (e.g., Saleh et al. 2015; Wang et al. 2014; Feng et al. 2013; Zhang et al. 2017; Brown et al. 2018), which have revealed a potentially important, yet highly uncertain radiative effect associated with BrC light absorption, with global-mean values ranging between +0.03 W $m^{-2}$ and +0.57 W $m^{-2}$ (Saleh 2020). This large variability is in part a manifestation of the limited understanding of the formation pathways, chemical nature, and atmospheric processing of BrC (Laskin, Laskin, and Nizkorodov 2015). In addition to the true variability outlined above, there are also differences in optical measurement approaches that have been applied in the literature, which could lead to discrepancies between different studies (Moosmüller, Chakrabarty, and Arnott 2009). All of the above hinder explicit representation of the wide range of experimentally derived BrC light-absorption properties within a climate-modeling framework.

### 1.2. Sources of Brown Carbon

On the global scale, incomplete combustion of biomass, including open-biomass burning (e.g., large-scale forest and savanna fires) and solid-biofuel burning (e.g., wood and other biofuels for heating, cooking, and energy), is the major source of atmospheric BrC (Ramanathan et al. 2007; Zhang et al. 2017; Wang et al. 2016; Xie et al. 2018; Washenfelder et al. 2015). Moreover, some studies have found that incomplete combustion of fossil fuels, such as low-efficiency residential coal combustion (Du et al. 2014a, 2014b; Yan et al. 2018; Yan et al. 2017) and heavy-fuel-oil (HFO) combustion in ship engines (Corbin et al. 2019, 2018), is also a significant source of BrC. Although biomass-combustion BrC has a higher contribution to the global BrC budget than fossil-

fuel combustion BrC, that does not imply that the chemical composition of biomass fuels is more conducive for BrC formation. The key to explain this discrepancy is combustion conditions, generally governed by the combustion temperature and air-fuel ratio (AFR) (Turns 2000). Biomass combustion is conducive for the formation of BrC because it is typically under relatively low-temperature fuel-rich combustion conditions (Saleh et al. 2014; Chen and Bond 2010). On the other hand, the combustion conditions at which fossil fuels are burned are usually designed to be more efficient than those of biomass combustion (e.g., higher combustion temperature and more fuel-lean). Such combustion conditions are less conducive for BrC formation. Therefore, the quantity of BrC emitted from combustion largely depends on combustion conditions (combustion temperature and AFR). Even with biomass fuels, the light-absorption properties of combustion BrC have been shown to vary significantly with combustion conditions (Chen and Bond 2010; Saleh et al. 2014; Martinsson et al. 2015; ). The combustion temperature and AFR are challenging to quantify in the real-life uncontrolled combustion that usually produces a mixture of BrC and BC. To overcome this, previous studies have resorted to proxies to indirectly characterize the combustion conditions, including the relative abundance of elemental carbon (EC) and organic carbon (OC) in the particulate emissions (Vicente et al. 2015; Chen et al. 2014; Shen et al. 2012; Stockwell et al. 2016; Hong et al. 2017) that higher EC-to-OC ratio (EC/OC) indicates more efficient combustion. Values of EC/OC reported in the literature for uncontrolled biomass combustion are highly variable (Olson et al. 2015; Roden et al. 2006; Yang et al. 2009; Chen et al. 2014; Bauer et al. 2009; Zhang et al. 2013; Akagi et al. 2011), underscoring the diversity in combustion conditions. EC/OC (Xie, Hays, and Holder 2017; Pokhrel et al. 2016) and BC/OA (Saleh et al. 2014) have been utilized to parameterize the optical properties of combustion carbonaceous aerosols. While EC and BC have different operational definitions that depend on the

measurement method, they are closely related and are often used interchangeably (Watson et al. 2005).

In addition to primary BrC emissions, BrC are also associated with secondary organic aerosol (SOA) from biogenic and anthropogenic precursors (Laskin et al. 2015; Lambe et al. 2013; Rizzo et al. 2011, 2013; Updyke et al. 2012). Oxidation of aromatic VOC precursors (e.g., benzene, toluene), usually generated from combustion, generate secondary BrC (Zhong and Jang 2011; Updyke et al. 2012; Dingle et al. 2019). High-NOx photooxidation (e.g., α-pinene/OH/NOx) and ozonolysis (α-pinene/O3) of biogenic precursors (e.g., α-pinene, *d*-limonene) (Nakayama et al. 2013; Nakayama et al. 2010; Flores et al. 2014) of biogenic precursors (e.g., α-pinene, *d*-limonene) generate SOA that is typically is non- or less absorbing (Dingle et al. 2019; He et al. 2018). These biogenetic SOA might be further oxidized by exposure to ammonia, amines, and amino acids to generate secondary BrC (Flores et al. 2014; Lee et al. 2014; Bones et al. 2010). Secondary BrC also forms in cloud and fog droplets through aqueous oxidation and oligomerization of α-dicarbonyls (e.g., glyoxal (GL) and methylglyoxal (MG)) (De Haan et al. 2017; Kampf et al. 2016; Marrero-Ortiz et al. 2019; Lin et al. 2015), polycyclic aromatic hydrocarbons (PAHs) (i.e., naphthalene and anthracene) (Haynes, Miller, and Majestic 2019), and other organic compounds (e.g., phenols) released during biomass burning (Gilardoni et al. 2016; Gelencsér et al. 2003; Hoffer et al. 2004; Sun et al. 2010). Secondary BrC can also be generated through nitrate oxidation of gas-phase and particle-phase PAHs (Lin et al. 2017; C. Li, He, Hettiyadura, et al. 2019; Lu et al. 2011).

### 1.3. Chemical Composition of Brown Carbon

The relationship between the chemical composition and optical properties of BrC remains limited due to the complexity of BrC chemical composition. Atmospheric BrC has been often associated with the broad family of humic-like substances (HULIS) (Pöschl 2005; Hoffer et al. 2006; Dinar et al. 2007; Utry et al. 2013; Y. Wang et al. 2019). This is rooted in a study by Mukai and Ambe (1986), who identified brown airborne particles originating from biomass burning and found that their chemical signatures were similar to humic acids. Mukai and Ambe (1986) suggested that the structure of HULIS contains polycyclic rings with hydrocarbon side chains containing hydroxyl, carboxyl, and carbonyl groups. Furthermore, there are more recent studies (Claeys et al. 2012; Kahnt et al. 2013; Lin, Engling, and Yu 2010; Lin et al. 2012) on the chemical composition of atmospheric HULIS reported presence of relatively small organic molecules (e.g., nitrocatechols, aromatic carboxylic acids, terpenoid acids, and nitrooxy organosulfates). HULIS can be formed by biomass burning or decomposition, as well as aqueous in-cloud processing and oligomerization of water-soluble organics (Andreae and Gelencsér 2006; Graber and Rudich 2006).

Another broad term, tar balls, was introduced by Posfai et al. (2004) and has been used to designate a prominent type of largely homogeneous BrC particles commonly detected in smoke emissions from incomplete combustion of biomass (Chakrabarty et al. 2010; Adachi and Buseck 2011; Alexander, Crozier, and Anderson 2008; China et al. 2013). Tar balls have a unique spherical morphology and are stable under the electron beam and high vacuum of a transmission electron microscope (TEM) (Chakrabarty et al. 2010; Hoffer et al. 2016; Tóth et al. 2014).

HULIS and tar balls are not necessarily incompatible. X-ray spectro-microscopy analysis of tar balls showed that their spectral and chemical characteristics were similar to the characteristic

properties of HULIS (Hopkins et al. 2007; Tivanski et al. 2007). Moreover, BrC chromophores in biomass-combustion emissions have been linked to charge transfer complexes (Phillips and Smith 2014) as well as aromatic species, including polycyclic aromatic hydrocarbons (PAHs) (Li, He, Schade et al. 2019; Adler et al. 2019) and oxygenated and nitrated aromatics ( Li, He, Schade et al. 2019; Lin et al. 2016; Liu et al. 2017; Desyaterik et al. 2013). Such chromophores have been identified both in HULIS (Dinar et al. 2007; Claeys et al. 2012; Wang et al. 2019) as well as tar balls (Li, He, Hettiyadura et al. 2019; Li, He, Schade et al. 2019). It has been shown that PAHs are major constituents of combustion BrC, especially the highly-absorptive fraction (Saleh et al. 2018; (Li, He, Hettiyadura et al. 2019; Li, He, Schade et al. 2019; Adler et al. 2019). This is not surprising since PAHs have been identified as key species in the soot-formation process by numerous fundamental laboratory studies (Michelsen 2017) and have been known to constitute a substantial fraction of combustion emissions of fossil (Karavalakis et al. 2011) and biomass (Shen et al. 2012) fuels.

### 1.4. Light-absorption Properties of Brown Carbon

The light-absorption properties of carbonaceous aerosols are usually quantified using the wavelength-dependent imaginary part of the refractive index (*k*) or the mass absorption cross-section (MAC). The literature suggested *k* and MAC at 550 nm for BC are 0.79 and 7.5±1.2 $m^2 g^{-1}$, respectively (Bond and Bergstrom 2006). Unlike BC, which has relatively well-constrained light-absorption properties, the BrC light-absorption properties reported in the literature are highly variable (Saleh 2020). The values of *k* at mid-visible wavelengths reported for BrC range over 3 orders of magnitude ($10^{-4}$ to $10^{-1}$) (Laskin, Laskin, and Nizkorodov 2015). BrC exhibits an increase in absorption with decreasing wavelength within the visible spectrum, which can be represented

using a power-law functional dependence on wavelength. Unlike BC, whose light absorption is weakly dependent on wavelength in the visible spectrum, the light absorption of BrC exhibits a stronger wavelength dependence. The values of the wavelength dependence of $k$ (i.e., the exponent of the power-law) is usually quantified in terms of the $w$. The values of $w$ of BrC $k$ (i.e., $k(\lambda) \sim \lambda^{-w}$) vary from ~1 to 10. For reference, the corresponding mid-visible MAC ($m^2\ g^{-1}$) values can be roughly approximated by multiplying the mid-visible $k$ by 10. Also, the wavelength dependence of MAC, the absorption Ångström exponent (AAE), can be approximated as $w + 1$ for particles much smaller than the wavelength. Saleh (2020) proposed an optical classification of BrC based on its $k$ at 550 nm ($k_{550}$) and $w$: very weakly absorbing BrC (VW-BrC) ($k_{550}=10^{-4}$-$10^{-3}$, $w$=6-9), weakly absorbing BrC (W-BrC) ($k_{550} = 10^{-3}$-$10^{-2}$, $w$ = 4-7), moderately absorbing BrC (M-BrC) ($k_{550} = 10^{-2}$-$10^{-1}$, $w$ = 1.5-4), and strongly absorbing BrC (S-BrC) ($k_{550} > 10^{-1}$, $w$ = 0.5-1.5). It is noteworthy that $k_{550}$ of VW-BrC and S-BrC are separated by 3 orders of magnitude and that the more absorptive BrC (larger $k_{550}$) is characterized by flatter absorption spectra (smaller $w$). Furthermore, there is a correlation between BrC sources and optical classes, with the more absorptive BrC (M-BrC and S-BrC) mostly associated with biomass combustion.

### 1.5. Atmospheric Processing of Brown Carbon

Despite the advances in identifying the chemical species that constitute BrC, a comprehensive picture of the landscape of BrC chemical structure is still lacking (Laskin, Laskin, and Nizkorodov 2015). Perhaps even more lacking is the understanding of the evolution of BrC upon chemical processing in the atmosphere, which has been the focus of numerous recent studies. The effects of atmospheric aging are complex and can either enhance or reduce light absorption by BrC (Laskin, Laskin, and Nizkorodov 2015). Both laboratory studies (Browne et al. 2019; Sumlin et al. 2017;

Zhao et al. 2015; Wong, Nenes, and Weber 2017) and field measurements (Satish et al. 2017; Dasari et al. 2019) have observed that photooxidation led to a reduction in BrC light absorption. This bleaching effect could be attributed to either dark or photo-initiated destruction of chromophores through OH oxidation.

On the other hand, the presence of $NO_x$ has been observed to enhance the BrC light absorption ( (Li, He, Hettiyadura et al. 2019; Li, He, Schade et al. 2019; Wang et al. 2019) or slow down the OH-induced bleaching effect (Zhong and Jang 2014; Nakayama et al. 2013). Another important, yet understudied, atmospheric reaction that can potentially contribute to the dynamic behavior of BrC light absorption is the nighttime reaction of PAHs with $NO_3$ (Keyte et al. 2013;). The large reaction rate coefficients (Mak et al. 2007) and rapid uptake of $NO_3$ on surfaces (Knopf, Forrester, and Slade 2011) suggest that $NO_3$ could induce heterogeneous oxidation of condensed-phase PAHs, leading to the formation of nitrogen-containing PAH derivatives, including nitro-PAHs. Studies of heterogeneous oxidation of single-compound PAHs (e.g., anthracene, pyrene, and benzo[a]pyrene) with $NO_2/NO_3/N_2O_5$ indicated that these reactions resulted in enhanced UV-visible absorption of the oxidized PAHs relative to their parent molecules (Kwamena and Abbatt 2008; Lu et al. 2011).

### 1.6. Biases in Brown Carbon Optical Measurements

In addition to the true variability in the light-absorption properties of BrC associated with the variability in the BrC formation pathway and chemical composition, some of the variability in the literature values is attributed to differences in measurement techniques and the associated biases and uncertainties (Moosmüller et al. 2009). Retrieval of *k* and *w* of BrC can be achieved via online aerosol optical measurements coupled with optical (e.g., Mie theory) calculations (Chakrabarty et

al. 2010; Saleh et al. 2013; Saleh et al. 2014; D. A. Lack et al. 2012) or offline methods involving filter collection and extraction with water or organic solvents followed by light-absorption measurements using ultraviolet-visible (UV-vis) spectrophotometry (Chen and Bond 2010; Li, Chen, and Bond 2016). The main advantage of the online methods is the ability to retrieve the optical properties of the BrC aerosol while airborne.

Photoacoustic spectroscopy (PAS) is a widely used online aerosol light-absorption properties measurement technique which has emerged as a technique that can directly measure the actual light absorption of suspended particles (Wiegand, Mathews, and Smith 2014; Fischer and Smith 2018). PAS is designed based on the photoacoustic effect, where particles absorb modulated light and convert radiation energy into thermal energy, and then release the thermal energy to heat the surrounding gas and generate pressure wave (Terhune and Anderson 1977). Microphones can detect these pressure waves, and the amplitude of the microphone signal is linearly proportional to the strength of absorption, which makes the PAS signal entirely insensitive for light scattering (Haisch 2012; Moosmüller et al. 1997; H. Lin and Campillo 1985; Sedlacek et al. 2008). This is one of the most important advantages of PAS technology. Additional to that, current PAS also has advantages of stability, reliability, fast time response (seconds to minutes), and low detection limit (<1 $Mm^{-1}$, approximately equal to 1 $\mu g/m^3$ black carbon concentration) (Fischer and Smith 2018; Wiegand, Mathews, and Smith 2014; Yu et al. 2019; Daniel A. Lack et al. 2006).

On the other hand, PAS instruments are typically limited in the number of wavelengths (typically 1 ~ 4 wavelengths) and spectral coverage (typically from ~400 to ~800 nm) (Lack et al. 2012; Linke et al. 2016; Lack and Langridge 2013; Liu et al. 2015). Moreover, the retrieval process is relatively complex. In the real-life, BrC is often co-emitted with black carbon (BC), induces

relatively large uncertainty because retrieval calculations require knowledge of the poorly constrained BC mixing state and morphology (Saleh 2020; Stevens and Dastoor 2019). Since BC is insoluble in water and organic solvents (T. C. Bond et al. 2013), aerosol researches apply the offline methods which can physically isolate the BrC via solvent extraction.

Traditionally, offline methods involving filter collection and extraction have been used to measure the light-absorption properties of BrC. These methods usually collect BrC aerosols over an extended period on the filters and then extract BrC aerosols from filters by solvents. The light absorption of the extracted BrC can be measured by Ultraviolet-visible (UV-vis) Spectroscopy (Phillips and Smith 2017; Chen and Bond 2010; Chen, and Bond 2016). Compared to the PAS method, the offline UV-vis method has advantages including simplicity, low price, and insensitivity to gaseous absorption and aerosol concentration. However, this method is limited to represent the average change in light absorption during a time course, rather than real-time change. Moreover, this method suffers from a bias associated with differences in the extraction efficiency of different solvents, thus the amount of chromophores present in the solution (Chen and Bond 2010; Liu et al. 2013). Not all types of BrC can be efficiently extracted in water and organic solvents (Corbin et al. 2019). Different types of BrC exhibit variable extraction efficiencies in different solvents leading to retrieved light-absorption properties that are solvent-dependent (Chen and Bond 2010; Liu et al. 2013; Shetty et al. 2019)

Traditionally, the most widely used solvent to extract organic aerosol (OA) in atmospheric science research is water (Hecobian et al. 2010; Claeys et al. 2012; Zhang et al. 2013). Realizing that a significant fraction of OA is not water-soluble, methanol has also been used as a solvent in more recent studies (Fuzzi and Decesari 2016; Xie et al. 2017; Xie, Hays, and Holder 2017; Phillips and

Smith 2017). Methanol is more effective at extracting OA, which exhibits a wide range of polarities (O'Brien et al. 2013; Hunter et al. 2017; Ditto et al. 2018), especially fresh combustion emissions (Y. Chen and Bond 2010; Sengupta et al. 2018), which are relatively non-polar. Consequently, for the same combustion emissions, *k* values retrieved for methanol-extracted BrC are larger than those for water-extracted BrC (Chen and Bond 2010; Wu et al. 2016). Although methanol has a higher OA extraction efficiency than water, its extraction efficiency is still limited, which can lead to underestimating OA light-absorption properties since unextracted fraction corresponds to the large-molecular-size BrC which have larger light-absorption properties (Saleh et al. 2014; Shetty et al. 2019). Thus, it is critical to find a more efficient extraction solvent. Although relatively uncommon in atmospheric aerosol studies, dichloromethane (DCM) is frequently used as a solvent in combustion soot-formation research due to its efficacy at extracting the large-molecular-size polycyclic aromatic hydrocarbons (PAHs) that constitute nascent soot (Alfè et al. 2008; Apicella et al. 2007; Faccinetto et al. 2015; Russo et al. 2013), which are important BrC components (Saleh et al. 2018; Cheng et al. 2020). BrC absorption (i.e., *k*) increases with increasing molecular size (Saleh et al. 2018) while its solubility decreases with increasing molecular size (Corbin et al. 2019). Therefore, offline solvent-extraction techniques are expected to underestimate BrC absorption as they miss the large-molecular-size S-BrC (Saleh 2020), which is poorly soluble or insoluble in organic solvents (Corbin et al. 2019). This is supported by the findings of Shetty et al. (2019) who reported that the extraction efficiency of biomass-burning BrC decreased with the increasing of BC/OA ratio, which is correlated with an increase in production of S-BrC (Cheng et al. 2019; Saleh 2020; Saleh et al. 2014).

### 1.7. Specific Objectives and Summary of Chapters

This dissertation aims to fill some of the important knowledge gaps of the optical properties of BrC, which will enable better representation of BrC in climate models. The main objectives of this dissertation are to 1) design controlled-combustion experiments where combustion conditions (relative flowrates of $O_2$, $N_2$, and fuel and combustion temperature) are varied systematically; 2) perform measurements to constrain the light-absorption properties of the combustion BrC and BrC-BC mixtures at different combustion conditions; 3) investigate the evolution of BrC light-absorption properties due to nighttime oxidation with $NO_3$; and 4) assess the bias associated with quantifying the light-absorption properties BrC using the solvent extraction method.

The dissertation is organized as follows:

In Chapter 2, controlled combustion experiments were performed to investigate the dependence of optical properties, described as the mass absorption cross-section (MAC) and absorption Ångström exponent (AAE), of combustion BrC emissions on combustion conditions. Using benzene and toluene as fuels, we obtained a wide range of combustion conditions by varying the combustion temperature and relative flowrates of $N_2$, $O_2$, and fuel. MAC and AAE were calculated from multi-wavelength light-absorption measurements using a photoacoustic spectrophotometer and aerosol mass loadings estimated from thermal-optical analysis. Starting with relatively low-temperature and fuel-rich combustion conditions and progressively increasing the temperature and/or decreasing the equivalence ratio, emissions were generated with progressive change from weakly absorbing brown carbon (BrC) (MAC at 532 nm ($MAC_{532}$) = 0.24 $m^2\ g^{-1}$ and AAE = 8.6) to strongly absorbing BrC ($MAC_{532}$ = 2.1 $m^2\ g^{-1}$ and AAE = 3.1) to mixtures of black carbon (BC) and strongly absorbing BrC ($MAC_{532}$ = 7.7 $m^2\ g^{-1}$ and AAE = 1.5). These findings indicate that

combustion conditions are important in dictating the light-absorption properties of the emitted aerosols. Furthermore, regardless of fuel type and combustion conditions, the emitted aerosols exhibit a unified continuum of light-absorption properties that can be characterized by $MAC_{532}$ and AAE pairs. The $MAC_{532}$ and AAE pairs are well-correlated with the elemental carbon-to-organic carbon ratio (EC/OC), which is a proxy of combustion conditions, confirming previous findings that EC/OC is a practical basis for parameterizing the light-absorption properties of combustion BrC.

In Chapter 3, the evolution of chemical composition and light-absorption properties of BrC due to atmospheric nighttime aging of BrC with $NO_3$ was investigated in a collaborative project with Aerodyne Research, Inc. We generated BrC from controlled combustion of toluene and oxidized it with $NO_3$ in an Aerodyne Potential Aerosol Mass oxidation flow reactor (OFR). Three types of BrC were studied, with varying light-absorption properties that were classified in terms of the imaginary part of the refractive index ($k$) as: light BrC ($k$ at 532 nm, $k_{532}$ = 0.008), medium BrC ($k_{532}$ = 0.026), and dark BrC ($k_{532}$ = 0.091). Exposure to $NO_3$ led to ~30% increase in $k_{532}$ of the light and medium BrC and ~5% decrease in $k_{532}$ of the dark BrC. This discrepancy is attributed to two competing effects: 1) the addition of chromophoric functional groups by heterogeneous oxidation and 2) condensation of gas-phase PAH+$NO_3$ oxidation products that were less-absorbing than the particulate PAHs. Analysis of the aerosol chemical evolution revealed that effect (2) was more important in the dark BrC experiments. I have performed optical calculations to isolate effect (1) and showed that heterogeneous oxidation led to a ~50% increase in $k_{532}$ for all the BrC types. These results indicate that $NO_3$-induced heterogeneous oxidation darkens some types of atmospheric BrC, which can counterbalance bleaching effects induced by OH oxidation.

In Chapter 4, we compared the imaginary part of the refractive indices (*k*) of brown carbon (BrC) retrieved using online and offline methods. We generated BrC with variable light-absorption properties from the controlled combustion of three structurally different fuels: toluene (aromatic), isooctane (branched alkane), and cyclohexane (cyclic alkane). The online retrieval method involved combining real-time measurements of aerosol absorption coefficients (at 422 nm, 532 nm, and 782 nm) and size distributions with Mie calculations. The offline method involved extracting BrC samples with two organic solvents, methanol and dichloromethane, followed by light-absorption measurements of the extracts using UV-vis spectroscopy. For the least absorbing BrC, *k* values of the extracts in both solvents, retrieved using the offline method, were similar to those of the aerosol, retrieved using the online method. However, for darker BrC, *k* values of the BrC extracts in dichloromethane were smaller than those of the BrC aerosol, and *k* values of the BrC extracts in methanol were the smallest, with the discrepancy among the three increasing with increasing BrC darkness. These results indicate that BrC produced in this study was more soluble in dichloromethane than methanol, and the BrC solubility in both solvents decreased with increasing BrC darkness. Finally, *k* of BrC produced from all fuels, for both BrC aerosol and extracts, followed the same trend of decreasing wavelength dependence (flatter absorption spectra) with increasing *k* as previous data, further supporting the brown-black continuum of light-absorption properties.

The comprehensive picture produced by this research of 1) the dependence of BrC properties on combustion conditions, 2) the evolution of BrC due to oxidation with $NO_3$, and 3) bias associated with the solvent extraction method will improve the understanding of BrC and the ability to represent its light-absorption effects in climate calculations.

## References


Adachi, K., and P. R. Buseck. 2011. Atmospheric Tar Balls from Biomass Burning in Mexico. *J. Geophys. Res.* 116 (5): 2–8. doi.org/10.1029/2010JD015102.

Adler, G., N. L. Wagner, K. D. Lamb, K. M. Manfred, J. P. Schwarz, A. Franchin, A. M. Middlebrook, et al. 2019. Evidence in Biomass Burning Smoke for a Light- Absorbing Aerosol with Properties Intermediate between Brown and Black Carbon. *Aerosol Science and Technology* 53 (9): 976–89. doi.org/10.1080/02786826.2019.1617832.

Akagi, S. K., R. J. Yokelson, C. Wiedinmyer, M. J. Alvarado, J. S. Reid, T. Karl, J. D. Crounse, and P. O. Wennberg. 2011. Emission Factors for Open and Domestic Biomass Burning for Use in Atmospheric Models. *Atmos. Chem. Phys.* 11 (9): 4039–72. doi.org/10.5194/acp-11-4039-2011.

Alexander, D. T. L., P. A. Crozier, and J. R. Anderson. 2008. Brown Carbon Spheres in East Asian Outflow and Their Optical Properties. *Science* 321 (5890): 833–36. doi.org/10.1126/science.1155296.

Alfè, M., B. Apicella, A. Tregrossi, and A. Ciajolo. 2008. Identification of Large Polycyclic Aromatic Hydrocarbons in Carbon Particulates Formed in a Fuel-Rich Premixed Ethylene Flame. *Carbon* 46 (15): 2059–66. doi.org/10.1016/j.carbon.2008.08.019.

Andreae, M. O., and P. Crutzen. 1997. Atmospheric Aerosol: Biogeochemical Sources and Role in Atmospheric Chemistry. *Science* 276 (2): 1052–11058.

Andreae, M. O., and A. Gelencsér. 2006. Black Carbon or Brown Carbon? The Nature of Light-Absorbing Carbonaceous Aerosols. *Atmos. Chem. Phys.* 6 (10): 3131–48. doi.org/10.5194/acp-6-3131-2006.

Apicella, B., A. Carpentieri, M. Alfè, R. Barbella, A. Tregrossi, P. Pucci, and A. Ciajolo. 2007. Mass Spectrometric Analysis of Large PAH in a Fuel-Rich Ethylene Flame. *Proceedings of the Combustion Institute* 31: 547–53. doi.org/10.1016/j.proci.2006.08.014.

Arola, A., G. Schuster, G. Myhre, S. Kazadzis, S. Dey, and S. N. Tripathi. 2011. Inferring Absorbing Organic Carbon Content from AERONET Data. *Atmos. Chem. Phys.* 11: 215–25. doi.org/10.5194/acp-11-215-2011.

Bahadur, R., P. S. Praveen, Y. Xu, and V. Ramanathan. 2012. Solar Absorption by Elemental and Brown Carbon Determined from Spectral Observations. *PNAS* 109 (43): 17366–71. doi.org/10.1073/pnas.1205910109.

Bauer, J. J., X. Y. Yu, R. Cary, N. Laulainen, and C. Berkowitz. 2009. Characterization of the Sunset Semi-Continuous Carbon Aerosol Analyzer. *J. Air & Waste Manage. Assoc.* 59 (7): 826–33. doi.org/10.3155/1047-3289.59.7.826.

Bernardoni, V., R. E. Pileci, L. Caponi, and D. Massabò. 2017. The Multi-Wavelength Absorption Analyzer (MWAA) Model as a Tool for Source and Component Apportionment Based on Aerosol Absorption Properties: Application to Samples Collected in Different Environments.

*Atmosphere* 8 (11): 1–18. doi.org/10.3390/atmos8110218.

Bond, T. C., S. J. Doherty, D. W. Fahey, P. M. Forster, T. Berntsen, B. J. Deangelo, M. G. Flanner, et al. 2013. Bounding the Role of Black Carbon in the Climate System: A Scientific Assessment. *Geophysical Research Atmospheres* 118 (11): 5380–5552. doi.org/10.1002/jgrd.50171.

Bond, T. C., and R. W. Bergstrom. 2006. Light Absorption by Carbonaceous Particles: An Investigative Review. *Aerosol Science and Technology* 40 (1): 27–67. doi.org/10.1080/02786820500421521.

Bond, T. C., G. Habib, and R. W. Bergstrom. 2006. Limitations in the Enhancement of Visible Light Absorption Due to Mixing State. *J. Geophys. Res.* 111 (20): D20211. doi.org/10.1029/2006JD007315.

Bones, D. L., D. K. Henricksen, S. A. Mang, M. Gonsior, A. P. Bateman, T. B. Nguyen, W. J. Cooper, and S. A. Nizkorodov. 2010. Appearance of Strong Absorbers and Fluorophores in Limonene-O3 Secondary Organic Aerosol Due to NH4+ -Mediated Chemical Aging over Long Time Scales. *J. Geophys. Res.* 115 (5): D05203. doi.org/10.1029/2009JD012864.

Brown, H., X. Liu, Y. Feng, Y. Jiang, M. Wu, Z. Lu, and C. Wu. 2018. Radiative Effect and Climate Impacts of Brown Carbon with the Community Atmosphere Model (CAM5). *Atmos. Chem. Phys.* 18: 17745–68.

Browne, E. C., X. Zhang, J. P. Franklin, K. J. Ridley, T. W. Kirchstetter, K. R. Wilson, C. D. Cappa, et al. 2019. Effect of Heterogeneous Oxidative Aging on Light Absorption by

Biomass Burning Organic Aerosol. *Aerosol Science and Technology* 53 (6): 663–74. doi.org/10.1080/02786826.2019.1599321.

Chakrabarty, R. K., H. Moosmüller, L. W. A. Chen, K. Lewis, W. P. Arnott, C. Mazzoleni, M. K. Dubey, et al. 2010. Brown Carbon in Tar Balls from Smoldering Biomass Combustion. *Atmos. Chem. Phys.* 10 (13): 6363–70. doi.org/10.5194/acp-10-6363-2010.

Chen, W. N., Y. C. Chen, C. Y. Kuo, C. H. Chou, C. H. Cheng, C. C. Huang, S. Y. Chang, et al. 2014. The Real-Time Method of Assessing the Contribution of Individual Sources on Visibility Degradation in Taichung. *Sci Total Environ.* 497–498 (110): 219–28. doi.org/10.1016/j.scitotenv.2014.07.120.

Chen, Y., and T. C. Bond. 2010. Light Absorption by Organic Carbon from Wood Combustion. *Atmos. Chem. Phys.* 9 (2001): 20471–513. doi.org/10.5194/acpd-9-20471-2009.

Cheng, Z., K. M. Atwi, Z. Yu, A. Avery, C. Fortner, L. Williams, F. Majluf, J. E. Krechmer, and A. T. Lambe. 2020. Evolution of the Light-Absorption Properties of Combustion Brown Carbon Aerosols Following Reaction with Nitrate Radicals. *Aerosol Science and Technology* 0 (0): 1–15. doi.org/10.1080/02786826.2020.1726867.

Cheng, Z., K. Atwi, T. Onyima, and R. Saleh. 2019. Investigating the Dependence of Light-Absorption Properties of Combustion Carbonaceous Aerosols on Combustion Conditions. *Aerosol Science and Technology* 53 (4): 419–34. doi.org/10.1080/02786826.2019.1566593.

China, S., C. Mazzoleni, K. Gorkowski, A. C. Aiken, and M. K. Dubey. 2013. Morphology and Mixing State of Individual Freshly Emitted Wildfire Carbonaceous Particles. *Nature*

*Communications* 4: 1–7. doi.org/10.1038/ncomms3122.

Claeys, M., R. Vermeylen, F. Yasmeen, Y. Gómez-González, X. Chi, W. Maenhaut, T. Mészáros, and I. Salma. 2012. Chemical Characterisation of Humic-like Substances from Urban, Rural and Tropical Biomass Burning Environments Using Liquid Chromatography with UV/Vis Photodiode Array Detection and Electrospray Ionisation Mass Spectrometry. *Environ. Chem.* 9 (3): 273–84. doi.org/10.1071/EN11163.

Corbin, J. C., H. Czech, D. Massabò, F. B. de Mongeot, G. Jakobi, F. Liu, P. Lobo, et al. 2019. Infrared-Absorbing Carbonaceous Tar Can Dominate Light Absorption by Marine-Engine Exhaust. *Npj Climate and Atmospheric Science* 2 (1). doi.org/10.1038/s41612-019-0069-5.

Corbin, J. C., S. M. Pieber, H. Czech, M. Zanatta, G. Jakobi, D. Massabò, J. Orasche, et al. 2018. Brown and Black Carbon Emitted by a Marine Engine Operated on Heavy Fuel Oil and Distillate Fuels: Optical Properties, Size Distributions, and Emission Factors. *J. Geophys. Res. Atmos* 123 (11): 6175–95. doi.org/10.1029/2017JD027818.

Dasari, S., A. Andersson, S. Bikkina, H. Holmstrand, K. Budhavant, S. Satheesh, E. Asmi, et al. 2019. Photochemical Degradation Affects the Light Absorption of Water-Soluble Brown Carbon in the South Asian Outflow. *Sci. Adv.* 5 (1): eaau8066.

Desyaterik, Y., Y. Sun, X. Shen, T. Lee, X. Wang, T. Wang, and J. L. C. Jr. 2013. Speciation of "Brown" Carbon in Cloud Water Impacted by Agricultural Biomass Burning in Eastern China. *J. Geophys. Res. Atmos.* 118: 7389–99. doi.org/10.1002/jgrd.50561.

Devi, J. J., M. H. Bergin, M. Mckenzie, J. J. Schauer, and R. J. Weber. 2016. Contribution of

Particulate Brown Carbon to Light Absorption in the Rural and Urban Southeast US. *Atmospheric Environment* 136: 95–104. doi.org/10.1016/j.atmosenv.2016.04.011.

Dinar, E., A. Abo Riziq, C. Spindler, C. Erlick, G. Kiss, and Y. Rudich. 2007. The Complex Refractive Index of Atmospheric and Model Humic-like Substances (HULIS) Retrieved by a Cavity Ring down Aerosol Spectrometer (CRD-AS). *The Royal Society of Chemistry* 137: 279–95. doi.org/10.1039/b703111d.

Dingle, J. H., S. Zimmerman, A. L. Frie, J. Min, H. Jung, and R. Bahreini. 2019. Complex Refractive Index, Single Scattering Albedo, and Mass Absorption Coefficient of Secondary Organic Aerosols Generated from Oxidation of Biogenic and Anthropogenic Precursors. *Aerosol Science and Technology* 53 (4): 449–63. doi.org/10.1080/02786826.2019.1571680.

Ditto, J. C., E. B. Barnes, P. Khare, M. Takeuchi, T. Joo, A. A. T. Bui, J. Lee-Taylor, et al. 2018. An Omnipresent Diversity and Variability in the Chemical Composition of Atmospheric Functionalized Organic Aerosol. *Communications Chemistry* 1 (1). doi.org/10.1038/s42004-018-0074-3.

Du, Z., K. He, Y. Cheng, F. Duan, Y. Ma, J. Liu, X. Zhang, M. Zheng, and R. Weber. 2014a. A Yearlong Study of Water-Soluble Organic Carbon in Beijing I: Sources and Its Primary vs. Secondary Nature. *Atmospheric Environment* 92: 514–21. doi.org/10.1016/j.atmosenv.2014.04.060.

———. 2014b. A Yearlong Study of Water-Soluble Organic Carbon in Beijing II: Light Absorption Properties. *Atmospheric Environment* 89: 235–41. doi.org/10.1016/j.atmosenv.2014.02.022.

Faccinetto, A., C. Focsa, P. Desgroux, and M. Ziskind. 2015. Progress toward the Quantitative Analysis of PAHs Adsorbed on Soot by Laser Desorption/Laser Ionization/Time-of-Flight Mass Spectrometry. *Environmental Science and Technology* 49 (17): 10510–20. doi.org/10.1021/acs.est.5b02703.

Feng, Y., V. Ramanathan, and V. R. Kotamarthi. 2013. Brown Carbon: A Significant Atmospheric Absorber of Solar Radiation? *Atmos. Chem. Phys.* 13 (17): 8607–21. doi.org/10.5194/acp-13-8607-2013.

Fischer, D. A., and G. D. Smith. 2018. A Portable, Four-Wavelength, Single-Cell Photoacoustic Spectrometer for Ambient Aerosol Absorption. *Aerosol Science and Technology* 52 (4): 393–406. doi.org/10.1080/02786826.2017.1413231.

Flores, J. M., R. A. Washenfelder, G. Adler, H. J. Lee, L. Segev, J. Laskin, A. Laskin, et al. 2014. Complex Refractive Indices in the Near-Ultraviolet Spectral Region of Biogenic Secondary Organic Aerosol Aged with Ammonia. *Physical Chemistry Chemical Physics* 16 (22): 10629–42. doi.org/10.1039/c4cp01009d.

Frenklach, M. 2002. Reaction Mechanism of Soot Formation in Flames. *Phys. Chem. Chem. Phys.* 4: 2028–2037 This. doi.org/10.1039/b110045a.

Frenklach, M., and H. A. I. Wang. 1990. Detailed Modeling of Soot Particle Nucleation and Growth. *The Combustion Institute*, 1559–66.

Fuzzi, S., and S. Decesari. 2016. Light Absorption Properties of Brown Carbon in the High Himalayas. *J. Geophys. Res. Atmos.* 121: 9621–39.

doi.org/10.1002/2016JD025030.Received.

Gelencsér, A., A. Hoffer, G. Kiss, E. Tombácz, R. Kurdi, and L. Bencze. 2003. In-Situ Formation of Light-Absorbing Organic Matter in Cloud Water. *J. Atoms. Chems.* 45 (1): 25–33. doi.org/10.1023/A:1024060428172.

Gilardoni, S., P. Massoli, M. Paglione, L. Giulianelli, C. Carbone, M. Rinaldi, S. Decesari, et al. 2016. Direct Observation of Aqueous Secondary Organic Aerosol from Biomass-Burning Emissions. *PNAS* 113 (36): 10013–18. doi.org/10.1073/pnas.1602212113.

Graber, E. R., and Y. Rudich. 2006. Atmospheric HULIS: How Humic-like Are They? A Comprehensive and Critical Review. *Atmos. Chem. Phys.* 6 (3): 729–53. doi.org/10.5194/acp-6-729-2006.

Haan, D. O. De, L. N. Hawkins, H. G. Welsh, R. Pednekar, J. R. Casar, E. A. Pennington, A. De Loera, et al. 2017. Brown Carbon Production in Ammonium- or Amine-Containing Aerosol Particles by Reactive Uptake of Methylglyoxal and Photolytic Cloud Cycling. *Environ. Sci. Technol.* 51 (13): 7458–66. doi.org/10.1021/acs.est.7b00159.

Haisch, C. 2012. Photoacoustic Spectroscopy for Analytical. *Meas. Sci. Technol.* 23: 012001. doi.org/10.1088/0957-0233/23/1/012001.

Hand, J. L., W. C. Malm, A. Laskin, D. Day, T. Lee, C. Wang, C. Carrico, et al. 2005. Optical, Physical, and Chemical Properties of Tar Balls Observed during the Yosemite Aerosol Characterization Study. *J. Geophys. Res.* 110: 1–14. doi.org/10.1029/2004JD005728.

Haynes, J. P., K. E. Miller, and B. J. Majestic. 2019. Investigation into Photoinduced Auto-

Oxidation of Polycyclic Aromatic Hydrocarbons Resulting in Brown Carbon Production. *Environ. Sci. Technol.* 53 (2): 682–91. doi.org/10.1021/acs.est.8b05704.

He, Q., N. Bluvshtein, L. Segev, D. Meidan, J. M. Flores, S. S. Brown, W. Brune, and Y. Rudich. 2018. Evolution of the Complex Refractive Index of Secondary Organic Aerosols during Atmospheric Aging. *Environ. Sci. Technol.* 52: 3456−3465. doi.org/10.1021/acs.est.7b05742.

Hecobian, A., X. Zhang, M. Zheng, N. Frank, E. S. Edgerton, R. J. Weber, A. Sciences, T. Park, and N. Carolina. 2010. Water-Soluble Organic Aerosol Material and the Light-Absorption Characteristics of Aque- Ous Extracts Measured Over the Southeastern United States. Atmos. *Atmos. Chem. Phys.* 10: 5965–77. doi.org/10.5194/acp-10-5965-2010.

Hoffer, A., A. Gelencsér, P. Guyon, G. Kiss, O. Schmid, G. P. Frank, P. Artaxo, and M. O. Andreae. 2006. Optical Properties of Humic-like Substances (HULIS) in Biomass-Burning Aerosols. *Atmos. Chem. Phys.* 6 (11): 3563–70. doi.org/10.5194/acp-6-3563-2006.

Hoffer, A., G. Kiss, M. Blazsó, and A. Gelencsér. 2004. Chemical Characterization of Humic-like Substances (HULIS) Formed from a Lignin-Type Precursor in Model Cloud Water. *Geophys. Res. Lett.* 31 (6): ,L06115. doi.org/10.1029/2003gl018962.

Hoffer, A., A. Tóth, I. NyirÅ'-Kósa, M. Pósfai, and A. Gelencsér. 2016. Light Absorption Properties of Laboratory-Generated Tar Ball Particles. *Atmos. Chem. Phys.* 16 (1): 239–46. doi.org/10.5194/acp-16-239-2016.

Hong, L., G. Liu, L. Zhou, J. Li, H. Xu, and D. Wu. 2017. Emission of Organic Carbon, Elemental

Carbon and Water-Soluble Ions from Crop Straw Burning under Flaming and Smoldering Conditions. *Particuology* 31: 181–90. doi.org/10.1016/j.partic.2016.09.002.

Hopkins, R. J., A. V. Tivanski, B. D. Marten, and M. K. Gilles. 2007. Chemical Bonding and Structure of Black Carbon Reference Materials and Individual Carbonaceous Atmospheric Aerosols. *J. Aerosol Sci.* 38 (6): 573–91. doi.org/10.1016/j.jaerosci.2007.03.009.

Hunter, J. F., D. A. Day, B. B. Palm, R. L. N. Yatavelli, A. W. H. Chan, L. Kaser, L. Cappellin, et al. 2017. Comprehensive Characterization of Atmospheric Organic Carbon at a Forested Site. *Nature Geoscience* 10 (10): 748–53. doi.org/10.1038/NGEO3018.

IPCC. 2013. Climate Change 2013: The Physical Science Basis. Contribution of Working Group I to the Fifth Assessment Report of the Intergovernmental Panel on Climate Change, Chapter 8: Anthropogenic and Natural Radiative Forcing. Edited by V. Bex and P.M. Midgley (eds.) Stocker, T.F., D. Qin, G.-K. Plattner, M. Tignor, S.K. Allen, J. Boschung, A. Nauels, Y. Xia. *Climate Change 2013: The Physical Science Basis. Contribution of Working Group I to the Fifth Assessment Report of the Intergovernmental Panel on Climate Change*. Cambridge, United Kingdom and New York, NY, USA. doi.org/10.1017/ CBO9781107415324.018.

Jacobson, M. Z. 2001. Strong Radiative Heating Due to the Mixing State of Black Carbon in Atmospheric Aerosols. *Nature* 409 (6821): 695–97. doi.org/10.1038/35055518.

Jacobson, M. Z. 2012. Investigating Cloud Absorption Effects: Global Absorption Properties of Black Carbon, Tar Balls, and Soil Dust in Clouds and Aerosols. *J. Geophys. Res.* 117: 1–25. doi.org/10.1029/2011JD017218.

Jethva, H., and O. Torres. 2011. Satellite-Based Evidence of Wavelength-Dependent Aerosol Absorption in Biomass Burning Smoke Inferred from Ozone Monitoring Instrument. *Atmos. Chem. Phys.* 11: 10541–51. doi.org/10.5194/acp-11-10541-2011.

Johansson, K. O., M. P. Head-Gordon, P. E. Schrader, K. R. Wilson, and H. A. Michelsen. 2018. Resonance-Stabilized Hydrocarbon-Radical Chain Reactions May Explain Soot Inception and Growth. *Science* 361 (September): 997–1000. doi.org/10.1126/science.aat3417.

Kahnt, A., S. Behrouzi, R. Vermeylen, M. Safi Shalamzari, J. Vercauteren, E. Roekens, M. Claeys, and W. Maenhaut. 2013. One-Year Study of Nitro-Organic Compounds and Their Relation to Wood Burning in PM10 Aerosol from a Rural Site in Belgium. *Atmospheric Environment* 81: 561–68. doi.org/10.1016/j.atmosenv.2013.09.041.

Kampf, C. J., A. Filippi, C. Zuth, T. Hoffmann, and T. Opatz. 2016. Secondary Brown Carbon Formation via the Dicarbonyl Imine Pathway: Nitrogen Heterocycle Formation and Synergistic Effect. *Physical Chemistry Chemical Physics* 18 (27): 18353–64. doi.org/10.1039/c6cp03029g.

Karagulian, F., and M. J. Rossi. 2007. Heterogeneous Chemistry of the NO3 Free Radical and N2O5 on Decane Flame Soot at Ambient Temperature: Reaction Products and Kinetics. *J. Phys. Chem. A* 111 (3): 1914–26. doi.org/10.1021/jp0670891.

Karanasiou, A., M. C. Minguillón, M. Viana, A. Alastuey, J.-P. Putaud, W. Maenhaut, P. Panteliadis, et al. 2015. Thermal-Optical Analysis for the Measurement of Elemental Carbon (EC) and Organic Carbon (OC) in Ambient Air a Literature Review. *Atmos. Meas. Tech.* 8 (9): 9649–9712. doi.org/10.5194/amtd-8-9649-2015.

Karavalakis, G., V. Boutsika, S. Stournas, and E. Bakeas. 2011. Biodiesel Emissions Profile in Modern Diesel Vehicles. Part 2: Effect of Biodiesel Origin on Carbonyl, PAH, Nitro-PAH and Oxy-PAH Emissions. *Science of the Total Environment, The* 409 (4): 738–47. doi.org/10.1016/j.scitotenv.2010.11.010.

Keyte, I. J., R. M. Harrisonz, and G. Lammel. 2013. Chemical Reactivity and Long-Range Transport Potential of Polycyclic Aromatic Hydrocarbons – a Review. *Chem. Soc. Rev.* 42: 9333--9391. doi.org/10.1039/c3cs60147a.

Kirchstetter, T. W., T. Novakov, and P. V. Hobbs. 2004. Evidence That the Spectral Dependence of Light Absorption by Aerosols Is Affected by Organic Carbon. *J. Geophys. Res.* 109 (21): D21208. doi.org/10.1029/2004JD004999.

Knopf, D. A., S. M. Forrester, and J. H. Slade. 2011. Heterogeneous Oxidation Kinetics of Organic Biomass Burning Aerosol. *Phys. Chem. Chem. Phys* 13: 21050–62. doi.org/10.1039/c1cp22478f.

Kwamena, N. A., and J. P. D. Abbatt. 2008. Heterogeneous Nitration Reactions of Polycyclic Aromatic Hydrocarbons and N-Hexane Soot by Exposure to NO3/NO2/N2O5. *Atmospheric Environment* 42 (35): 8309–14. doi.org/10.1016/j.atmosenv.2008.07.037.

Lack, D. A., and J. M. Langridge. 2013. On the Attribution of Black and Brown Carbon Light Absorption Using the Ångström Exponent. *Atmos. Chem. Phys.* 13 (20): 10535–43. doi.org/10.5194/acp-13-10535-2013.

Lack, D. A., J. M. Langridge, R. Bahreini, C. D. Cappa, A. M. Middlebrook, and J. P. Schwarz.

2012. Brown Carbon and Internal Mixing in Biomass Burning Particles. *PNAS* 109 (37): 14802–7. doi.org/10.1073/pnas.1206575109.

Lack, D. A., E. R. Lovejoy, T. Baynard, A. Pettersson, and A. R. Ravishankara. 2006. Aerosol Absorption Measurement Using Photoacoustic Spectroscopy: Sensitivity, Calibration, and Uncertainty Developments. *Aerosol Science and Technology* 40 (9): 697–708. doi.org/10.1080/02786820600803917.

Lack, D. A., M. S. Richardson, D. Law, J. M. Langridge, C. D. Cappa, R. J. McLaughlin, and D. M. Murphy. 2012. Aircraft Instrument for Comprehensive Characterization of Aerosol Optical Properties, Part 2: Black and Brown Carbon Absorption and Absorption Enhancement Measured with Photo Acoustic Spectroscopy. *Aerosol Science and Technology* 46 (5): 555–68. doi.org/10.1080/02786826.2011.645955.

Lambe, A. T., C. D. Cappa, P. Massoli, T. B. Onasch, S. D. Forestieri, A. T. Martin, M. J. Cummings, et al. 2013. Relationship between Oxidation Level and Optical Properties of Secondary Organic Aerosol. *Environ. Sci. Technol.* 47 (12): 6349–57. doi.org/10.1021/es401043j.

Laskin, A., J. Laskin, and S. A. Nizkorodov. 2015. Chemistry of Atmospheric Brown Carbon. *Chemical Reviews* 115 (10): 4335–82. doi.org/10.1021/cr5006167.

Lee, H. J., P. K. Aiona, A. Laskin, J. Laskin, and S. A. Nizkorodov. 2014. Effect of Solar Radiation on the Optical Properties and Molecular Composition of Laboratory Proxies of Atmospheric Brown Carbon. *Environ. Sci. Technol.* 48: 10217−10226. doi.org/10.1021/es502515r.

Li, C., Q. He, A. P. S. Hettiyadura, U. Käfer, G. Shmul, D. Meidan, R. Zimmermann, et al. 2019. Formation of Secondary Brown Carbon in Biomass Burning Aerosol Proxies through NO3 Radical Reactions. *Environ. Sci. Technol.* 54 (3): 1395−1405. doi.org/10.1021/acs.est.9b05641.

Li, C., Q. He, J. Schade, J. Passig, R. Zimmermann, D. Meidan, A. Laskin, and Y. Rudich. 2019. Dynamic Changes in Optical and Chemical Properties of Tar Ball Aerosols by Atmospheric Photochemical Aging. *Atmos. Chem. Phys.* 19: 139–63.

Li, X., Y. Chen, and T. C. Bond. 2016. Light Absorption of Organic Aerosol from Pyrolysis of Corn Stalk. *Atmospheric Environment* 144: 249–56. doi.org/10.1016/j.atmosenv.2016.09.006.

Lin, G., J. E. Penner, M. G. Flanner, S. Sillman, L. Xu, and C. Zhou. 2014. Radiative Forcing of Organic Aerosol in the Atmosphere and on Snow: Effects of SOA and Brown Carbon. *J. Geophys. Res. Atmos.* 119: 7453–7476. doi.org/10.1002/2013JD021186.Received.

Lin, H., and A. J. Campillo. 1985. Photothermal Aerosol Absorption Spectroscopy. *APPLIED OPTICS* 24 (3): 422–36.

Lin, P., G. Engling, and J. Z. Yu. 2010. Humic-like Substances in Fresh Emissions of Rice Straw Burning and in Ambient Aerosols in the Pearl River Delta Region, China. *Atmospheric Chemistry and Physics* 10 (14): 6487–6500. doi.org/10.5194/acp-10-6487-2010.

Lin, P., P. K. Aiona, Y. Li, M. Shiraiwa, J. Laskin, S. A. Nizkorodov, and A. Laskin. 2016. Molecular Characterization of Brown Carbon in Biomass Burning Aerosol Particles. *Environ.*

*Sci. Technol.* 50 (21): 11815–24. doi.org/10.1021/acs.est.6b03024.

Lin, P., N. Bluvshtein, Y. Rudich, S. A. Nizkorodov, J. Laskin, and A. Laskin. 2017. Molecular Chemistry of Atmospheric Brown Carbon Inferred from a Nationwide Biomass Burning Event. *Environ. Sci. Technol. 2017,* 51: 11561–70. doi.org/10.1021/acs.est.7b02276.

Lin, P., J. Laskin, S. A. Nizkorodov, and A. Laskin. 2015. Revealing Brown Carbon Chromophores Produced in Reactions of Methylglyoxal with Ammonium Sulfate. *Environ. Sci. Technol.* 49 (24): 14257–66. doi.org/10.1021/acs.est.5b03608.

Lin, P., J. Liu, J. E. Shilling, S. M. Kathmann, J. Laskinc, and A. Laskin. 2015. Molecular Characterization of Brown Carbon (BrC) Chromophores in Secondary Organic Aerosol Generated from Photo-Oxidation of Toluene. *Phys.Chem.Chem.Phys.* 17 (36): 23283–23676. doi.org/10.1039/c5cp02563j.

Lin, P., J. Z. Yu, G. Engling, and M. Kalberer. 2012. Organosulfates in Humic-like Substance Fraction Isolated from Aerosols at Seven Locations in East Asia: A Study by Ultra-High-Resolution Mass Spectrometry. *Environ. Sci. Technol.* 46 (24): 13118–27. doi.org/10.1021/es303570v.

Linke, C., I. Ibrahim, N. Schleicher, R. Hitzenberger, M. O. Andreae, T. Leisner, and M. Schnaiter. 2016. A Novel Single-Cavity Three-Wavelength Photoacoustic Spectrometer for Atmospheric Aerosol Research. *Atmos. Meas. Tech.* 9: 5331–46. doi.org/10.5194/amt-9-5331-2016.

Liu, C., P. Zhang, B. Yang, Y. Wang, and J. Shu. 2012. Kinetic Studies of Heterogeneous

Reactions of Polycyclic Aromatic Hydrocarbon Aerosols with NO3 Radicals. *Environ. Sci. Technol.* 46 (3): 7575−7580. doi.org/10.1021/es301403d.

Liu, D., T. Lin, J. Hussain, C. Zhineng, Y. Xu, K. Li, and Z. Gan. 2017. Concentration, Source Identification, and Exposure Risk Assessment of PM2.5-Bound Parent PAHs and Nitro-PAHs in Atmosphere from Typical Chinese Cities. *Scientific Reports* 7: 10398. doi.org/10.1038/s41598-017-10623-4.

Liu, J., M. Bergin, H. Guo, L. King, N. Kotra, E. Edgerton, and R. J. Weber. 2013. Size-Resolved Measurements of Brown Carbon in Water and Methanol Extracts and Estimates of Their Contribution to Ambient Fine-Particle Light Absorption. *Atmos. Chem. Phys.* 13: 12389–404. doi.org/10.5194/acp-13-12389-2013.

Liu, S., A. C. Aiken, K. Gorkowski, M. K. Dubey, C. D. Cappa, L. R. Williams, S. C. Herndon, et al. 2015. Enhanced Light Absorption by Mixed Source Black and Brown Carbon Particles in UK Winter. *Nature Communications* 6: 8435. doi.org/10.1038/ncomms9435.

Lu, J. W., J. M. Flores, A. Lavi, A. Abo-riziq, and Y. Rudich. 2011. Changes in the Optical Properties of Benzo[a]Pyrene-Coated Aerosols upon Heterogeneous Reactions with NO2 and NO3. *Phys. Chem. Chem. Phys* 13: 6484–92. doi.org/10.1039/c0cp02114h.

Mak, J., S. Gross, and A. K. Bertram. 2007. Uptake of NO3 on Soot and Pyrene Surfaces. *Geophys. Res. Lett.* 34: L10804. doi.org/10.1029/2007GL029756.

Marrero-Ortiz, W., M. Hu, Z. Du, Y. Ji, Y. Wang, S. Guo, Y. Lin, et al. 2019. Formation and Optical Properties of Brown Carbon from Small α-Dicarbonyls and Amines. *Environ. Sci.*

*Technol.* 53 (1): 117–26. doi.org/10.1021/acs.est.8b03995.

Martinsson, J., A. C. Eriksson, I. E. Nielsen, V. B. Malmborg, E. Ahlberg, C. Andersen, R. Lindgren, et al. 2015. Impacts of Combustion Conditions and Photochemical Processing on the Light Absorption of Biomass Combustion Aerosol. *Environ. Sci. Technol.* 49 (24): 14663–71. doi.org/10.1021/acs.est.5b03205.

Michelsen, H. A. 2017. Probing Soot Formation, Chemical and Physical Evolution, and Oxidation: A Review of in Situ Diagnostic Techniques and Needs. *Proceedings of the Combustion Institute* 36 (1): 717–35. doi.org/10.1016/j.proci.2016.08.027.

Moosmüller, H., W. P. Arnott, C. F. Rogers, H. Moosmüller, W. P. Arnott, and C. F. Rogers. 1997. Methods for Real-Time, In Situ Measurement of Aerosol Light Absorption. *Journal of the Air & Waste Management Association* 47 (2): 157–66. doi.org/10.1080/10473289.1997.10464430.

Moosmüller, H., R. K. Chakrabarty, and W. P. Arnott. 2009. Aerosol Light Absorption and Its Measurement: A Review. *Journal of Quantitative Spectroscopy and Radiative Transfer* 110 (11): 844–78. doi.org/10.1016/j.jqsrt.2009.02.035.

Mukai, H., and Y. Ambe. 1986. Characterization of a Humic Acid-like Brown Substance in Airborne Particulate Matter and Tentative Identification of Its Origin. *Atmospheric Environment* 20 (5): 813–19.

Nakayama, T., K. Sato, Y. Matsumi, T. Imamura, A. Yamazaki, and A. Uchiyama. 2013. Wavelength and NOx Dependent Complex Refractive Index of SOAs Generated from the

Photooxidation of Toluene. *Atmos. Chem. Phys.* 13: 531–45. doi.org/10.5194/acp-13-531-2013.

Nakayama, T., Y. Matsumi, K. Sato, T. Imamura, and A. Yamazaki. 2010. Laboratory Studies on Optical Properties of Secondary Organic Aerosols Generated during the Photooxidation of Toluene and the Ozonolysis of A-pinene. *J. Geophys. Res.* 115: D24204. doi.org/10.1029/2010JD014387.

O'Brien, R. E., A. Laskin, J. Laskin, S. Liu, R. Weber, L. M. Russell, and A. H. Goldstein. 2013. Molecular Characterization of Organic Aerosol Using Nanospray Desorption/Electrospray Ionization Mass Spectrometry: CalNex 2010 Field Study. *Atmospheric Environment* 68: 265–72. doi.org/10.1016/j.atmosenv.2012.11.056.

Olson, M. R., M. V. Garcia, M. A. Robinson, P. Van Rooy, M. A. Dietenberger, M. Bergin, and J. J. Schauer. 2015. Investigation of Black and Brown Carbon Multiple-Wavelength-Dependent Light Absorption from Biomass and Fossil Fuel Combustion Source Emissions. *J. Geophys. Res. Atmos* 120: 6682–97. doi.org/10.1002/2014JD022970.Received.

Phillips, S. M., and G. D. Smith. 2014. Light Absorption by Charge Transfer Complexes in Brown Carbon Aerosols. *Environ. Sci. Technol. Lett.* 1 (10): 382–86. doi.org/10.1021/ez500263j.

———. 2015. Further Evidence for Charge Transfer Complexes in Brown Carbon Aerosols from Excitation-Emission Matrix Fluorescence Spectroscopy. *J. Phys. Chem.* 119 (19): 4545–51. doi.org/10.1021/jp510709e.

Phillips, S. M., and G. D. Smith. 2017. Spectroscopic Comparison of Water- and Methanol-Soluble

Brown Carbon Particulate Matter. *Aerosol Science and Technology* 51 (9): 1113–1121. doi.org/10.1080/02786826.2017.1334109.

Pokhrel, R. P., N. L. Wagner, J. M. Langridge, D. A. Lack, T. Jayarathne, E. A. Stone, C. E. Stockwell, R. J. Yokelson, and S. M. Murphy. 2016. Parameterization of Single-Scattering Albedo (SSA) and Absorption Ångström Exponent (AAE) with EC/OC for Aerosol Emissions from Biomass Burning. *Atmos. Chem. Phys.* 16 (15): 9549–61. doi.org/10.5194/acp-16-9549-2016.

Pöschl, U. 2005. Atmospheric Aerosols: Composition, Transformation, Climate and Health Effects Ulrich. *Angew. Chem. Int. Ed.* 44: 7520–40. doi.org/10.1002/anie.200501122.

Posfai, M., A. Gelencser, R. Simonics, K. Arato, J. Li, P. V. Hobbs, and P. R. Buseck. 2004. Atmospheric Tar Balls: Particles from Biomass and Biofuel Burning. *J. Geophys. Res.* 109: D06213. doi.org/10.1029/2003JD004169.

Ramanathan, V., F. Li, M. V Ramana, P. S. Praveen, D. Kim, C. E. Corrigan, H. Nguyen, et al. 2007. Atmospheric Brown Clouds: Hemispherical and Regional Variations in Long-Range Transport, Absorption, and Radiative Forcing. *J. Geophys. Res.* 112: D22S21. doi.org/10.1029/2006JD008124.

Rizzo, L. V., P. Artaxo, T. Müller, A. Wiedensohler, M. Paixão, G. G. Cirino, A. Arana, et al. 2013. Long Term Measurements of Aerosol Optical Properties at a Primary Forest Site in Amazonia. *Atmos. Chem. Phys.* 13 (5): 2391–2413. doi.org/10.5194/acp-13-2391-2013.

Rizzo, L. V., A. L. Correia, P. Artaxo, A. S. Procápio, and M. O. Andreae. 2011. Spectral

Dependence of Aerosol Light Absorption over the Amazon Basin. *Atmos. Chem. Phys.* 11 (17): 8899–8912. doi.org/10.5194/acp-11-8899-2011.

Roden, C. A., T. C. Bond, S. Conway, and A. B. Osorto Pinel. 2006. Emission Factors and Real-Time Optical Properties of Particles Emitted from Traditional Wood Burning Cookstoves. *Environ. Sci. Technol.* 40 (21): 6750–57. doi.org/10.1021/es052080i.

Russo, C., M. Alfe, J. N. Rouzaud, F. Stanzione, A. Tregrossi, and A. Ciajolo. 2013. Probing Structures of Soot Formed in Premixed Flames of Methane, Ethylene and Benzene. *Proceedings of the Combustion Institute* 34 (1): 1885–92. doi.org/10.1016/j.proci.2012.06.127.

Saleh, R., C. J. Hennigan, G. R. McMeeking, W. K. Chuang, E. S. Robinson, H. Coe, N. M. Donahue, and A. L. Robinson. 2013. Absorptivity of Brown Carbon in Fresh and Photo-Chemically Aged Biomass-Burning Emissions. *Atmos. Chem. Phys.* 13: 7683–93. doi.org/10.5194/acp-13-7683-2013.

Saleh, R. 2020. From Measurements to Models: Toward Accurate Representation of Brown Carbon in Climate Calculations. *Curr Pollution Rep*, no. 706. doi.org/doi.org/10.1007/s40726-020-00139-3.

Saleh, R., Z. Cheng, and K. Atwi. 2018. The Brown–Black Continuum of Light-Absorbing Combustion Aerosols. Rapid-communication. *Environ. Sci. Technol. Lett.* 5: 508–13. doi.org/10.1021/acs.estlett.8b00305.

Saleh, R., M. Marks, J. Heo, P. J. Adams, N. M. Donahue, and A. L. Robinson. 2015. Contribution

of Brown Carbon and Lensing to the Direct Radiative Effect of Carbonaceous Aerosols from Biomass and Biofuel Burning Emissions. *J. Geophys. Res. Atmos* 120 (10): 10,285–10,296. doi.org/10.1002/ 2015JD023697.

Saleh, R., E. S. Robinson, D. S. Tkacik, A. T. Ahern, S. Liu, A. C. Aiken, R. C. Sullivan, et al. 2014. Brownness of Organics in Aerosols from Biomass Burning Linked to Their Black Carbon Content. *Nature Geoscience* 7 (9): 647–50. doi.org/10.1038/ngeo2220.

Satish, R., P. Shamjad, N. Thamban, S. Tripathi, and N. Rastogi. 2017. Temporal Characteristics of Brown Carbon over the Central Indo- Gangetic Plain. *Environ. Sci. Technol.* 51: 6765−6772. doi.org/10.1021/acs.est.7b00734.

Sedlacek, A., J. Lee, A. Sedlacek, J. Lee, and L. Law. 2008. Photothermal Interferometric Aerosol Absorption Spectrometry. *Aerosol Science and Technology* 41 (12): 1089–1101. doi.org/10.1080/02786820701697812.

Sengupta, D., V. Samburova, C. Bhattarai, E. Kirillova, L. Mazzoleni, M. Iaukea-Lum, A. Watts, H. Moosmüller, and A. Khlystov. 2018. Light Absorption by Polar and Non-Polar Aerosol Compounds from Laboratory Biomass Combustion. *Atmospheric Chemistry and Physics* 18 (15): 10849–67. doi.org/10.5194/acp-18-10849-2018.

Shamjad, P. M., R. V Satish, N. M. Thamban, N. Rastogi, and S. N. Tripathi. 2018. Absorbing Refractive Index and Direct Radiative Forcing of Atmospheric Brown Carbon over Gangetic Plain. *ACS Earth Space Chem.* 2: 31–37. doi.org/10.1021/acsearthspacechem.7b00074.

Shamjad, P. M., S. N. Tripathi, N. M. Thamban, and H. Vreeland. 2016. Refractive Index and

Absorption Attribution of Highly Absorbing Brown Carbon Aerosols from an Urban Indian City-Kanpur. *Scientific Reports* 6 (October): 1–7. doi.org/10.1038/srep37735.

Shen, G., S. Tao, S. Wei, Y. Zhang, R. Wang, B. Wang, W. Li, H. Shen, Y. Huang, Y. Chen, H. Chen, Y. Yang, W. Wang, X. Wang, et al. 2012. Emissions of Parent, Nitro, and Oxygenated Polycyclic Aromatic Hydrocarbons from Residential Wood Combustion in Rural China. *Environ. Sci. Technol.* 46: 8123−8130. doi.org/10.1021/es301146v.

Shen, G., S. Tao, S. Wei, Y. Zhang, R. Wang, B. Wang, W. Li, H. Shen, Y. Huang, Y. Chen, H. Chen, Y. Yang, W. Wang, W. Wei, et al. 2012. Reductions in Emissions of Carbonaceous Particulate Matter and Polycyclic Aromatic Hydrocarbons from Combustion of Biomass Pellets in Comparison with Raw Fuel Burning. *Environ. Sci. Technol.* 46 (11): 6409–16. doi.org/10.1021/es300369d.

Shetty, N. J., A. Pandey, S. Baker, W. M. Hao, and R. K. Chakrabarty. 2019. Measuring Light Absorption by Freshly Emitted Organic Aerosols: Optical Artifacts in Traditional Solvent-Extraction-Based Methods. *Atmos. Chem. Phys.* 19: 8817–30.

Stevens, R., and A. Dastoor. 2019. A Review of the Representation of Aerosol Mixing State in Atmospheric Models. *Atmosphere* 10 (4). doi.org/10.3390/atmos10040168.

Stockwell, C. E., T. Jayarathne, M. A. Cochrane, K. C. Ryan, E. I. Putra, B. H. Saharjo, A. D. Nurhayati, et al. 2016. Field Measurements of Trace Gases and Aerosols Emitted by Peat Fires in Central Kalimantan, Indonesia, during the 2015 El Niño. *Atmos. Chem. Phys.* 16 (18): 11711–32. doi.org/10.5194/acp-16-11711-2016.

Sumlin, B. J., A. Pandey, M. J. Walker, R. S. Pattison, B. J. Williams, and R. K. Chakrabarty. 2017. Atmospheric Photooxidation Diminishes Light Absorption by Primary Brown Carbon Aerosol from Biomass Burning. *Environ. Sci. Technol. Lett* 4: 540−545. doi.org/10.1021/acs.estlett.7b00393.

Sun, Y. L., Q. Zhang, C. Anastasio, and J. Sun. 2010. Insights into Secondary Organic Aerosol Formed via Aqueous-Phase Reactions of Phenolic Compounds Based on High Resolution Mass Spectrometry. *Atmos. Chem. Phys.* 10 (10): 4809–22. doi.org/10.5194/acp-10-4809-2010.

Terhune, R. W., and J. E. Anderson. 1977. Spectrophone Measurements of the Absorption of Visible Light by Aerosols in the Atmosphere. *Optics Letters* 1 (2): 70–72.

Tivanski, A. V., R. J. Hopkins, T. Tyliszczak, and M. K. Gilles. 2007. Oxygenated Interface on Biomass Burn Tar Balls Determined by Single Particle Scanning Transmission X-Ray Microscopy. *J. Phys. Chem. A* 111 (25): 5448–58. doi.org/10.1021/jp070155u.

Tóth, A., A. Hoffer, I. Nyiro-Kósa, M. Pósfai, and A. Gelencsér. 2014. Atmospheric Tar Balls: Aged Primary Droplets from Biomass Burning? *Atmos. Chem. Phys.* 14 (13): 6669–75. doi.org/10.5194/acp-14-6669-2014.

Turns, S. R. 2000. *An Introduction to Combustion: Concepts and Applications*. Second edi. New York: The McGraw-Hill Companies, Inc.

Updyke, K. M., T. B. Nguyen, and S. A. Nizkorodov. 2012. Formation of Brown Carbon via Reactions of Ammonia with Secondary Organic Aerosols from Biogenic and Anthropogenic

Precursors. *Atmospheric Environment* 63: 22–31. doi.org/10.1016/j.atmosenv.2012.09.012.

Utry, N., T. Ajtai, ágnes Filep, M. Dániel Pintér, A. Hoffer, Z. Bozoki, and G. Szabó. 2013. Mass Specific Optical Absorption Coefficient of HULIS Aerosol Measured by a Four-Wavelength Photoacoustic Spectrometer at NIR, VIS and UV Wavelengths. *Atmospheric Environment* 69: 321–24. doi.org/10.1016/j.atmosenv.2013.01.003.

Vicente, E. D., M. A. Duarte, A. I. Calvo, T. F. Nunes, L. A. C. Tarelho, D. Custódio, C. Colombi, et al. 2015. Influence of Operating Conditions on Chemical Composition of Particulate Matter Emissions from Residential Combustion. *Atmospheric Research* 166: 92–100. doi.org/10.1016/j.atmosres.2015.06.016.

Wang, L., Z. Li, Q. Tian, Y. Ma, F. Zhang, Y. Zhang, D. Li, K. Li, and L. Li. 2013. Estimate of Aerosol Absorbing Components of Black Carbon, Brown Carbon, and Dust from Ground-Based Remote Sensing Data of Sun-Sky Radiometers. *J. Geophys. Res.* 118 (12): 6534–43. doi.org/10.1002/jgrd.50356.

Wang, X, C. L. Heald, D. A. Ridley, J. P. Schwarz, J. R. Spackman, A. E. Perring, H. Coe, and D. Liu. 2014. Exploiting Simultaneous Observational Constraints on Mass and Absorption to Estimate the Global Direct Radiative Forcing of Black Carbon and Brown Carbon. *Atmos. Chem. Phys.* 14: 10989–10. doi.org/10.5194/acp-14-10989-2014.

Wang, X., C. L. Heald, A. J. Sedlacek, S. S. De Sá, S. T. Martin, M. L. Alexander, T. B. Watson, et al. 2016. Deriving Brown Carbon from Multiwavelength Absorption Measurements: Method and Application to AERONET and Aethalometer Observations. *Atmos. Chem. Phys.* 16: 12733–52. doi.org/10.5194/acp-16-12733-2016.

Wang, Y., M. Hu, P. Lin, T. Tan, M. Li, N. Xu, J. Zheng, et al. 2019. Enhancement in Particulate Organic Nitrogen and Light Absorption of Humic-Like Substances over Tibetan Plateau Due to Long-Range Transported Biomass Burning Emissions. Research-article. *Environ. Sci. Technol.* 53: 14222–32. doi.org/10.1021/acs.est.9b06152.

Washenfelder, R. A., A. R. Attwood, C. A. Brock, H. Guo, L. Xu, R. J. Weber, N. L. Ng, et al. 2015. Biomass Burning Dominates Brown Carbon Absorption in the Rural Southeastern United States. *Geophys. Res. Lett.* 42: 653–664. doi.org/10.1002/2014GL062444.Received.

Watson, J. G., J. C. Chow, and L. A. Chen. 2005. *Summary of Organic and Elemental Carbon / Black Carbon Analysis Methods and Intercomparisons*. *Aerosol and Air Quality Research*. Vol. 5. doi.org/10.4209/aaqr.2005.06.0006.

Wiegand, J. R., L. D. Mathews, and G. D. Smith. 2014. A UV-Vis Photoacoustic Spectrophotometer. *Anal. Chem.* 86 (12): 6049–56. doi.org/10.1021/ac501196u.

Wong, J. P. S., A. Nenes, and R. J. Weber. 2017. Changes in Light Absorptivity of Molecular Weight Separated Brown Carbon Due to Photolytic Aging. *Environ. Sci. Technol.* 51: 8414−8421. doi.org/10.1021/acs.est.7b01739.

Wu, G. M., Z. Y. Cong, S. C. Kang, K. Kawamura, P. Q. Fu, Y. L. Zhang, X. Wan, S. P. Gao, and B. Liu. 2016. Brown Carbon in the Cryosphere: Current Knowledge and Perspective. *Advances in Climate Change Research* 7 (1–2): 82–89. doi.org/10.1016/j.accre.2016.06.002.

Xie, M., X. Chen, M. D. Hays, M. Lewandowski, O. John, T. E. Kleindienst, and A. L. Holder. 2017. Light Absorption of Secondary Organic Aerosol: Composition and Contribution of

Nitroaromatic Compounds. *Environ. Sci. Technol.* 51: 11607−11616. doi.org/10.1021/acs.est.7b03263.

Xie, M., M. D. Hays, and A. L. Holder. 2017. Light-Absorbing Organic Carbon from Prescribed and Laboratory Biomass Burning and Gasoline Vehicle Emissions. *Scientific Reports* 7 (1): 1–9. doi.org/10.1038/s41598-017-06981-8.

Xie, M., G. Shen, A. L. Holder, M. D. Hays, and J. J. Jetter. 2018. Light Absorption of Organic Carbon Emitted from Burning Wood, Charcoal, and Kerosene in Household Cookstoves. *Environmental Pollution* 240: 60–67. doi.org/10.1016/j.envpol.2018.04.085.

Yan, C., M. Zheng, C. Bosch, A. Andersson, Y. Desyaterik, A. P. Sullivan, J. L. Collett, et al. 2017. Important Fossil Source Contribution to Brown Carbon in Beijing during Winter. *Scientific Reports* 7: 1–10. doi.org/10.1038/srep43182.

Yan, J., X. Wang, P. Gong, C. Wang, and Z. Cong. 2018. Review of Brown Carbon Aerosols: Recent Progress and Perspectives. *Science of the Total Environment* 634: 1475–85. doi.org/10.1016/j.scitotenv.2018.04.083.

Yang, M., S. G. Howell, J. Zhuang, and B. J. Huebert. 2009. Attribution of Aerosol Light Absorption to Black Carbon, Brown Carbon, and Dust in China - Interpretations of Atmospheric Measurements during EAST-AIRE. *Atmos. Chem. Phys.* 9 (6): 2035–50. doi.org/10.5194/acp-9-2035-2009.

Yu, Z., G. Magoon, J. Assif, W. Brown, and R. Miake-Lye. 2019. A Single-Pass RGB Differential Photoacoustic Spectrometer (RGB-DPAS) for Aerosol Absorption Measurement at 473, 532,

and 671 Nm. *Aerosol Science and Technology* 53 (1): 94–105. doi.org/10.1080/02786826.2018.1551611.

Zhang, X., Y. H. Lin, J. D. Surratt, and R. J. Weber. 2013. Sources, Composition and Absorption Ångström Exponent of Light-Absorbing Organic Components in Aerosol Extracts from the Los Angeles Basin. *Environ. Sci. Technol.* 47 (8): 3685–93. doi.org/10.1021/es305047b.

Zhang, Y., H. Forrister, J. Liu, J. Dibb, B. Anderson, J. P. Schwarz, A. E. Perring, et al. 2017. Top-of-Atmosphere Radiative Forcing Affected by Brown Carbon in the Upper Troposphere. *Nature Geoscience* 10: 486. doi.org/10.1038/NGEO2960.

Zhao, R., A. K. Y. Lee, L. Huang, X. Li, F. Yang, and J. P. D. Abbatt. 2015. Photochemical Processing of Aqueous Atmospheric Brown Carbon. *Atmos. Chem. Phys*. 15: 6087–6100. doi.org/10.5194/acp-15-6087-2015.

Zhong, M, and M. Jang. 2014. Dynamic Light Absorption of Biomass-Burning Organic Carbon Photochemically Aged under Natural Sunlight. *Atmos. Chem. Phys.* 14: 1517–25. doi.org/10.5194/acp-14-1517-2014.

Zhong, M., and M. Jang. 2011. Light Absorption Coefficient Measurement of SOA Using a UV-Visible Spectrometer Connected with an Integrating Sphere. *Atmospheric Environment* 45 (25): 4263–71. doi.org/10.1016/j.atmosenv.2011.04.082.

# CHAPTER 2

# INVESTIGATING THE DEPENDENCE OF LIGHT-ABSORPTION PROPERTIES OF COMBUSTION CARBONACEOUS AEROSOLS ON COMBUSTION CONDITIONS[1]

[1] Cheng, Z., K. Atwi, T. Onyima, and R. Saleh. 2019. *Aerosol Science and Technology*. 53 (4):419–34. doi:10. 1080/02786826.2019.1566593
Reprinted here with permission of the publisher

**Abstract**

We performed controlled combustion experiments to investigate the dependence of the mass absorption cross-section (MAC) and absorption Ångström exponent (AAE) of combustion carbonaceous aerosol emissions on combustion conditions. Using benzene and toluene as fuels, we obtained a wide range of combustion conditions by varying the combustion temperature and equivalence ratio. We also used nitrogen as a passive diluent to tune the combustion conditions. We calculated MAC and AAE from multi-wavelength light-absorption measurements using a photoacoustic spectrophotometer and aerosol mass loadings estimated from thermal-optical analysis. Starting with relatively low-temperature and fuel-rich combustion conditions and progressively increasing the temperature and/or decreasing the equivalence ratio, we produced emissions with progressive change from weakly absorbing brown carbon (BrC) (MAC at 532 nm ($MAC_{532}$) = 0.24 $m^2/g$ and AAE = 8.6) to strongly absorbing BrC ($MAC_{532}$ = 2.1 $m^2/g$ and AAE = 3.1) to mixtures of black carbon (BC) and strongly absorbing BrC ($MAC_{532}$ = 7.7 $m^2/g$ and AAE = 1.5). These findings indicate that combustion conditions are important in dictating the light-absorption properties of the emitted aerosols. Furthermore, regardless of fuel type and combustion conditions, the emitted aerosols exhibit a unified continuum of light-absorption properties that can be characterized by $MAC_{532}$ and AAE pairs. The $MAC_{532}$ and AAE pairs are well-correlated with the elemental carbon-to-organic carbon ratio (EC/OC), which is a proxy of combustion conditions, confirming previous findings that EC/OC is a practical basis for parameterizing the light-absorption properties of combustion carbonaceous aerosols.

## 2.1. Introduction

Carbonaceous aerosols, including black carbon (BC) and organic aerosol (OA), have significant but poorly constrained impacts on the climate (Bond et al. 2013; IPCC 2013). BC absorbs solar radiation efficiently (Bond and Bergstrom 2006; Moosmüller et al. 2009) and has been established as a leading climate-warming agent, potentially second only to $CO_2$ (Bond et al. 2013; IPCC 2013; Jacobson 2001b). The OA interaction with solar radiation and its impact on the climate are more complicated than those of BC. OA encompasses organic species with highly diverse chemical structures and optical properties. Some OA species absorb solar radiation and are dubbed brown carbon (BrC) (Andreae and Gelencsér 2006). Unlike BC which has relatively well-constrained light-absorption properties (Bond and Bergstrom 2006), the BrC light-absorption properties reported in the literature are highly variable (e.g. Alexander, Crozier, and Anderson 2008; Chakrabarty et al. 2010; Selimovic et al. 2017; Hoffer et al. 2017; Kirchstetter et al. 2004; Saleh et al. 2013, 2014; Utry et al. 2013). BrC is less absorbing than BC as manifested in its smaller wavelength-dependent mass absorption cross-section (MAC) values. However, MAC of BrC exhibits a stronger wavelength dependence, which is usually quantified in terms of the absorption Ångström exponent (AAE). AAE for freshly emitted BC is typically close to unity (Bond et al. 2006; Moosmüller et al. 2011) and can be up to 1.7 when BC is internally mixed with other material (Lack and Cappa, 2010), indicating that BC light absorption is weakly dependent on wavelength in the visible spectrum. On the other hand, the BrC AAE values reported in the literature range between 2 and 9 (Chakrabarty et al. 2010, 2016; Kirchstetter et al. 2004; Lack and Langridge 2013; Sumlin et al. 2018; Sun et al. 2017; Xie, Hays, and Holder 2017; Zhang et al. 2013). The considerable variability in BrC light-absorption properties stems from the diversity in its (poorly understood) chemical composition (Laskin et al. 2015).

Open biomass combustion is the most significant source of BrC (Akagi et al. 2011; Chen and Bond 2010; Kirchstetter and Thatcher 2012; Saleh et al. 2014). Moreover, BrC has been associated with the incomplete combustion of fossil fuels (Du et al. 2014a, 2014b, Olson et al. 2015) as well as secondary organic aerosols from biogenic and anthropogenic precursors (Laskin et al. 2015; Lambe et al. 2013; Rizzo et al. 2011, 2013; Updyke et al. 2012). In this study, we focus on combustion BrC. The light-absorption properties of combustion BrC have been shown to vary with combustion conditions (Chen and Bond 2010; Saleh et al. 2014; Martinsson et al. 2015; ). The combustion conditions are generally governed by the combustion temperature and equivalence ratio ($\Phi$) (Turns 2000), which are challenging to quantify in the real-life uncontrolled combustion that usually produces BrC and BC. To overcome this, previous studies have resorted to proxies to indirectly characterize the combustion conditions, including the relative abundance of elemental carbon (EC) and organic carbon (OC) in the particulate emissions (Vicente et al. 2015; Chen et al. 2014; Shen et al. 2012; Stockwell et al. 2016; Hong et al. 2017). Values of EC-to-OC ratio (EC/OC) reported in the literature for uncontrolled biomass combustion are highly variable (Olson et al. 2015; Roden et al. 2006; Yang et al. 2009; Chen et al. 2014; Bauer et al. 2009; Zhang et al. 2013; Akagi et al. 2011), underscoring the diversity in combustion conditions. EC/OC (Xie, Hays, and Holder 2017; Pokhrel et al. 2016) and BC/OA (Saleh et al. 2014) have been utilized to parameterize the optical properties of combustion carbonaceous aerosols. While EC and BC have different operational definitions that depend on the measurement method, they are closely related and are often used interchangeably (Watson et al. 2005).

In this paper, we systematically explore the effect of combustion conditions on the light-absorption properties (MAC and AAE) of the emitted carbonaceous aerosols by performing a series of combustion experiments controlled at different temperatures and equivalence ratios. We also

assess the efficacy of EC/OC in predicting the light-absorption properties of combustion carbonaceous aerosols.

### 2.2. Methods

In order to generate carbonaceous aerosols of different light-absorption properties, we performed combustion experiments, using benzene and toluene as fuels, controlled at two different combustion temperatures and using various equivalence ratios. We used nitrogen as a passive diluent to fine tune the combustion conditions, as elaborated in section 2.2.1. We performed online measurements of aerosol size distributions and light absorption at each combustion condition. We also collected filter samples for offline thermal-optical analysis to determine the elemental carbon-to-organic carbon ratio (EC/OC) and estimate the aerosol mass loadings. Those were then used to calculate MAC and AAE of the aerosol and develop the parameterizations.

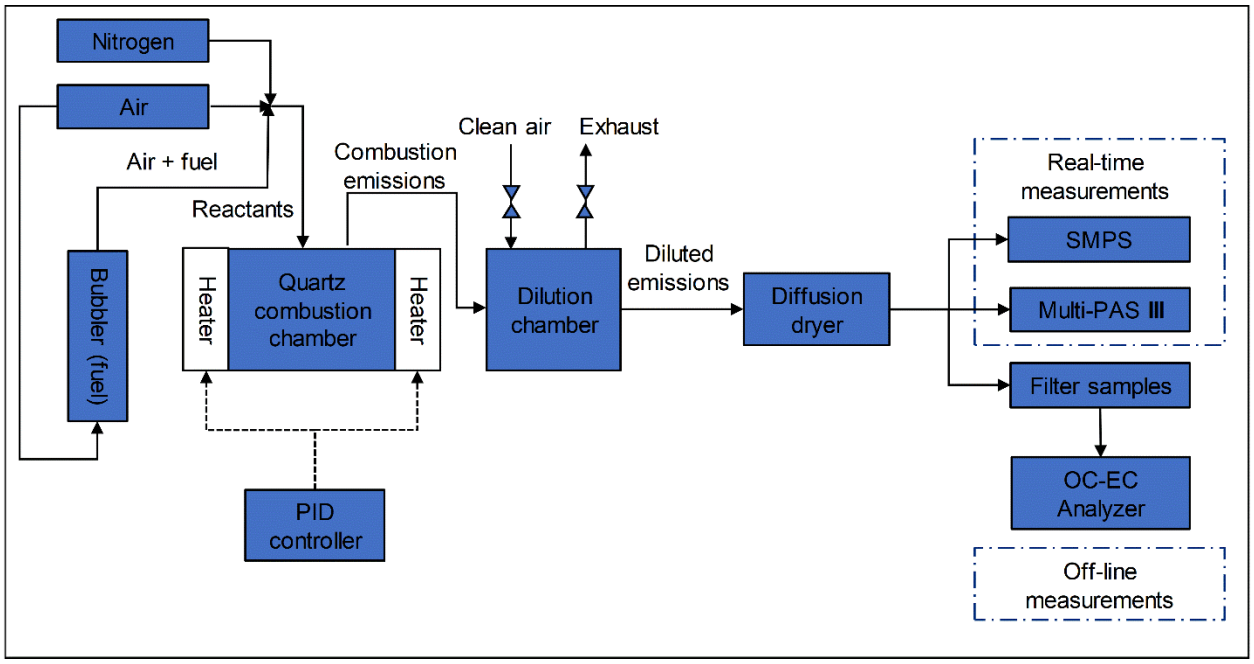


**Figure 2.1.** Schematic of the experimental setup.

### 2.2.1 Combustion experiments

The experimental setup is shown in Figure 2.1. We performed controlled-combustion experiments in a custom-made quartz combustion chamber (ID 50 mm × H 120 mm) enclosed in two 180° semi-cylindrical heating elements (Thermcraft) that could heat the chamber to a maximum temperature of 1200 °C. The temperature inside the chamber was measured by a high-temperature type-K thermocouple (OMEGA, KMQXL-125E-12) and controlled by a PID controller (OMEGA, CNi3244). Fuel was introduced into the combustion chamber by flowing clean air through a bubbler containing the fuel, thus saturating the air with fuel. An additional stream of clean air was mixed with the fuel-saturated stream to adjust the equivalence ratio. We also added a stream of nitrogen to fine-tune the combustion conditions (see below). The flow rates were controlled using mass-flow controllers (DAKOTA, 6AGC1AL55-09AB). We diluted the combustion emissions with clean air in a custom-made glass dilution chamber (ID 150 mm × H 140 mm) to reduce the aerosol concentrations to levels within the detection limits of the real-time instruments. The aerosol was conditioned in a home-built diffusion dryer (ID 10cm × L 65 cm) to a relative humidity lower than 15%.

We performed combustion experiments at two temperatures, 950 °C and 1050 °C. At each temperature, we varied the equivalence ratio ($\Phi$) defined as:

$$\Phi = \frac{(n_{\mathrm{fuel}}/n_{\mathrm{O_2}})}{(n_{\mathrm{fuel}}/n_{\mathrm{O_2}})_{\mathrm{st.}}} \tag{2.1}$$

Where $(n_{\mathrm{fuel}}/n_{\mathrm{O_2}})$ is the fuel-to-oxygen ratio calculated from the relative volumetric flowrates of fuel and air and $(n_{\mathrm{fuel}}/n_{\mathrm{O_2}})_{\mathrm{st.}}$ is the stoichiometric fuel-to-oxygen ratio, which is 0.13 and 0.11 for benzene and toluene, respectively. The volumetric flow rate of the fuel was calculated as:

$$Q_{\text{fuel}} = \frac{P_{\text{sat,fuel}}}{P_{\text{tot}}} Q_{\text{tot}} \quad (2.2)$$

Where $P_{\text{sat,fuel}}$ is the saturation vapor pressure of the fuel, $P_{\text{tot}}$ is the total pressure (1 atm), and $Q_{\text{tot}}$ is the total volumetric flow rate of fuel and air exiting the bubbler. As confirmed by the calculations in the SI, the residence time of a bubble rising in the bubbler (approximately 1 s) is longer than the time required to saturate a single bubble (approximately 0.4 s), confirming that the vapor pressure of the fuel exiting the bubbler is equal to $P_{\text{sat,fuel}}$. We calculated $P_{\text{sat,fuel}}$ using the Antoine equation:

$$P_{\text{sat,fuel}} = 10^{A-\frac{B}{C+T}} \quad (2.3)$$

Where $T$ is the temperature (K) inside the bubbler and $A$, $B$, and $C$ are component-specific constants. $A$ = 4.01814, $B$ = 1203.835, and $C$ = -53.226 for benzene (Willingham et al. 1945) and $A$ = 4.23679, $B$ = 1426.48, and $C$ = -45.957 for toluene (Besley and Bottomley 1974).

Tuning the combustion conditions to achieve specific light-absorption properties (MAC and AAE) has proved to be challenging if relying only on manipulating $\Phi$. The reason is that MAC and AAE are more sensitive to $\Phi$ than the precision at which we can control the relative flow rates of fuel and air. To overcome this issue, we used nitrogen as a passive diluent to fine-tune the combustion conditions. Adding a passive diluent reduces the reaction intensity of the combustible gases (Wagnon and Wooldridge 2014; Li et al. 2015) and thus decreases the combustion efficiency. The effect on the combustion products is similar to making the combustion more fuel rich. However, MAC and AAE are less sensitive to the change in the flow rate of the added nitrogen than to change in the flow rate of the fuel or air (oxygen). Therefore, adjusting the nitrogen flow rate allowed us to accurately control the combustion conditions to achieve the desirable MAC and AAE values.

With the introduction of nitrogen as a passive diluent, however, the previously defined equivalence ratio ($\Phi$) is no longer sufficient to describe the combustion conditions. In other words, two combustion experiments can have the same temperature and $\Phi$ but different combustion efficiencies, and consequently different combustion products, if one of the experiments involves adding a passive diluent (see SI Table S2.1). Hence, to present the light-absorption properties as a function of combustion conditions, we define a modified equivalence ratio ($\Phi$') that captures the effect of the passive diluent (nitrogen) in decreasing the combustion efficiency. Adding nitrogen has a similar effect on the combustion efficiency and the aerosol light-absorption properties as reducing oxygen. Therefore, we define $\Phi$' as:

$$\Phi' = \frac{n_{fuel}/n_{\mathrm{O}_2\,hyp}}{(n_{\mathrm{fuel}}/n_{\mathrm{O}_2})_{st.}} \tag{2.4}$$

Where $n_{fuel}/n_{\mathrm{O}_2\,hyp}$ is the fuel-to-oxygen ratio corresponding to a hypothetical oxygen flow rate ($Q_{\mathrm{O}_2\mathrm{hyp}}$) that is reduced compared to the actual oxygen flow rate.

In order for the hypothetical reduction in the oxygen flow rate to capture the effect of the added nitrogen, it should be proportional to the added nitrogen flowrate ($Q_{\mathrm{N}_2}$). To achieve that, we calculate $Q_{\mathrm{O}_2\mathrm{hyp}}$ by scaling the actual oxygen flow rate as follows:

$$Q_{\mathrm{O}_2\mathrm{hyp}} = (\frac{x'_{\mathrm{O}_2}}{x_{\mathrm{O}_2}})\, Q_{\mathrm{O}_2} \tag{2.5}$$

Where $x_{\mathrm{O}_2}$ = 0.21 is the mole fraction of oxygen in air, $Q_{\mathrm{O}_2}$ is the actual oxygen flowrate, and $x'_{\mathrm{O}_2}$ is the mole fraction of oxygen in the system containing air and the added nitrogen:

$$x'_{\mathrm{O}_2} = Q_{\mathrm{O}_2}/(Q_{\mathrm{air}} + Q_{\mathrm{N}_2}) \tag{2.6}$$

Where $Q_{\mathrm{air}}$ is the total air flowrate entering the combustion chamber. Combining equations (2.1) and (2.4) – (2.6), we obtain:

$$\Phi' = \Phi\left(1 + \frac{Q_{\mathrm{N_2}}}{Q_{\mathrm{air}}}\right) \tag{2.7}$$

We stress that $\Phi$' serves as a convenient parameter to qualitatively represent changes in combustion conditions when nitrogen is added as a passive diluent (see Figure 2.3) based on our observation that adding nitrogen moves the combustion products in the same direction as making the combustion more fuel rich. However, we do not imply that adding nitrogen has the same effect on combustion chemistry as increasing the fuel-to-oxygen ratio. In other words, for two combustion systems A and B (with B involving additional nitrogen as a passive diluent), we do not imply that A and B exhibit the same combustion chemistry if $\Phi_{\mathrm{A}} = \Phi'_{\mathrm{B}}$.

### 2.2.2. Light-absorption and size-distribution measurements

At each combustion condition, we measured real-time aerosol absorption coefficients ($b_{abs}$, $Mm^{-1}$) at 422, 532, and 782 nm using a 3-wavelength multi-pass photoacoustic spectrophotometer (Multi-PAS III) built by Geoffrey Smith's group (University of Georgia) following the same design as Fischer and Smith (2018). This design has the advantage that a single wavelength calibration is applicable to all wavelengths (Fischer and Smith 2018). However, we performed our calibrations at 422 nm and 532 nm to ensure consistency. The calibration was performed daily with $NO_2$ (1-5 ppm in $N_2$) using $NO_2$ absorption cross-section values of $5.79\times10^{-19}$ $cm^2$ /molecule and $1.47\times10^{-19}$ $cm^2$ /molecule at 422 nm and 532 nm, respectively (Vandaele 2002). We obtained the instrument calibration coefficient as the average of the two calibration coefficients. With the absence of reliable $NO_2$ absorption cross-section data at 782 nm, we opted to exclude the 782 nm laser from

the calibration process. The Multi-PAS III has a detection limit better than 0.6 $Mm^{-1}$ (Fischer and Smith 2018). This detection limit is much smaller than the absorption coefficients observed in our experiments, which were typically larger than 10, 100, and 500 $Mm^{-1}$ at 782, 532, and 422 nm, respectively.

We measured the aerosol electrical-mobility size distributions within the size range 10-550 nm using a Scanning Mobility Particle Sizer (SMPS, TSI). The SMPS includes an Electrostatic Classifier (TSI, Model 3082) with a long Differential Mobility Analyzer (DMA, TSI, Model 3081A00), an Advanced Aerosol Neutralizer (TSI, Model 3088), and a Condensation Particle Counter (CPC, TSI, Model 3772). Typical number and mass size distributions of combustion particles are shown in Figure 2.2a and Figure 2.2b, respectively. The particle size distributions exhibited a strong dependence on the combustion conditions. As shown in Figure 2.2, the particles generated in our combustion experiments fall into two general regimes: pure organics (BrC) and mixed BrC and BC (BrC+BC). For combustion conditions that produced only BrC, the particles were relatively small and exhibited a unimodal size distribution with mass-mode diameters typically smaller than 60 nm. On the other hand, combustion conditions that produced BrC+BC were characterized by bimodal particle size distributions, with the mass concentration being dominated by the larger particles (Figure 2.2b). As the mass distributions of the BrC+BC particles were not adequately captured within the SMPS measurement window, we applied lognormal fits to obtain the missing part of the distributions (Figure 2.2b).

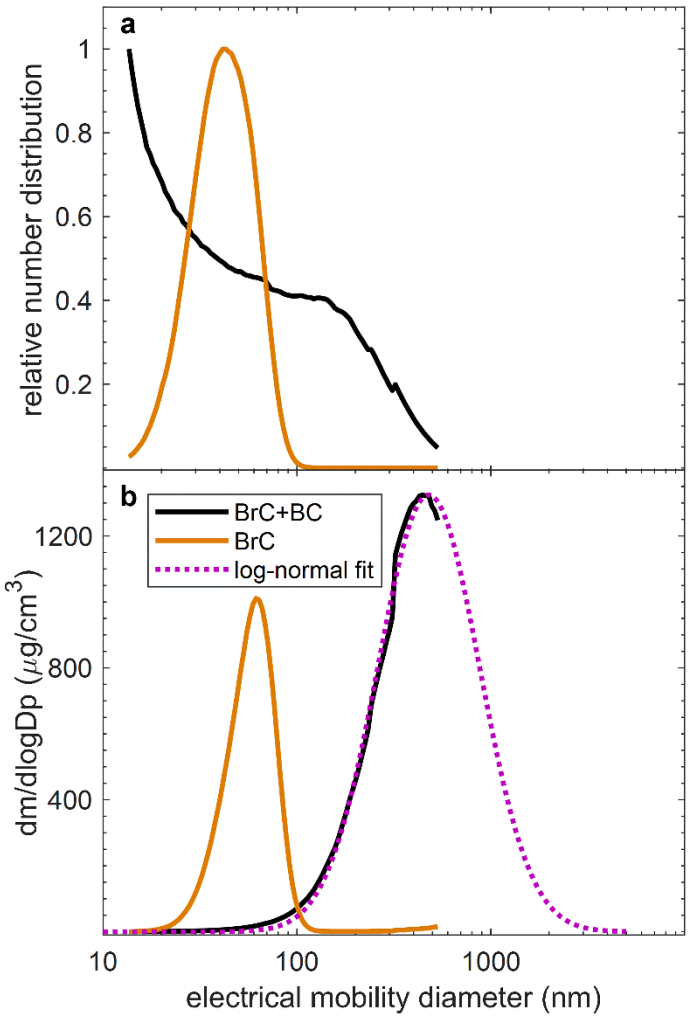


**Figure 2.2.** Typical SMPS (**a**) number and (**b**) mass (assuming a density of 1g/cm$^3$) size distributions of combustion particles containing only BrC (brown) and BrC+BC (black). The SMPS measurement window does not adequately capture the BrC+BC mass distribution. To obtain the missing part of the distributions, we used log-normal fits (dotted magenta line).

### 2.2.3. Determining aerosol mass concentrations and elemental-carbon / organic-carbon ratios

For each experiment, we measured the integrated total carbon (TC) mass loading on the filter and the elemental carbon-to-organic carbon ratio (EC/OC) using an OC-EC analyzer (Sunset

Laboratory Inc, Portland, OR, Model 5L) operated using the IMPROVE-A protocol, which has been commonly employed in OC-EC studies (Chow et al. 2001, 2007; Karanasiou et al. 2015; Salako et al. 2012). We collected the combustion particles at a flow rate of 6 standard liters per minute (SLPM) on 47 mm quartz fiber filters pre-baked at 200 ˚C for 12 hours. The detection limit of the OC-EC analyzer specified by the manufacturer is 0.1 μg/cm$^2$. Therefore, we targeted loadings on the order of 10 μg /cm$^2$. The active collection area on each quartz fiber filter is approximately 11.3 cm$^2$. Hence, the loading corresponds to 113 μg /filter. With typical aerosol concentrations of 300 μg /cm$^3$, the sample collection time was approximately 1 hour. As shown in SI Figure S2.1, the aerosol light-absorption properties and the particle concentrations (i.e., integrated size distributions) were stable during each sampling period to within 5% and 10%, respectively.

We utilized the OC-EC analysis to obtain EC/OC for each experiment, which we used to parameterize the light-absorption properties of the aerosol (see section 2.3.3). Estimating EC/OC collected on quartz filters is prone to both negative and positive artifacts when the aerosol sample contains volatile and semi-volatile organic compounds (VOCs and SVOCs) (Turpin et al. 1994; Turpin et al. 2000; Cheng et al. 2010). The negative artifact is caused by evaporation of SVOCs collected on the filter during the time between the end of sampling and beginning of the OC-EC analysis. To minimize this artifact, we performed the OC-EC analysis immediately after sampling (i.e. the filters were not stored before OC-EC analysis). The positive artifact is caused by adsorption of VOCs and vapor-phase SVOCs on the quartz filter, which leads to overestimating the OC mass. To minimize this artifact, we employed the bare-quartz (BQ) and quartz-behind-Teflon (QBT) method (Ma et al. 2016; Chen and Bond 2010; Gao et al. 2006; Kirchstetter et al. 2001; Subramanian et al. 2004). In addition to the main quartz filter (BQ), we added another

sampling line with a quartz filter installed downstream of a Teflon filter (QBT). This method assumes that the Teflon filter exhibits minimal adsorption of VOCs and vapor-phase SVOCs, and those are adsorbed on the QBT filter. Therefore, the particle-phase OC can be estimated as the difference between the OC collected on the QB and QBT filters.

We also used the measured TC to estimate the average aerosol mass loading $C_p$ (μg/m$^3$) during an experiment, which we used to calculate MAC (section 2.2.4). This was done using

$$C_p = \frac{m_{TC}}{t \cdot Q} \quad (2.8)$$

Where $m_{TC}$ is the total mass loading on the filter, $Q$ is the sample collection flow rate, and $t$ is the sample collection time.

Equation (2.8) assumes that the aerosol mass is dominated by carbon (TC). This assumption is justified as follows: We have previously shown using laser-desorption ionization mass spectrometry that the organic aerosol emitted at similar combustion conditions was dominated by molecules with sizes typically larger than 300 Da (and up to several 1000 Da) and with signatures indicative of a strong presence of polycyclic aromatic hydrocarbons (PAHs) (Saleh et al. 2018). The mass of these large organic molecules is dominated by carbon.

To validate this calculation of mass loading, we combined the aerosol particle mass loading measurements from OC-EC analysis and the volume concentrations obtained from integrating SMPS electrical-mobility size distributions (section 2.2.2) to calculate particle effective densities:

$$\rho_{eff} = \frac{C_p}{V_p} \quad (2.9)$$

Where $C_p$ is the particle mass loading and $V_p$ is the SMPS integrated volume concentration.

As described in section 2.2.2, depending on the combustion conditions, the particles were either pure organic (BrC) or mixed BrC+BC. The pure BrC particles exhibit compact, near-spherical morphologies (Saleh et al. 2018), and, therefore, their effective density calculated using equation (2.9) corresponds to the actual material density. We obtained densities between 1.2 and 1.5 g/cm$^3$ for the pure BrC particles (see SI Table S2.1). These values are in good agreement with the values reported in the literature for organic aerosol (Cross et al. 2007; Schmid et al. 2009), thus validating our OC-EC method to calculate particle mass loadings.

The OC-EC method is especially useful for the BrC+BC particles because they exhibit irregular morphologies (Saleh et al. 2018) and are expected to be composed of a complex mix of internally and externally mixed particles. This makes it challenging to estimate their mass concentration by relying on SMPS size distributions with the absence of detailed information on mixing state and morphology. To validate the mass-loading calculations for the BrC+BC particles, we combined OC-EC mass loadings with integrated SMPS volume concentrations to obtain distribution-average shape factors ($\chi$) of the BrC+BC particles and compared them with values reported in the literature for BC-containing particles. $\chi$ can be calculated as (Sarangi et al. 2016; Rissler et al. 2014; Malloy et al. 2009):

$$\chi = \sqrt[3]{\frac{\rho_p}{\rho_{eff}}} \tag{2.10}$$

Where $\rho_p$ is the material density of the aerosol and $\rho_{eff}$ is the effective density obtained from equation (2.9). For the BrC+BC particles, we estimated $\rho_p$ as the weighted average of BrC (1.3 ± 0.1 g/cm$^3$, estimated based on the average BrC density from the OC-EC analysis) and BC (1.8 ±

0.1 g/cm$^3$) (Bond et al. 2013) assuming that the BC-to-BrC ratio is equal to the EC-to-OC ratio obtained from the EC/OC analysis:

$$\rho_{\mathrm{p}} = \rho_{\mathrm{BrC}} \frac{m_{\mathrm{OC}}}{m_{\mathrm{TC}}} + \rho_{\mathrm{BC}} \frac{m_{\mathrm{EC}}}{m_{\mathrm{TC}}} \quad (2.11)$$

The $\chi$ values we obtained for the BrC+BC particles range between 1.09 and 2.63 (the complete list of values is given in SI Table S2.1). This range overlaps with $\chi$ values for BC-containing particles reported in the literature, with the variability attributed to differences in morphology and mixing state (Slowik et al. 2004; Ahern et al. 2016; Slowik et al. 2007). Furthermore, the $\chi$ values are well correlated with EC/OC (SI Figure S2.2). This correlation is expected because the increase in EC/OC is associated with deviation from sphericity ($\chi$ = 1) and is in qualitative agreement with previous reports (Slowik et al. 2007; Qiu et al. 2012; Zhang et al. 2016; Ahern et al. 2016; Schnitzler et al. 2014).

### 2.4. Light-absorption properties calculations

We quantified the light-absorption properties using the wavelength-dependent mass-absorption cross-section (MAC, m$^2$/g). MAC follows an approximate power-low wavelength dependence and can, therefore, be represented using two parameters: MAC at a particular wavelength ($\lambda$), which we choose to be 532 nm (the mid-wavelength of the Multi-PAS III), and the absorption Ångström exponent (AAE):

$$\mathrm{MAC} = \mathrm{MAC}_{532} \left(\frac{532}{\lambda}\right)^{\mathrm{AAE}} \quad (2.12)$$

It is important to note that MAC and AAE depend on particle size and morphology (Lack and Cappa 2010; Bond et al. 2006; Soewono and Rogak 2013; Poudel et al. 2017) and are thus not true

intensive properties. However, they are commonly employed because they can be readily calculated from light-absorption measurements. On the other hand, retrieving refractive indices, which are the fundamental optical properties, requires involved optical calculations. The retrieval process is especially challenging for non-spherical particles, where the commonly used Mie calculations are not suitable, and the optical calculations require detailed knowledge of the morphology (Adachi, Chung, and Buseck 2010; Lack and Cappa 2010; Bond and Bergstrom 2006; Moosmüller, Chakrabarty, and Arnott 2009; Sorensen 2001). With the absence of morphology information for the mixed BrC+BC particles in this study, we elected to represent the light-absorption properties using MAC and AAE. For each experiment (i.e. combustion condition), we calculated MAC at 422, 532, and 782 nm as:

$$\mathrm{MAC} = \frac{b_{\mathrm{abs}}}{C_{\mathrm{p}}} \tag{2.13}$$

Where $b_{\mathrm{abs}}$ is the experiment-mean absorption coefficient measured using the Multi-PAS III (section 2.2.2), and $C_{\mathrm{p}}$ is the mean particle mass loading obtained from OC-EC measurements (section 2.2.3).

The AAE for each experiment was obtained by fitting a power-law function to the wavelength-dependent MAC (equation 2.12) measured at the three wavelengths (422, 532, and 782 nm). Therefore, the AAE obtained here is an effective AAE that represents the wavelength dependence of measured aerosol absorption over the visible spectrum.

## 2.3. Results and discussion

### 2.3.1. The dependence of aerosol light-absorption properties on combustion conditions

The obtained dependence of MAC at 532 nm ($MAC_{532}$) and AAE on combustion conditions is summarized in Figures 2.3a and 2.3b, respectively. In each panel, we show the results for toluene and benzene combustion at temperatures of 950 °C and 1050 °C. As described in section 2.2.2, depending on the combustion conditions, the emitted particles fall into two general regimes: pure BrC and mixed BrC+BC. To visually distinguish between the two regimes, we added a grey background shading to the BrC+BC region in Figure 2.3. For both fuels and combustion temperatures, the $MAC_{532}$ and AAE values show similar trends as a function of $\Phi$'. Starting with largest $\Phi$', the particles have small $MAC_{532}$ (as small as 0.24 $m^2/g$) and large AAE (as large as 8.6) values, which are similar to values frequently observed for weakly absorbing BrC in smoldering-biomass emissions (Chakrabarty et al. 2010; Chen and Bond 2010; Chakrabarty et al. 2016; Li et al. 2016). As $\Phi$' decreases, $MAC_{532}$ increases and AAE decreases, which is indicative of darker BrC. The $MAC_{532}$ (2.09 $m^2/g$) and AAE (3.1) values for the darkest BrC in this study are similar to those observed for dark biomass-burning BrC (Saleh et al. 2014; Kirchstetter et al. 2004) and tar balls (Hoffer et al. 2016, 2017). As expected, the BrC+BC particles exhibit larger $MAC_{532}$ and smaller AAE values, and as the BC content increases (see section 2.3.3), they converge to the values frequently reported for BC ($MAC_{532}$ = 7-8 $m^2/g$ and AAE close to unity) (Bond and Bergstrom 2006).

Even though the trends of $MAC_{532}$ and AAE versus $\Phi$' are similar, the values are dependent on fuel type and combustion temperature. To investigate this dependence, it is helpful to qualitatively define combustion efficiency as the level of completeness of the combustion reaction. This

definition is consistent with the definition of the "modified combustion efficiency," quantified as the ratio of CO to $CO_2$ in the emissions, which has been previously employed to characterize combustion conditions (Selimovic et al. 2017; Xie et al. 2017; Akagi et al. 2011; Aurell et al. 2015; Sun et al. 2018). The combustion efficiency is governed by fuel type, combustion temperature, and $\Phi$'. Specifically, for a certain fuel, the combustion efficiency increases with increasing temperature and/or decreasing $\Phi$'. If the BC-formation threshold is located in the combustion-efficiency space, reducing the combustion efficiency below this point produces pure BrC particles, which are the organic precursors of BC (Saleh et al. 2018). The darkness of these BrC particles varies proportionally with combustion efficiency (Saleh et al. 2018). This behavior is evident in Figure 2.3 for the pure BrC particles. For both benzene and toluene combustion, the emitted BrC is darker (larger $MAC_{532}$ and smaller AAE) for decreasing $\Phi$' at a constant combustion temperature or increasing combustion temperature at a constant $\Phi$'.

Figure 2.3 also reveals a dependence of combustion efficiency on fuel type. In the pure BrC regime, benzene combustion emitted darker BrC than toluene combustion for the same combustion temperature and $\Phi$'. It is important to note that this result does not indicate that benzene and toluene emit different types of BrC but rather that benzene combustion progresses more efficiently towards the BC-formation threshold than toluene combustion. Put in other words, both benzene and toluene produce the same BrC continuum, but for the same combustion temperature and $\Phi$', benzene produces BrC that is further along the continuum (more mature) than toluene. This assertion is further discussed in section 2.3.2.

It is important to note that approaching the BC-formation threshold (shaded regions in Figure 2.3a and 2.3b) marks a convergence in $MAC_{532}$ and AAE for both fuels and combustion temperatures.

The reason is that BC is the end product to which the soot-formation process converges, which leads to its relatively uniform, fuel-independent and temperature-independent light-absorption properties.

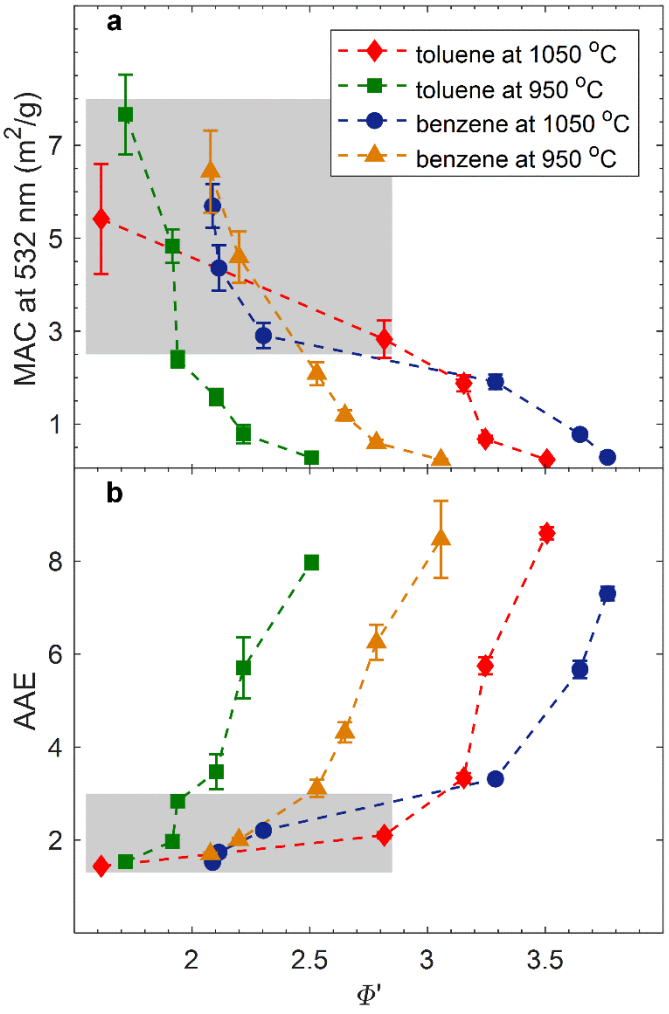


**Figure 2.3.** The dependence of light-absorption properties of the carbonaceous aerosols emitted from benzene and toluene combustion on the modified equivalence ratio ($\Phi$' – see derivation in section 2.2.1) for combustion temperatures of 950 °C and 1050°C. The shaded regions correspond to combustion conditions that produced mixed BrC+BC particles, and the non-shaded regions correspond to conditions that produced pure BrC particles. **a)** The mass absorption cross-section

at 532 nm ($MAC_{532}$). **b)** The absorption Ånsgström exponent (AAE). Error bars represent measurement uncertainty (see uncertainty analysis in SI). The $MAC_{532}$ reported here is calculated based on the correction for adsorbed VOCs as described in section 2.2.2. For reference, a similar plot is presented in SI Figure S2.3 without correcting for the adsorbed VOCs.

### 2.3.2. The continuum of light-absorption properties

As shown in Figure 2.4, the data points from all the combustion experiments in Figure 2.3 collapse on the same continuum when their histories (fuel and combustion conditions) are ignored and are instead presented in AAE versus $MAC_{532}$ space. This result supports our assertion in section 2.3.1 that the dependence of the light-absorption properties on fuel type, combustion temperature, and $\Phi$' observed in Figure 2.3 is not a manifestation of diversity in formation pathways. It rather indicates that combinations of fuel type, combustion temperature, and $\Phi$' dictate how far the soot-formation process progresses along the same continuum. We stress that for the four fuel-type/combustion-temperature combinations in this study (benzene at 1050 °C, benzene at 950 °C, toluene at 1050 °C, and toluene at 950 °C), we could vary $\Phi$' to produce wide and overlapping portions of the continuum that spanned weakly absorbing BrC to highly absorbing BrC to mixtures of BC and highly absorbing BrC (Figure 2.4). However, combustion temperature can be a limiting factor. For instance, regardless of fuel type and $\Phi$', low combustion temperatures would potentially produce only BrC in the weakly absorbing part of the continuum.

We have previously introduced the continuum of light-absorption properties of combustion carbonaceous aerosol produced through the soot-formation route, the brown-black continuum, in Saleh et al. (2018). In that study, we presented experimental evidence of this continuum for BrC and posited that the continuum extended into the BC regime. Here, we present experimental

evidence that it indeed applies to both the BrC and BC regimes. As shown in Figure 2.4, the same trend set by the $MAC_{532}$-AAE pairs upon progression from light to dark BrC continues beyond the BC-formation threshold. This implies that in practice, the light-absorption properties of combustion carbonaceous aerosol produced via the soot-formation route, which includes both BrC and BC, as well as their mixtures, can be parameterized within a unified framework.

For completeness, we reproduced Figure 2.4 but for AAE between 532 nm and 422 nm ($AAE_{532-422}$) and between 782 nm and 532 nm ($AAE_{782-532}$). Figure S2.5 in the SI shows the effective AAE over the visible spectrum (i.e. what we simply refer to as AAE in this paper) versus $AAE_{532-422}$ and $AAE_{782-532}$. As expected, $AAE_{782-532} < AAE < AAE_{532-422}$. The reason is that each sample is composed of components with varying light-absorption properties, and the darker components (large MAC, small AAE) dominate the absorption in the long-visible range while the contribution of the lighter components (small MAC, large AAE) to absorption increases in the short-visible range. As shown in Figure S2.6, while there are differences in the values of effective AAE, $AAE_{532-422}$, and $AAE_{782-532}$, they all exhibit the same exponential decay trend as a function of MAC.

To close this section, a discussion of the potential universality of the brown-black continuum (Figure 2.4) is in order. Theoretical and experimental investigations suggest that the soot-formation route, which involves sequential organization of aromatic rings into large PAHs (Michelsen 2017), is expected to be fairly fuel-independent (Lautenberger et al. 2005; Johansson et al. 2018). Therefore, we expect that the light-absorption properties of the components along this route, i.e. the brown-black continuum, to also be fuel-independent. In this study, we present evidence of fuel independence by showing that benzene and toluene combustion produce the same brown-black continuum (Figure 2.4). However, more structurally diverse and complex fuels (e.g.

solid fuels) need to be investigated in order to scrutinize the universality of the brown-black continuum. Furthermore, the brown-black continuum applies for carbonaceous particles produced through the soot-formation route. However, different classes of BrC have been observed in combustion emissions, especially biomass combustion, including nitroaromatic compounds (Budisulistiorini et al. 2017; Zhang et al. 2013; Iinuma et al. 2010; Lin et al. 2016; Claeys et al. 2012), charge transfer complexes (Phillips and Smith 2014, 2015), and tar balls (Hoffer et al. 2017; Chakrabarty et al. 2010; Alexander et al. 2008). An understanding of the relative contributions of the different classes to the total BrC budget is still lacking (Laskin et al. 2015), and it remains to be seen whether the light-absorption properties of these types of BrC fall on the same continuum as the BrC produced in this study through the soot-formation route.

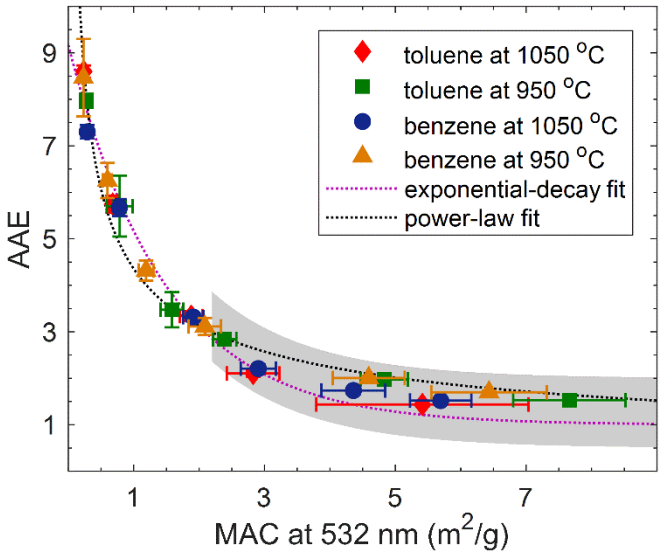


**Figure 2.4**. The mass absorption cross-section at 532 nm ($MAC_{532}$) versus the absorption Ånsgström exponent (AAE) for all the data points in Figure 2.3. The shaded region corresponds to mixed BrC+BC particles, and the non-shaded region corresponds to pure BrC particles. The dotted magenta line is an exponential-decay fit (AAE = (8.17±0.58) exp[(-0.67±0.09) $MAC_{532}$] +1, $R^2$=0.9709). The dotted black line is a power-law fit (AAE = (4.37±0.22) $MAC_{532}^{-0.48\pm0.04}$,

$R^2$=0.9686). Error bars represent measurement uncertainty (see uncertainty analysis in SI). The $MAC_{532}$ reported here is calculated based on the correction for adsorbed VOCs as described in section 2.2.2. For reference, a similar plot is presented in SI Figure S2.4 without the adsorbed VOCs correction.

### 2.3.3. Parameterizing the light-absorption properties as a function of EC/OC

The ratio of elemental carbon to organic carbon (EC/OC) in combustion emissions can be readily calculated from emissions inventories (Petzold et al. 2013; Chow et al. 2012; Caserini et al. 2013; Bond et al. 2004). This makes EC/OC an attractive proxy of combustion conditions for parameterizing aerosol optical properties obtained from laboratory and field measurements for use in large-scale climate calculations. Figure 2.5 shows EC/OC, determined as described in section 2.2.3, versus $\Phi$' for all combustion experiments. For each fuel, EC/OC increases with increasing combustion efficiency (increasing temperature and/or decreasing $\Phi$'), confirming that EC/OC is a good indicator of combustion conditions.

EC/OC and the closely related BC/OA have been previously shown to correlate with the carbonaceous aerosol light-absorption properties (Saleh et al. 2014; Xie et al. 2017; Pokhrel et al. 2016). More specifically, the carbonaceous aerosol becomes darker with increasing EC/OC. Differentiating between two aspects of this correlation is important. The first aspect is that the increase in carbonaceous aerosol darkness with EC/OC is partly attributed to the fractional increase of the highly absorptive EC (or BC) in the aerosol. The second aspect is that as the EC/OC (or BC/OA) increases, the organics aerosol (or BrC) becomes darker as shown by Saleh et al. (2014). This is consistent with the brown-black continuum (Saleh et al. 2018) because the more conducive

the combustion conditions are to forming BC, the more skewed the BrC components are to the darker end of the continuum.

Our controlled-combustion experiments enable us to distinguish the dark BrC from BC and show that the light-absorption properties of BrC and BC can be combined in a unified parameterization. To do that, we exploited a measurement artifact of the thermal-optical method used to determine EC/OC. Specifically, a fraction of OC is usually pyrolyzed during the step-increase in temperature in the OC-analysis stage (Bauer et al. 2009; Chow et al. 2001; Jeong et al. 2004). This is manifested as an increase in attenuation of a 633 nm laser, which is continuously monitored during the analysis. The pyrolyzed OC is quantified as the amount of carbon measured after the introduction of $O_2$ (i.e. during the EC-analysis stage) until reflectance returns to its initial value at the beginning of the OC analysis phase ( Karanasiou et al. 2015; Chow et al. 2007; Chow et al. 2004; Chow et al. 2001). An implicit assumption in the pyrolyzed-OC correction process is that only EC absorbs at 633 nm. Therefore, OC (or BrC) that absorbs appreciably at 633 nm is inaccurately registered as EC, and for the same amount of BrC, the registered amount of "artificial EC" increases with increasing BrC darkness. As shown in Figure 2.6, for the pure BrC particles in our experiments, $MAC_{532}$ and AAE are well correlated with the artificial EC/OC. The correlation extends into the BC-formation regime (i.e., when the registered EC includes "true EC"), where $MAC_{532}$ increases and AAE decreases due to the formation of both BC and highly absorptive BrC.

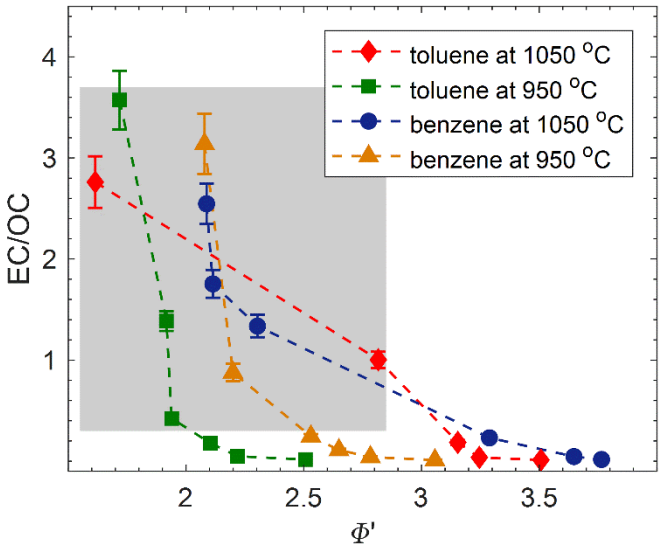


**Figure 2.5.** Elemental carbon-to-organic-carbon ratio (EC/OC) versus modified equivalence ratio ($\Phi$') for all experiments. The shaded region corresponds to mixed BrC+BC particles, and the non-shaded region corresponds to pure BrC particles. Error bars represent measurement uncertainty (see uncertainty analysis in SI). The EC/OC reported here is corrected for adsorbed VOCs as described in section 2.2.2. For reference, a similar plot is presented in SI Figure S2.7 with uncorrected EC/OC.

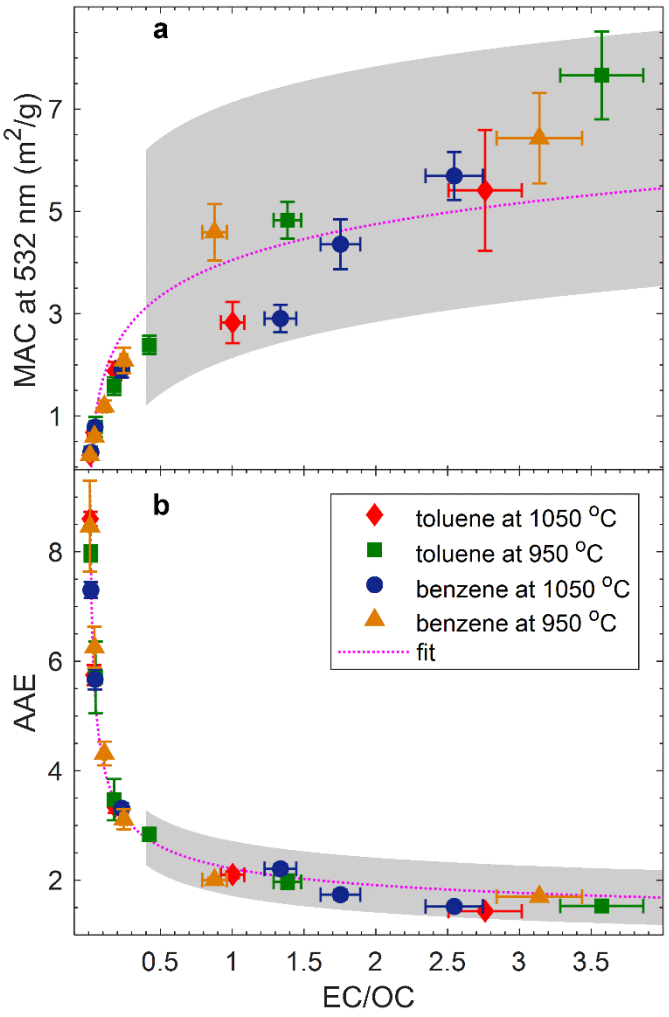


**Figure 2.6.** Parameterizing the light-absorption properties of combustion carbonaceous aerosols as a function of EC/OC. The shaded regions correspond to mixed BrC+BC particles and the non-shaded regions correspond to pure BrC particles. The EC/OC reported here is corrected for adsorbed VOCs as described in section 2.2.2. For reference, a similar plot is presented in SI Figure S2.8 with uncorrected EC/OC. **a)** Mass absorption cross-section at 532 nm ($MAC_{532}$) versus EC/OC. The dotted magenta line is a fit with the equation: $MAC_{532} = (1.04\pm0.20)\ \log(EC/OC) + (4.13\pm0.52)$, $R^2 = 0.8431$. **b)** Absorption Ångström exponent (AAE) versus EC/OC. The dotted magenta line is a fit with the equation: $AAE = (1.21\pm0.14)\ EC/OC^{-0.4155\pm0.03} + 1$, $R^2 = 0.9850$. Error bars represent measurement uncertainty (see uncertainty analysis in SI).

## 2.4. Conclusions

By performing controlled-combustion experiments that span both pure BrC as well as mixed BrC+BC formation regimes, we show that the light-absorption properties in both regimes follow the brown-black continuum introduced by Saleh et al. (2018). At the same combustion conditions, the two fuels used in this study (benzene and toluene) produce BrC with different optical properties, with benzene consistently producing darker BrC. However, this difference is not a manifestation of differences in formation pathways but is rather an indication that the soot-formation process in benzene combustion progresses more efficiently than in toluene combustion. When presented in optical-properties space, the BrC and BC produced by both fuels fall on the same brown-black continuum characterized by pairs of increasing MAC at 532 nm ($MAC_{532}$) and decreasing AAE.

For both the pure BrC and mixed BrC+BC regimes, $MAC_{532}$ increases and AAE decreases with increasing EC/OC, which is an indicator of combustion efficiency. Systematically traversing the two regimes using controlled-combustion experiments shows that this correlation is due to both the formation of progressively darker BrC as well as the increase in BC fraction with increasing combustion efficiency. This finding provides a fundamental basis for previous reports on the observed dependence of light-absorption properties on EC/OC. It also suggests that a unified framework can potentially be implemented to parameterize the light-absorption properties of carbonaceous aerosols produced through the soot-formation route in both the pure-organic (e.g., smoldering) and BC-forming (e.g., flaming) combustion regimes.

**Acknowledgments**

The authors gratefully acknowledge Dr. Geoffery Smith (Department of Chemistry, University of Georgia) and his research group for designing and building Multi-PAS III used in this study, as well as the Scientific Glass Blowing Shop (University of Georgia) for building the quartz combustion chamber. Financial support was provided by the National Science Foundation, Division of Atmospheric and Geospace Sciences (AGS-1748080).

## References


Adachi, K., S. H. Chung, and P. R. Buseck. 2010. Shapes of Soot Aerosol Particles and Implications for Their Effects on Climate. *J. Geophys. Res.* 115 (15): D15206. doi.org/10.1029/2009JD012868.

Ahern, A. T., R. Subramanian, G. Saliba, E. M. Lipsky, N. M. Donahue, and R. C. Sullivan. 2016. Effect of Secondary Organic Aerosol Coating Thickness on the Real-Time Detection and Characterization of Biomass-Burning Soot by Two Particle Mass Spectrometers. *Atmos. Meas. Tech.* 9 (12): 6117–37. doi.org/10.5194/amt-9-6117-2016.

Akagi, S. K., R. J. Yokelson, C. Wiedinmyer, M. J. Alvarado, J. S. Reid, T. Karl, J. D. Crounse, and P. O. Wennberg. 2011. Emission Factors for Open and Domestic Biomass Burning for Use in Atmospheric Models. *Atmos. Chem. Phys.* 11 (9): 4039–72. doi.org/10.5194/acp-11-4039-2011.

Alexander, D. T. L., P. A. Crozier, and J. R. Anderson. 2008. Brown Carbon Spheres in East Asian Outflow and Their Optical Properties. *Science* 321 (5890): 833–36. doi.org/10.1126/science.1155296.

Andreae, M. O., and A. Gelencsér. 2006. Black Carbon or Brown Carbon? The Nature of Light-Absorbing Carbonaceous Aerosols. *Atmos. Chem. Phys.* 6 (10): 3131–48. doi.org/10.5194/acp-6-3131-2006.

Aurell, J., B. K. Gullett, and D. Tabor. 2015. Emissions from Southeastern U.S. Grasslands and Pine Savannas: Comparison of Aerial and Ground Field Measurements with Laboratory Burns. *Atmospheric Environment* 111: 170–78. doi.org/10.1016/j.atmosenv.2015.03.001.

Bauer, J. J., X. Y. Yu, R. Cary, N. Laulainen, and C. Berkowitz. 2009. Characterization of the Sunset Semi-Continuous Carbon Aerosol Analyzer. *J. Air & Waste Manage. Assoc.* 59 (7): 826–33. doi.org/10.3155/1047-3289.59.7.826.

Besley, L. M., and G. A. Bottomley. 1974. Vapour Pressure of Toluence from 273.15 to 298.15 K. *J. Chem. Thermodynamics* 6 (6): 577–80. doi.org/10.1016/0021-9614(74)90045-7.

Bond, T. C., and R. W. Bergstrom. 2006. Light Absorption by Carbonaceous Particles: An Investigative Review. *Aerosol Science and Technology* 40 (1): 27–67. doi.org/10.1080/02786820500421521.

Bond, T. C., S. J. Doherty, D. W. Fahey, P. M. Forster, T. Berntsen, B. J. Deangelo, M. G. Flanner, et al. 2013. Bounding the Role of Black Carbon in the Climate System: A Scientific Assessment. *Geophysical Research Atmospheres* 118 (11): 5380–5552. doi.org/10.1002/jgrd.50171.

Bond, T. C., G. Habib, and R. W. Bergstrom. 2006. Limitations in the Enhancement of Visible Light Absorption Due to Mixing State. *J. Geophys. Res.* 111 (20): D20211. doi.org/10.1029/2006JD007315.

Bond, T. C., D. G. Streets, K. F. Yarber, S. M. Nelson, J. Woo, and Z. Klimont. 2004. A Technology-Based Global Inventory of Black and Organic Carbon Emissions from

Combustion. *J. Geophys. Res.* 109: D14203. doi.org/10.1029/2003JD003697.

Budisulistiorini, S. H., M. Riva, M. Williams, J. Chen, M. Itoh, J. D. Surratt, and M. Kuwata. 2017. Light-Absorbing Brown Carbon Aerosol Constituents from Combustion of Indonesian Peat and Biomass. *Environ. Sci. Technol.* 51 (8): 4415–23. doi.org/10.1021/acs.est.7b00397.

Caserini, S., S. Galante, S. Ozgen, S. Cucco, K. De Gregorio, and M. Moretti. 2013. A Methodology for Elemental and Organic Carbon Emission Inventory and Results for Lombardy Region, Italy Stefano. *Sci Total Environ.* 450–451: 22–30. doi.org/10.1016/j.scitotenv.2013.01.073.

Chakrabarty, R. K., M. Gyawali, R. L. N. Yatavelli, A. Pandey, A. C. Watts, J. Knue, L. W. A. Chen, et al. 2016. Brown Carbon Aerosols from Burning of Boreal Peatlands: Microphysical Properties, Emission Factors, and Implications for Direct Radiative Forcing. *Atmos. Chem. Phys.* 16 (5): 3033–40. doi.org/10.5194/acp-16-3033-2016.

Chakrabarty, R. K., H. Moosmüller, L. W. A. Chen, K. Lewis, W. P. Arnott, C. Mazzoleni, M. K. Dubey, C. E. Wold, W. M. Hao, and S. M. Kreidenweis. 2010. Brown Carbon in Tar Balls from Smoldering Biomass Combustion. *Atmos. Chem. Phys.* 10 (13): 6363–70. doi.org/10.5194/acp-10-6363-2010.

Chen, W. N., Y. C. Chen, C. Y. Kuo, C. H. Chou, C. H. Cheng, C. C. Huang, S. Y. Chang, et al. 2014. The Real-Time Method of Assessing the Contribution of Individual Sources on Visibility Degradation in Taichung. *Sci Total Environ.* 497–498 (110): 219–28. doi.org/10.1016/j.scitotenv.2014.07.120.

Chen, Y., and T. C. Bond. 2010. Light Absorption by Organic Carbon from Wood Combustion. *Atmos. Chem. Phys.* 9 (2001): 20471–513. doi.org/10.5194/acpd-9-20471-2009.

Cheng, Y., K. B. He, F. K. Duan, M. Zheng, Y. L. Ma, J. H. Tan, and Z. Y. Du. 2010. Improved Measurement of Carbonaceous Aerosol: Evaluation of the Sampling Artifacts and Inter-Comparison of the Thermal-Optical Analysis Methods. *Atmos. Chem. Phys.* 10 (17): 8533–48. doi.org/10.5194/acp-10-8533-2010.

Chow, J. C., J. G. Watson, L. W. A. Chen, W. P. Arnott, H. Moosmüller, and K. Fung. 2004. Equivalence of Elemental Carbon by Thermal/Optical Reflectance and Transmittance with Different Temperature Protocols. *Environ. Sci. Technol.* 38 (16): 4414–22. doi.org/10.1021/es034936u.

Chow, J. C., J. G. Watson, L. W. A. Chen, M. C. O. Chang, N. F. Robinson, D. Trimble, and S. Kohl. 2007. The IMPROVE_A Temperature Protocol for Thermal/Optical Carbon Analysis: Maintaining Consistency with a Long-Term Database. *J. Air & Waste Manage. Assoc.* 57 (9): 1014–23. doi.org/10.3155/1047-3289.57.9.1014.

Chow, J. C., J. G. Watson, D. Crow, D. H. Lowenthal, and T. Merrifield. 2001. Comparison of IMPROVE and NIOSH Carbon Measurements. *Aerosol Science and Technology* 34 (1): 23–34. doi.org/10.1080/02786820119073.

Chow, J. C., J. G. Watson, D. H. Lowenthal, L. Antony, N. Motallebi, J. C. Chow, J. G. Watson, et al. 2010. Black and Organic Carbon Emission Inventories : Review and Application to California Black and Organic Carbon Emission Inventories : Review and Application to California. *J. Air & Waste Manage. Assoc.* 60 (4): 497–507. doi.org/doi.org/10.3155/1047-

3289.60.4.497.

Claeys, M., R. Vermeylen, F. Yasmeen, Y. Gómez-González, X. Chi, W. Maenhaut, T. Mészáros, and I. Salma. 2012. Chemical Characterisation of Humic-like Substances from Urban, Rural and Tropical Biomass Burning Environments Using Liquid Chromatography with UV/Vis Photodiode Array Detection and Electrospray Ionisation Mass Spectrometry. Environmental Chemistry 9 (3): 273–84. doi.org/10.1071/EN11163.

Cross, E. S., J. G. Slowik, P. Davidovits, J. D. Allan, D. R. Worsnop, J. T. Jayne, D. K. Lewis, M. Canagaratna, and T. B. Onasch. 2007. Laboratory and Ambient Particle Density Determinations Using Light Scattering in Conjunction with Aerosol Mass Spectrometry. *Aerosol Science and Technology* 41 (4): 343–59. doi.org/10.1080/02786820701199736.

Du, Z., K. He, Y. Cheng, F. Duan, Y. Ma, J. Liu, X. Zhang, M. Zheng, and R. Weber. 2014a. A Yearlong Study of Water-Soluble Organic Carbon in Beijing I: Sources and Its Primary vs. Secondary Nature. *Atmospheric Environment* 92: 514–21. doi.org/10.1016/j.atmosenv.2014.04.060.

Du, Z., K. He, Y. Cheng, F. Duan, Y. Ma, J. Liu, X. Zhang, M. Zheng, and R. Weber. 2014b. A Yearlong Study of Water-Soluble Organic Carbon in Beijing II: Light Absorption Properties. *Atmospheric Environment* 89: 235–41. doi.org/10.1016/j.atmosenv.2014.02.022.

Fischer, D. Al, and G. D. Smith. 2018. A Portable, Four-Wavelength, Single-Cell Photoacoustic Spectrometer for Ambient Aerosol Absorption. *Aerosol Science and Technology* 52 (4): 393–406. doi.org/10.1080/02786826.2017.1413231.

Gao, S., J. D. Surratt, E. M. Knipping, E. S. Edgerton, M. Shahgholi, and J. H. Seinfeld. 2006. Characterization of Polar Organic Components in Fine Aerosols in the Southeastern United States: Identity, Origin, and Evolution. *J. Geophys. Res.* 111 (14): D14314. doi.org/10.1029/2005JD006601.

Hoffer, A., A. Tóth, I. NyirÅ'-Kósa, M. Pósfai, and A. Gelencsér. 2016. Light Absorption Properties of Laboratory-Generated Tar Ball Particles. *Atmos. Chem. Phys.* 16 (1): 239–46. doi.org/10.5194/acp-16-239-2016.

Hoffer, A., Á. Tóth, M. Pósfai, C. E. Chung, and A. Gelencsér. 2017. Brown Carbon Absorption in the Red and Near-Infrared Spectral Region. *Atmos. Chem. Phys* 10 (6): 2353–59. doi.org/10.5194/amt-10-2353-2017.

Hong, L., G. Liu, L. Zhou, J. Li, H. Xu, and D. Wu. 2017. Emission of Organic Carbon, Elemental Carbon and Water-Soluble Ions from Crop Straw Burning under Flaming and Smoldering Conditions. *Particuology* 31: 181–90. doi.org/10.1016/j.partic.2016.09.002.

Jacobson, M. Z. 2001. Strong Radiative Heating Due to the Mixing State of Black Carbon in Atmospheric Aerosols. *Nature* 409 (6821): 695–97. doi.org/10.1038/35055518.

Jeong, C. H., P. K. Hopke, E. Kim, and D. W. Lee. 2004. The Comparison between Thermal-Optical Transmittance Elemental Carbon and Aethalometer Black Carbon Measured at Multiple Monitoring Sites. *Atmospheric Environment* 38 (31): 5193–5204. doi.org/10.1016/j.atmosenv.2004.02.065.

Johansson, K. O., M. P. Head-Gordon, P. E. Schrader, K. R. Wilson, and H. A. Michelsen. 2018.

Resonance-Stabilized Hydrocarbon-Radical Chain Reactions May Explain Soot Inception and Growth. *Science* 361 (September): 997–1000. doi.org/10.1126/science.aat3417.

Karanasiou, A., M. C. Minguillón, M. Viana, A. Alastuey, J.-P. Putaud, W. Maenhaut, P. Panteliadis, G. Močnik, O. Favez, and T. A. J. Kuhlbusch. 2015. Thermal-Optical Analysis for the Measurement of Elemental Carbon (EC) and Organic Carbon (OC) in Ambient Air a Literature Review. *Atmos. Meas. Tech.* 8 (9): 9649–9712. doi.org/10.5194/amtd-8-9649-2015.

Kirchstetter, T. W., C. E. Corrigan, and T. Novakov. 2001. Laboratory and Field Investigation of the Adsorption of Gaseous Organic Compounds onto Quartz Filters. *Atmospheric Environment* 35 (9): 1663–71. doi.org/10.1016/S1352-2310(00)00448-9.

Kirchstetter, T. W., T. Novakov, and P. V. Hobbs. 2004. Evidence That the Spectral Dependence of Light Absorption by Aerosols Is Affected by Organic Carbon. *J. Geophys. Res.* 109 (21): D21208. doi.org/10.1029/2004JD004999.

Kirchstetter, T. W., and T. L. Thatcher. 2012. Contribution of Organic Carbon to Wood Smoke Particulate Matter Absorption of Solar Radiation. *Atmos. Chem. Phys.* 12 (14): 6067–72. doi.org/10.5194/acp-12-6067-2012.

Lack, D. A., and C. D. Cappa. 2010. Impact of Brown and Clear Carbon on Light Absorption Enhancement, Single Scatter Albedo and Absorption Wavelength Dependence of Black Carbon. *Atmos. Chem. Phys.* 10 (9): 4207–20. doi.org/10.5194/acp-10-4207-2010.

Lack, D. A., and J. M. Langridge. 2013. On the Attribution of Black and Brown Carbon Light

Absorption Using the Ångström Exponent. *Atmos. Chem. Phys.* 13 (20): 10535–43. doi.org/10.5194/acp-13-10535-2013.

Lambe, A. T., C. D. Cappa, P. Massoli, T. B. Onasch, S. D. Forestieri, A. T. Martin, M. J. Cummings, et al. 2013. Relationship between Oxidation Level and Optical Properties of Secondary Organic Aerosol. *Environ. Sci. Technol.* 47 (12): 6349–57. doi.org/10.1021/es401043j.

Laskin, A., J. Laskin, and S. A. Nizkorodov. 2015. Chemistry of Atmospheric Brown Carbon. *Chemical Reviews* 115 (10): 4335–82. doi.org/10.1021/cr5006167.

Lautenberger, C. W., J. L. De Ris, N. A. Dembsey, J. R. Barnett, and H. R. Baum. 2005. A Simplified Model for Soot Formation and Oxidation in CFD Simulation of Non-Premixed Hydrocarbon Flames. *Fire Safety Journal* 40 (2): 141–76. doi.org/10.1016/j.firesaf.2004.10.002.

Li, W., Z. Liu, Z. Wang, and H. Dou. 2015. Experimental and Theoretical Analysis of Effects of Atomic, Diatomic and Polyatomic Inert Gases in Air and EGR on Mixture Properties, Combustion, Thermal Efficiency and NOx Emissions of a Pilot-Ignited NG Engine. *Energy Conversion and Management* 105: 1082–95. doi.org/10.1016/j.enconman.2015.08.052.

Li, X., Y. Chen, and T. C. Bond. 2016. Light Absorption of Organic Aerosol from Pyrolysis of Corn Stalk. *Atmospheric Environment* 144: 249–56. doi.org/10.1016/j.atmosenv.2016.09.006.

Iinuma, Y., O. Böge, and H. Herrmann. 2010. Methyl-Nitrocatechols: Atmospheric Tracer

Compounds for Biomass Burning Secondary Organic Aerosols. *Environ. Sci. Technol.* 44 (22): 8453–59. doi.org/10.1021/es102938a.

IPCC. 2013. Climate Change 2013: The Physical Science Basis. Contri- Bution OfWorking Group I to the Fifth Assessment Report of the Intergovernmental Panel on Climate Change, Chapter 8: Anthropogeni. Edited by V. Bex and P.M. Midgley (eds.) Stocker, T.F., D. Qin, G.-K. Plattner, M. Tignor, S.K. Allen, J. Boschung, A. Nauels, Y. Xia. *Climate Change 2013: The Physical Science Basis. Contribution of Working Group I to the Fifth Assessment Report of the Intergovernmental Panel on Climate Change*. Cambridge, United Kingdom and New York, NY, USA. doi.org/10.1017/ CBO9781107415324.018.

Lin, P., P. K. Aiona, Y. Li, M. Shiraiwa, J. Laskin, S. A. Nizkorodov, and A. Laskin. 2016. Molecular Characterization of Brown Carbon in Biomass Burning Aerosol Particles. *Environ. Sci. Technol.* 50 (21): 11815–24. doi.org/10.1021/acs.est.6b03024.

Ma, J., X. Li, P. Gu, T. R. Dallmann, A. A. Presto, and N. M. Donahue. 2016. Estimating Ambient Particulate Organic Carbon Concentrations and Partitioning Using Thermal Optical Measurements and the Volatility Basis Set. *Aerosol Science and Technology* 50 (6): 638–51. doi.org/10.1080/02786826.2016.1158778.

Malloy, Q. G. J., S. Nakao, L. Qi, R. Austin, C. Stothers, H. Hagino, and D. R. Cocker. 2009. Real-Time Aerosol Density Determination Utilizing a Modified Scanning Mobility Particle Sizer Aerosol Particle Mass Analyzer System. *Aerosol Science and Technology* 43 (7): 673–78. doi.org/10.1080/02786820902832960.

Martinsson, J., A. C. Eriksson, I. E. Nielsen, V. B. Malmborg, E. Ahlberg, C. Andersen, R.

Lindgren, et al. 2015. Impacts of Combustion Conditions and Photochemical Processing on the Light Absorption of Biomass Combustion Aerosol. *Environ. Sci. Technol.* 49 (24): 14663–71. doi.org/10.1021/acs.est.5b03205.

Michael R. Olson, Mercedes Victoria Garcia, Michael A. Robinson, Paul Van Rooy, Mark A. Dietenberger, Michael Bergin, and J. J. S. 2015. Investigation of Black and Brown Carbon Multiple-Wavelength- Dependent Light Absorption from Biomass and Fossil Fuel Combustion Source Emissions. *J. Geophys. Res. Atmos* 120: 6682–97. doi.org/10.1002/2014JD022970.Received.

Michelsen, H. A. 2017. Probing Soot Formation, Chemical and Physical Evolution, and Oxidation: A Review of in Situ Diagnostic Techniques and Needs. *Proceedings of the Combustion Institute* 36 (1): 717–35. doi.org/10.1016/j.proci.2016.08.027.

Moosmüller, H., R. K. Chakrabarty, and W. P. Arnott. 2009. Aerosol Light Absorption and Its Measurement: A Review. *Journal of Quantitative Spectroscopy and Radiative Transfer* 110 (11): 844–78. doi.org/10.1016/j.jqsrt.2009.02.035.

Moosmüller, H., R. K. Chakrabarty, K. M. Ehlers, and W. P. Arnott. 2011. Absorption Ångström Coefficient, Brown Carbon, and Aerosols: Basic Concepts, Bulk Matter, and Spherical Particles. *Atmos. Chem. Phys.* 11 (3): 1217–25. doi.org/10.5194/acp-11-1217-2011.

Petzold, A., J. A. Ogren, M. Fiebig, P. Laj, S. M. Li, U. Baltensperger, T. Holzer-Popp, et al. 2013. Recommendations for Reporting Black Carbon Measurements. *Atmos. Chem. Phys.* 13 (16): 8365–79. doi.org/10.5194/acp-13-8365-2013.

Phillips, S. M., and G. D. Smith. 2014. Light Absorption by Charge Transfer Complexes in Brown Carbon Aerosols. Environ. Sci. Technol. Lett. 1 (10): 382–86. doi.org/10.1021/ez500263j.

Phillips, S. M., and G. D. Smith. 2015. Further Evidence for Charge Transfer Complexes in Brown Carbon Aerosols from Excitation-Emission Matrix Fluorescence Spectroscopy. J. Phys. Chem. 119 (19): 4545–51. doi.org/10.1021/jp510709e.

Pokhrel, R. P., N. L. Wagner, J. M. Langridge, D. A. Lack, T. Jayarathne, E. A. Stone, C. E. Stockwell, R. J. Yokelson, and S. M. Murphy. 2016. Parameterization of Single-Scattering Albedo (SSA) and Absorption Ångström Exponent (AAE) with EC/OC for Aerosol Emissions from Biomass Burning. *Atmos. Chem. Phys.* 16 (15): 9549–61. doi.org/10.5194/acp-16-9549-2016.

Poudel, S., M. Fiddler, D. Smith, K. Flurchick, and S. Bililign. 2017. Optical Properties of Biomass Burning Aerosols: Comparison of Experimental Measurements and T-Matrix Calculations. *Atmosphere* 8 (11): 228. doi.org/10.3390/atmos8110228.

Qiu, C., A. F. Khalizov, and R. Zhang. 2012. Soot Aging from OH-Initiated Oxidation of Toluene. *Environ. Sci. Technol.* 46 (17): 9464–72. doi.org/10.1021/es301883y.

Rezgui, Y., and M. Guemini. 2014. Benzene Combustion: A Detailed Chemical Kinetic Modeling in Laminar Flames Conditions. Kinetics and Catalysis 55 (3): 278–86. doi.org/10.1134/S0023158414030124

Rissler, J., E. Z. Nordin, A. C. Eriksson, P. T. Nilsson, M. Frosch, M. K. Sporre, A. Wierzbicka, et al. 2014. Effective Density and Mixing State of Aerosol Particles in a Near-Traffic Urban

Environment. *Environ. Sci. Technol.* 48 (11): 6300–6308. doi.org/10.1021/es5000353.

Rizzo, L. V., P. Artaxo, T. Müller, A. Wiedensohler, M. Paixão, G. G. Cirino, A. Arana, et al. 2013. Long Term Measurements of Aerosol Optical Properties at a Primary Forest Site in Amazonia. *Atmos. Chem. Phys.* 13 (5): 2391–2413. doi.org/10.5194/acp-13-2391-2013.

Rizzo, L. V., A. L. Correia, P. Artaxo, A. S. Procápio, and M. O. Andreae. 2011. Spectral Dependence of Aerosol Light Absorption over \newline the Amazon Basin. *Atmos. Chem. Phys.* 11 (17): 8899–8912. doi.org/10.5194/acp-11-8899-2011.

Roden, C. A., T. C. Bond, S. Conway, and A. B. Osorto Pinel. 2006. Emission Factors and Real-Time Optical Properties of Particles Emitted from Traditional Wood Burning Cookstoves. *Environ. Sci. Technol.* 40 (21): 6750–57. doi.org/10.1021/es052080i.

Salako, G. O., P. K. Hopke, D. D. Cohen, B. A. Begum, S. K. Biswas, G. G. Pandit, Y. S. Chung, et al. 2012. Exploring the Variation between EC and BC in a Variety of Locations. *Aerosol and Air Quality Research* 12 (1): 1–7. doi.org/10.4209/aaqr.2011.09.0150.

Saleh, R., Z. Cheng, and K. Atwi. 2018. The Brown–Black Continuum of Light-Absorbing Combustion Aerosols. *Environ. Sci. Technol. Lett.* 5 (8): 508–513. doi.org/10.1021/acs.estlett.8b00305.

Saleh, R., C. J. Hennigan, G. R. McMeeking, W. K. Chuang, E. S. Robinson, H. Coe, N. M. Donahue, and A. L. Robinson. 2013. Absorptivity of Brown Carbon in Fresh and Photo-Chemically Aged Biomass-Burning Emissions. *Atmos. Chem. Phys.* 13 (15): 7683–93. doi.org/10.5194/acp-13-7683-2013.

Saleh, R., E. S. Robinson, D. S. Tkacik, A. T. Ahern, S. Liu, A. C. Aiken, R. C. Sullivan, et al. 2014. Brownness of Organics in Aerosols from Biomass Burning Linked to Their Black Carbon Content. *Nature Geoscience* 7 (9): 647–50. doi.org/10.1038/ngeo2220.

Sarangi, B., S. G. Aggarwal, D. Sinha, and P. K. Gupta. 2016. Aerosol Effective Density Measurement Using Scanning Mobility Particle Sizer and Quartz Crystal Microbalance with the Estimation of Involved Uncertainty. *Atmos. Meas. Tech.* 9 (3): 859–75. doi.org/10.5194/amt-9-859-2016.

Schmid, O., D. Chand, E. Karg, P. Guyon, G. P. Frank, E. Swietlicki, and M. O. Andreae. 2009. Derivation of the Density and Refractive Index of Organic Matter and Elemental Carbon from Closure between Physical and Chemical Aerosol Properties Derivation of the Density and Refractive Index of Organic Matter and Elemental Carbon from Closure Between. *Environ. Sci. Technol.* 43 (4): 1166–72.

Schnitzler, E. G., A. Dutt, A. M. Charbonneau, J. S. Olfert, and W. Jäger. 2014. Soot Aggregate Restructuring Due to Coatings of Secondary Organic Aerosol Derived from Aromatic Precursors. *Environ. Sci. Technol.* 48 (24): 14309–16. doi.org/10.1021/es503699b.

Selimovic, V., R. J. Yokelson, C. Warneke, J. M. Roberts, J. A. de Gouw, and D. W. T. Griffith. 2018. Aerosol Optical Properties and Trace Gas Emissions from Laboratory-Simulated Western US Wildfires. *Atmos. Chem. Phys.* 18 (4): 2929–48.

Shen, G., S. Tao, S. Wei, Y. Zhang, R. Wang, B. Wang, W. Li, et al. 2012. Reductions in Emissions of Carbonaceous Particulate Matter and Polycyclic Aromatic Hydrocarbons from Combustion of Biomass Pellets in Comparison with Raw Fuel Burning. *Environ. Sci.*

*Technol.* 46 (11): 6409–16. doi.org/10.1021/es300369d.

Slowik, J. G., E. S. Cross, J. H. Han, J. Kolucki, P. Davidovits, L. R. Williams, T. B. Onasch, J. T. Jayne, C. E. Kolb, and D. R. Worsnop. 2007. Measurements of Morphology Changes of Fractal Soot Particles Using Coating and Denuding Experiments: Implications for Optical Absorption and Atmospheric Lifetime. *Aerosol Science and Technology* 41 (8): 734–50. doi.org/10.1080/02786820701432632.

Slowik, J. G., K. Stainken, P. Davidovits, L. R. Williams, J. T. Jayne, C. E. Kolb, D. R. Worsnop, Y. Rudich, P. F. DeCarlo, and J. L. Jimenez. 2004. Particle Morphology and Density Characterization by Combined Mobility and Aerodynamic Diameter Measurements. Part 2: Application to Combustion-Generated Soot Aerosols as a Function of Fuel Equivalence Ratio. *Aerosol Science and Technology* 38 (12): 1206–22. doi.org/10.1080/027868290903916.

Soewono, A., and S. N. Rogak. 2013. Morphology and Optical Properties of Numerically Simulated Soot Aggregates. *Aerosol Science and Technology* 47 (3): 267–74. doi.org/10.1080/02786826.2012.749972.

Sorensen, C. M. 2001. Light Scattering by Fractal Aggregates: A Review. *Aerosol Science and Technology* 35 (2): 648–687. doi.org/doi.org/10.1080/02786820117868.

Stockwell, C. E., T. Jayarathne, M. A. Cochrane, K. C. Ryan, E. I. Putra, B. H. Saharjo, A. D. Nurhayati, et al. 2016. Field Measurements of Trace Gases and Aerosols Emitted by Peat Fires in Central Kalimantan, Indonesia, during the 2015 El Niño. *Atmos. Chem. Phys.* 16 (18): 11711–32. doi.org/10.5194/acp-16-11711-2016.

Subramanian, R., A. Y. Khlystov, J. C. Cabada, and A. L. Robinson. 2004. Positive and Negative Artifacts in Particulate Organic Carbon Measurements with Denuded and Undenuded Sampler Configurations Special Issue of Aerosol Science and Technology on Findings from the Fine Particulate Matter Supersites Program. *Aerosol Science and Technology* 38 (Si): 27–48. doi.org/10.1080/02786820390229354.

Sumlin, B. J., C. Oxford, B. Seo, R. Pattison, B. J. Williams, and R. K. Chakrabarty. 2018. Density and Homogeneous Internal Composition of Primary Brown Carbon Aerosol. *Environ. Sci. Technol.*, no. 1: acs.est.8b00093. doi.org/10.1021/acs.est.8b00093.

Sun, J., Z. Shen, L. Zhang, Q. Zhang, Y. Lei, J. Cao, Y. Huang, et al. 2018. Impact of Primary and Secondary Air Supply Intensity in Stove on Emissions of Size-Segregated Particulate Matter and Carbonaceous Aerosols from Apple Tree Wood Burning. *Atmospheric Research* 202 (October 2017): 33–39. doi.org/10.1016/j.atmosres.2017.11.010.

Sun, J., G. Zhi, R. Hitzenberger, Y. Chen, C. Tian, Y. Zhang, Y. Feng, et al. 2017. Emission Factors and Light Absorption Properties of Brown Carbon from Household Coal Combustion in China. *Atmos. Chem. Phys.* 17 (7): 4769–80. doi.org/10.5194/acp-17-4769-2017.

Turns, S. R. 2000. *An Introduction to Combustion: Concepts and Applications*. Second edi. New York: The McGraw-Hill Companies, Inc.

Turpin, B. J., J. J. Huntzicker, and S. V. Hering. 1994. Investigation of Organic Aerosol Sampling Artifacts in the Los Angeles Basin. *Atmospheric Environment* 28 (19): 3061–71. doi.org/10.1016/1352-2310(94)00133-6.

Turpin, B. J., P. Saxena, and E. Andrews. 2000. Measuring and Simulating Particulate Organics in the Atmosphere: Problems and Prospects. *Atmospheric Environment* 34 (18): 2983–3013. doi.org/10.1016/S1352-2310(99)00501-4.

Updyke, K. M., T. B. Nguyen, and S. A. Nizkorodov. 2012. Formation of Brown Carbon via Reactions of Ammonia with Secondary Organic Aerosols from Biogenic and Anthropogenic Precursors. *Atmospheric Environment* 63: 22–31. doi.org/10.1016/j.atmosenv.2012.09.012.

Utry, N., T. Ajtai, ágnes Filep, M. Dániel Pintér, A. Hoffer, Z. Bozoki, and G. Szabó. 2013. Mass Specific Optical Absorption Coefficient of HULIS Aerosol Measured by a Four-Wavelength Photoacoustic Spectrometer at NIR, VIS and UV Wavelengths. *Atmospheric Environment* 69: 321–24. doi.org/10.1016/j.atmosenv.2013.01.003.

Vandaele, A. C. 2002. High-Resolution Fourier Transform Measurement of the NO 2 Visible and near-Infrared Absorption Cross Sections: Temperature and Pressure Effects. *J. Geophys. Res.* 107 (D18): 4348. doi.org/10.1029/2001JD000971.

Vicente, E. D., M. A. Duarte, A. I. Calvo, T. F. Nunes, L. A. C. Tarelho, D. Custódio, C. Colombi, V. Gianelle, A. Sanchez de la Campa, and C. A. Alves. 2015. Influence of Operating Conditions on Chemical Composition of Particulate Matter Emissions from Residential Combustion. *Atmospheric Research* 166: 92–100. doi.org/10.1016/j.atmosres.2015.06.016.

Wagnon, S. W., and M. S. Wooldridge. 2014. Effects of Buffer Gas Composition on Autoignition. *Combustion and Flame* 161 (4): 898–907. doi.org/10.1016/j.combustflame.2013.09.022.

Watson, J. G., J. C. Chow, and L. A. Chen. 2005. *Summary of Organic and Elemental Carbon /*

*Black Carbon Analysis Methods and Intercomparisons*. *Aerosol and Air Quality Research*. Vol. 5. doi.org/10.4209/aaqr.2005.06.0006.

Willingham, C. B., W. J. Taylor, J. M. Pignocco, and F. D. Rossini. 1945. Vapor Pressures and Boiling Points of Some Paraffin, Alkylcyclopentane, Alkylcyclohexane, and Alkylbenzene Hydrocarbons. *Journal of Research of the National Bureau of Standards* 35 (3): 219. doi.org/10.6028/jres.035.009.

Xie, M., M. D. Hays, and A. L. Holder. 2017. Light-Absorbing Organic Carbon from Prescribed and Laboratory Biomass Burning and Gasoline Vehicle Emissions. *Scientific Reports* 7 (1): 1–9. doi.org/10.1038/s41598-017-06981-8.

Yang, M., S. G. Howell, J. Zhuang, and B. J. Huebert. 2009. Attribution of Aerosol Light Absorption to Black Carbon, Brown Carbon, and Dust in China - Interpretations of Atmospheric Measurements during EAST-AIRE. *Atmos. Chem. Phys.* 9 (6): 2035–50. doi.org/10.5194/acp-9-2035-2009.

Zhang, X., Y. H. Lin, J. D. Surratt, and R. J. Weber. 2013. Sources, Composition and Absorption Ångström Exponent of Light-Absorbing Organic Components in Aerosol Extracts from the Los Angeles Basin. *Environ. Sci. Technol.* 47 (8): 3685–93. doi.org/10.1021/es305047b.

Zhang, Y., Q. Zhang, Y. Cheng, H. Su, S. Kecorius, Z. Wang, Z. Wu, et al. 2016. Measuring the Morphology and Density of Internally Mixed Black Carbon with SP2 and VTDMA: New Insight into the Absorption Enhancement of Black Carbon in the Atmosphere. *Atmos. Meas. Tech.* 9 (4): 1833–43. doi.org/10.5194/amt-9-1833-2016.

# CHAPTER 3

# EVALUTION OF THE LIGHT-ABSORTPION PROPERTIES OF COMBUSTION BROWN CARBON AEROSOLS FOLLWING REACTION WITH NITRATE RADICALS [2]

[2] Cheng, Z., K. M. Atwi, Z. Yu, A. Avery, E. C. Fortner, L. Williams, F. Majluf, J. E. Krechmer, A. T. Lambe, and R. Saleh. Aerosol Science and Technology, DOI: 10.1080/02786826.2020.1726867
Reprinted here with permission of the publisher

**Abstract**

Polycyclic aromatic hydrocarbons (PAHs) are important constituents of brown carbon (BrC) that are subject to atmospheric processing by gas-phase oxidants such as the hydroxyl radical (OH) and the nitrate radical ($NO_3$). While OH oxidation of BrC has been investigated extensively, studies of $NO_3$ oxidation are limited. Here, we generated BrC from the combustion of toluene containing a complex mixture of light-absorbing PAHs and investigated changes in their chemical composition and light-absorption properties following exposure to $NO_3$ in an oxidation flow reactor. Three types of BrC were studied, with varying light-absorption properties that were classified in terms of the imaginary part of the refractive index ($k$) as: light BrC ($k$ at 532 nm, $k_{532}$ = 0.008), medium BrC ($k_{532}$ = 0.026), and dark BrC ($k_{532}$ = 0.091). Exposure to $NO_3$ led to ~30% increase in $k_{532}$ of the light and medium BrC and ~5% decrease in $k_{532}$ of the dark BrC. This discrepancy is attributed to two competing effects: 1) addition of chromophoric functional groups by NO3-induced heterogeneous oxidation and 2) condensation of gas-phase PAH+$NO_3$ oxidation products that were less-absorbing than the particulate PAHs. Analysis of the aerosol chemical evolution revealed that effect (2) was more important in the dark BrC experiments. We performed optical calculations to isolate effect (1) and showed that heterogeneous oxidation led to ~50% increase in $k_{532}$ for all the BrC types. These results indicate that $NO_3$-induced heterogeneous oxidation darkens some types of atmospheric BrC, which can counterbalance bleaching effects induced by OH oxidation.

## 3.1. Introduction

Brown carbon (BrC), also known as light-absorbing organic aerosol (OA), plays a vital role alongside black carbon (BC) in the absorption of solar radiation by carbonaceous aerosols. This has been confirmed by numerous laboratory experiments (e.g., Saleh et al. 2014; Adler et al. 2019; Olson et al. 2015), field observations (e.g., Lack et al. 2012; Zhang et al. 2017), and remote-sensing observations (e.g., Wang et al. 2016; Jethva and Torres 2011; Wang et al. 2013). Consequently, the radiative effect of light absorption by BrC has been the focus of several global-climate calculations (e.g., Saleh et al. 2015; Jo et al. 2016; Hammer et al. 2016; Wang et al. 2014; Brown et al. 2018; Feng et al. 2013; Wang et al. 2018). These modeling studies have revealed a potentially important, yet highly uncertain radiative effect associated with BrC light absorption, with global-mean values ranging between +0.03 W $m^{-2}$ and +0.57 W $m^{-2}$. This large variability is in part a manifestation of the limited understanding of the chemical nature, formation pathways, and atmospheric processing of BrC, which hinders explicit representation of the wide range of experimentally derived BrC light-absorption properties within a climate-modeling framework.

While BrC is typically associated with biomass-combustion emissions, it has also been observed in the emissions of fossil-fuel combustion as well as in secondary organic aerosol (SOA) formed by the oxidation of biogenic and anthropogenic precursors (Laskin, Laskin, and Nizkorodov 2015; Moise, Flores, and Rudich 2015). The light-absorption properties of BrC are usually quantified using the wavelength-dependent imaginary part of the refractive index ($k$) or the mass absorption cross section (MAC). The values of $k$ at mid-visible wavelengths reported for BrC range over 3 orders of magnitude ($10^{-4}$ to $10^{-1}$) (Laskin, Laskin, and Nizkorodov 2015). BrC exhibits an increase in absorption with decreasing wavelength within the visible spectrum, which can be represented

using a power-law functional dependence on wavelength. The values of wavelength dependence ($w$) of $k$ (i.e., the exponent of the power-law) vary from ~1 to 10. For reference, the corresponding mid-visible MAC ($m^2\ g^{-1}$) values can be roughly approximated by multiplying the mid-visible $k$ by 10. Also, the wavelength dependence of MAC, the absorption Ångström exponent (AAE), can be approximated as $w + 1$ for particles much smaller than the wavelength.

In terms of chemical composition, atmospheric BrC has been often associated with the broad family of humic-like substances (HULIS) (Kwon et al. 2018; Claeys et al. 2012; Utry et al. 2013; Wang et al. 2019). This is rooted in a study by Mukai and Ambe (1986) who identified brown airborne particles originating from biomass burning and found that their chemical signatures were similar to humic acids. Another broad term, tar balls, was introduced by Posfai et al. (2004) and has been used to designate a class of BrC emitted from biomass combustion (Adachi et al. 2018; Sedlacek III et al. 2018; Hoffer et al. 2016; Tóth et al. 2014). These two classifications are not necessarily incompatible. BrC absorption in biomass-combustion emissions have been linked to charge transfer complexes (Phillips and Smith 2014) as well as aromatic species, including polycyclic aromatic hydrocarbons (PAHs) ( Li, He, Schade et al. 2019; Adler et al. 2019) and oxygenated and nitrated aromatics ( Li, He, Schade et al. 2019; Lin et al. 2016; Liu et al. 2017; Desyaterik et al. 2013). Such chromophores have been identified both in HULIS (Claeys et al. 2012; Wang et al. 2019) as well as tar balls ( Li, He, Hettiyadura et al. 2019; Li, He, Schade et al. 2019).

Despite the advances in identifying the chemical species that constitute BrC, a comprehensive picture of the landscape of BrC chemical structure is still lacking (Laskin, Laskin, and Nizkorodov 2015). Perhaps even more lacking is the understanding of the evolution of BrC upon chemical

processing in the atmosphere, which has been the focus of numerous recent studies. Both laboratory studies (Browne et al. 2019; Sumlin et al. 2017; Zhao et al. 2015; Wong, Nenes, and Weber 2017; Wong et al. 2019) and field measurements (Satish et al. 2017; Dasari et al. 2019; Forrister et al. 2015; Wong et al. 2019) have observed that photo-oxidation led to a reduction in BrC light absorption. This bleaching effect could be attributed to either dark or photo-initiated destruction of chromophores through OH oxidation. On the other hand, the presence of $NO_x$ has been observed to enhance the BrC light absorption ( Li, He, Hettiyadura et al. 2019; Li, He, Schade et al. 2019; Wang et al. 2019) or slow down the OH-induced bleaching effect (Zhong and Jang 2014; Nakayama et al. 2013). Another important, yet understudied, atmospheric reaction that can potentially contribute to the dynamic behavior of BrC light absorption is the nighttime reaction of PAHs with $NO_3$ radicals (Keyte et al. 2013;). The large reaction rate coefficients (Mak et al. 2007) and rapid uptake of $NO_3$ on surfaces (Knopf, Forrester, and Slade 2011) suggest that $NO_3$ could induce heterogeneous oxidation of condensed-phase PAHs, leading to the formation of nitrogen-containing PAH derivatives, including nitro-PAHs. Studies of heterogeneous oxidation of single-compound PAHs (e.g., anthracene, pyrene, and benzo[a]pyrene) with $NO_2$/$NO_3$/$N_2O_5$ indicated that these reactions resulted in enhanced UV-visible absorption of the oxidized PAHs relative to their parent molecules (Kwamena and Abbatt 2008; Lu et al. 2011).

As alluded to above, PAHs are major constituents of combustion BrC, especially the highly-absorptive fraction (Saleh et al. 2018; Li, He, Hettiyadura et al. 2019; Li, He, Schade et al. 2019; Adler et al. 2019). This is not surprising since PAHs have been identified as key species in the soot-formation process by numerous fundamental laboratory studies (Michelsen 2017) and have been known to constitute a substantial fraction of combustion emissions of fossil (Karavalakis et al. 2011) and biomass (Shen et al. 2012) fuels. We have recently shown that BrC produced from

the combustion of benzene and toluene has prominent PAH signatures and exhibits varying molecular sizes, volatilities, and light-absorbing properties that are dependent on combustion conditions such as temperature and relative amounts of fuel, oxygen, and nitrogen (Saleh et al. 2018). The light-absorption properties of these PAHs fall on a continuum that extends from weakly absorbing (light) BrC to strongly absorbing (dark) BrC, eventually approaching BC (Cheng et al. 2019). Here, we build on these findings to investigate the evolution of the light-absorption properties of complex PAH-containing BrC following oxidation by $NO_3$. We performed toluene-combustion experiments controlled at different combustion conditions to produce BrC with varying levels of darkness. For each combustion condition, we exposed the BrC to $NO_3$ in an oxidation flow reactor (OFR) and compared the light-absorption properties and chemical composition of the oxidation products to their parent molecules. Since PAHs and their derivatives are the dominant constituents of toluene-combustion BrC (Saleh et al. 2018), we use BrC and PAHs interchangeably throughout the paper in a manner that serves the discussion.

### 3.2. Methods

As shown in Figure 3.1, the experimental setup employed in this study has 4 major components: 1) A combustion system used to generate BrC with variable light-absorption properties; 2) $N_2O_5$ generation system; 3) oxidation flow reactor (OFR), where the BrC was aged with $NO_3$ produced from thermal decomposition of $N_2O_5$; and 4) a suite of instruments that enabled characterization of the chemical composition and light-absorption properties of the OFR effluent. Each of the components is described in the subsequent sections.

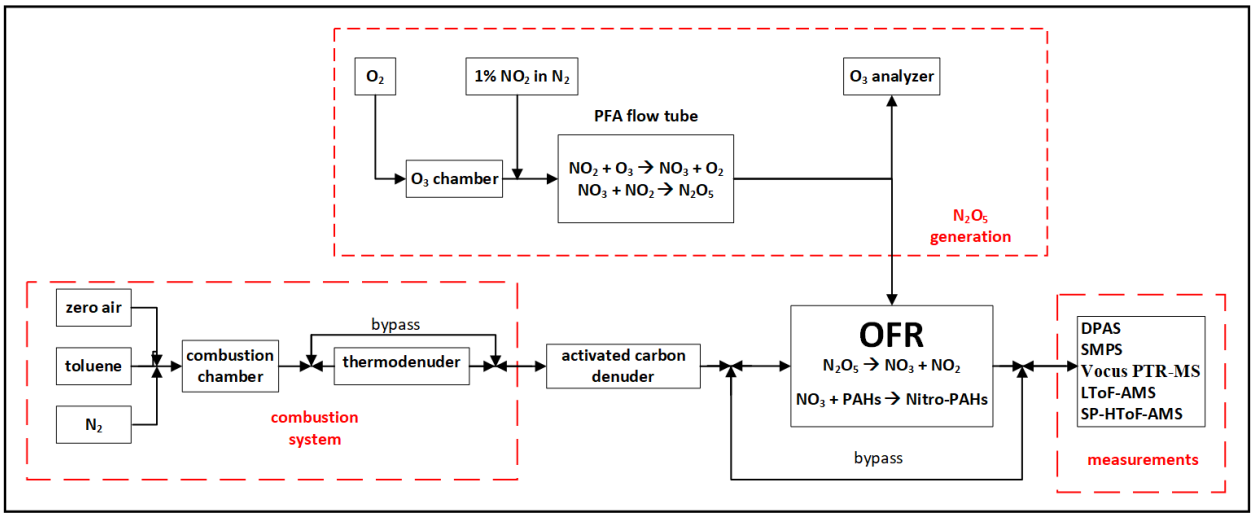


**Figure 3.1:** Schematic of the experimental setup for generating unoxidized and oxidized (with $NO_3$) BrC

### 3.2.1. Combustion system

A detailed description of the combustion system can be found in Cheng et al. (2019). Briefly, combustion of toluene was performed in a quartz combustion chamber controlled at 1050 ˚C. Toluene vapor was introduced into the combustion chamber by flowing nitrogen through a bubbler containing toluene. The flow of toluene-saturated nitrogen (0.14 - 0.17 LPM) was then mixed with flows of nitrogen (0.35 - 0.41 LPM) and zero air (0.23 - 0.24 LPM) before entering the combustion chamber. By controlling the relative flowrates of toluene, zero air, and nitrogen, we generated BrC with varying light-absorption properties. Specifically, decreasing the nitrogen flowrate produced larger-molecular size, more-absorbing (darker) BrC. Combustion conditions were fine-tuned using the observed light absorption properties (MAC and AAE) that were calculated in real-time based on measurements of particle size distributions and light absorption coefficients, as described in Section 3.2.3. In one experiment, we passed the combustion emissions through a thermodenuder controlled at 200 ˚C. By doing so, we relied on the established association between volatility,

molecular size, and light-absorption properties (Saleh et al. 2018) to isolate the dark, large-molecular-size fraction of the BrC. In order to minimize contributions of gas-phase PAH + $NO_3$ oxidation products on the optical properties of the BrC (i.e., condensed-phase PAHs), an activated carbon denuder was placed in-line before the OFR to absorb gas-phase components of the combustion emissions.

### 3.2.2. $NO_3$ generation and oxidative aging of the BrC

As shown in Figure 3.1, separate flows containing $NO_2$ (1% in $N_2$ , Praxair) and $O_3$ were input to a perfluoro alkoxy (PFA) flow tube with 1 inch outer diameter and 60" length that was operated as a laminar flow reactor (LFR), where, upon mixing, $N_2O_5$ was generated in the gas phase from the reaction $NO_2 + O_3 \rightarrow NO_3 + O_2$ followed by the reaction $NO_3 + NO_2 \rightarrow N_2O_5$ (Lambe et al. 2020). In these experiments, the $NO_2$ in the $N_2$ flow rate was set between 0 and 15 $cm^3\ min^{-1}$, and $O_3$ was generated by passing 2 LPM of $O_2$ through an ozone chamber housing a mercury fluorescent lamp (GPH212T5VH, Light Sources, Inc.). The output of the LFR was mixed with the combustion emissions and ~12 LPM of dilution air prior to injection into an Aerodyne Potential Aerosol Mass oxidation flow reactor (OFR) (Lambe et al. 2011). The mean residence time in the OFR was approximately 70 sec. The $N_2O_5$ generated in the LFR thermally decomposed at room temperature inside the OFR to generate $NO_3$, which initiated oxidation of the PAHs (both in the condensed phase and vapor phase) introduced from the combustion system. The integrated $NO_3$ exposure, that is, the product of the $NO_3$ concentration and mean OFR residence time, was estimated based on results from a separate set of experiments as $5.2 \times 10^{13}$ molec $cm^{-3}$ sec, corresponding to an equivalent atmospheric aging time of approximately 2.4 nights assuming a

12-hour average ambient $NO_3$ mixing ratio of 20 ppt (Atkinson 1991) and negligible daytime $NO_3$ concentration. The calculations are shown in the SI.

### 3.2.3. Size distributions and light-absorption properties

The size distributions of the unoxidized and oxidized BrC particles were measured using a scanning mobility particle sizer (SMPS, TSI). As shown in Figure S3.1, the volume distributions of the particles were scanned from 10 nm to 400 nm, with mode diameters between 60 nm and 80 nm. We also integrated the SMPS volume distributions and calculated the total aerosol mass concentrations ($m_p$) using a density of 1.2 g $cm^{-3}$. The density was obtained in a previous experiment on similar aerosol emissions using the tandem differential mobility analyzer – aerosol particle mass analyzer (tandem DMA-APM) technique (Malloy et al. 2009).

We measured the absorption coefficients ($b_{abs}$, $Mm^{-1}$) at $\lambda$ = 473, 532, and 671 nm using a differential photoacoustic aerosol spectrometer (DPAS, Aerodyne Research Inc.) (Yu et al. 2019). The DPAS contains two photoacoustic cells, where one cell measures light absorption by the total aerosol and gaseous sample, and the other cell measures the light absorption by the gaseous sample only. Aerosol light absorption is calculated as the difference in light absorption measured by the two cells. The DPAS has a time resolution of 10 s and detection limits of 0.20 $Mm^{-1}$ at 671 nm, 0.22 $Mm^{-1}$ at 532 nm, and 0.90 $Mm^{-1}$ at 473nm (Yu et al. 2019). Following the procedure of Yu et al. (2019), we calibrated the DPAS absorption at the 3 wavelengths using synthetic pigment black particles (Cab-O-Jet 200 from Cabot Corp., Boston, MA, USA). Cab-O-Jet has spectroscopic and morphological properties similar to aged BC (MAC at 550 nm = 7.89 ± 0.25 $m^2$ $g^{-1}$ and AAE = 1.03 ± 0.09) (You et al. 2016). The calibration process involved size-selecting Cab-O-Jet particles of 300 nm electrical-mobility diameter using a differential mobility analyzer (DMA, TSI) at

different concentrations and using linear regression to obtain the calibration coefficient at each wavelength as the slope of the DPAS microphone signal versus concentration.

Using the $b_{abs}$ values from the DPAS and $m_p$ values from the SMPS, we calculated MAC and AAE of the unoxidized aerosol during the experiments as:

$$\mathrm{MAC} = b_{abs}/m_p \quad (3.1)$$

$$\mathrm{MAC} = \mathrm{MAC}_{532}\,(\frac{532}{\lambda})^{\mathrm{AAE}} \quad (3.2)$$

Where $MAC_{532}$ is the MAC at 532 nm, λ is the wavelength, and AAE was obtained by fitting a power-law function to equation 3.2.

We used these real-time calculations to tune the combustion conditions to produce BrC with a range of light-absorption properties. Producing the dark BrC also involved passing the emissions through a thermodenuder maintained at 200 °C (see Section 3.2.1).

We retrieved the wavelength-dependent BrC imaginary part of the refractive indices ($k$) from these measurements using optical closure (Saleh et al. 2014; Lack et al. 2012). The optical closure procedure involved fitting $b_{abs}$ at 473, 532, and 671 nm obtained using Mie theory calculations to $b_{abs}$ measured by the DPAS. Inputs to Mie calculations included the particle size distributions measured by the SMPS and the real part of the refractive index. The latter was assumed to be wavelength-independent with a value between 1.6 and 1.7, which are typical values observed for BrC (Saleh et al. 2014; Li, He, Hettiyadura et al. 2019; Li, He, Schade et al. 2019). The imaginary part of the refractive indices at each wavelength ($k_{473}$, $k_{532}$, $k_{671}$) were fitting parameters. We then

calculated the wavelength dependence (*w*) as the exponent of a power-law fit of the retrieved $k_{473}$, $k_{532}$, $k_{671}$ versus wavelength.

### 3.2.4. Chemical speciation

Volatile organic compounds (VOCs) and oxygenated VOCs (OVOCs) were measured using a Vocus Proton Transfer Reaction Time-of-Flight Mass Spectrometer (PTR-MS, Tofwerk/Aerodyne) (Krechmer et al. 2018) with $H_3O^+$ reagent ion. PTR-MS data were analyzed using the Tofware software package (Tofwerk AG, Aerodyne Research, Inc.) implemented in IGOR Pro (Wavemetrics, Inc.). Ensemble mass spectra of the particles and their aerodynamic size distributions were measured with two Aerodyne time-of-flight aerosol mass spectrometers (AMS). One AMS was operated with the standard tungsten vaporizer configuration to enable detection of non-refractory aerosol components with flash vaporization at 600 °C followed by electron impact ionization and time-of-flight mass spectrometry (e.g., Decarlo et al. 2006). This AMS was equipped with a long high-resolution (resolving power up to ~ 8,000 □m/m) time-of-flight mass spectrometer (L-ToF-AMS). The other AMS, a soot particle aerosol mass spectrometer (SP-AMS), was operated with a λ = 1064 nm laser vaporizer to enable detection of aerosol components that absorb at 1064 nm as well as species internally mixed with the absorbing aerosols (Onasch et al. 2012). The tungsten vaporizer was removed so that only absorbing particles were detected. This AMS used a high resolution TOFMS with resolving power up to ~ 4,000 □m/m. Elemental analysis yielding O/C, H/C, and N/C ratios was performed on AMS measurements using the SQUIRREL/PIKA software package implemented in IGOR Pro (Aiken et al. 2007; Canagaratna et al. 2015). To calculate N/C, we assumed that AMS signals at m/z = 30 ($NO^+$) and m/z = 46

($NO_2^+$) were associated with PAH + $NO_3$ oxidation products (details in Section 3.3.2.1) and therefore were classified as organics in the software.

## 3.3. Results and Discussion

### 3.3.1. Evolution of light-absorption properties

By tuning the combustion conditions of toluene, we generated BrC with varying light-absorption properties, which we categorized as light ($k_{473}$ = 0.021, $k_{532}$ = 0.008, $k_{671}$ = 0.004, $w$ = 6.2), medium ($k_{473}$ = 0.053, $k_{532}$ = 0.026, $k_{671}$ = 0.020, $w$ = 3.6), and dark ($k_{473}$ = 0.099, $k_{532}$ = 0.091, $k_{671}$ = 0.081, $w$ = 0.6). We note that the descriptors light, medium, and dark are not meant to be associated with the corresponding $k$ values in an absolute sense, but are introduced to facilitate discussing the results. The evolution of the retrieved $k$ and $w$ after exposure to $NO_3$ is depicted in Figures 2a and 2b, respectively. The $k$ values of the oxidized BrC are normalized to those of the unoxidized BrC for ease of visual comparison across different wavelengths and different samples. The absolute $k$ values of the oxidized BrC can be calculated by multiplying the ratios in Figure 3.2a with the values of unoxidized BrC above, and they are also given in Table S3.1 in the SI. The light BrC underwent a 10% decrease in $k_{473}$, 30% increase in $k_{532}$, and more than a factor of 2 increase in $k_{671}$, which is manifested as an overall decrease in $w$ of approximately 50% (Figure 3.2b). This indicates that $NO_3$-induced oxidation added chromophores that are significantly darker (larger mid-visible $k$ with a flatter wavelength dependence) than those existing in the parent PAHs. The medium BrC underwent a 7% increase in $k_{473}$, 30% increase in $k_{532}$, and 20% increase in $k_{671}$. This indicates that for the medium BrC, $NO_3$-induced oxidation also added chromophores that are darker than the original parent PAHs. The dark BrC experienced the smallest change in light-absorption properties. It underwent a 7% increase $k_{473}$, 3% decrease in $k_{532}$, and 2% decrease $k_{671}$,

which is an indication of the addition of chromophores that are, on average, relatively lighter than the parent PAHs. In Section 3.3.2, we discuss the differences in the evolution of light-absorption properties between the light, medium, and dark BrC in the context of differences in their chemical evolution in the OFR.

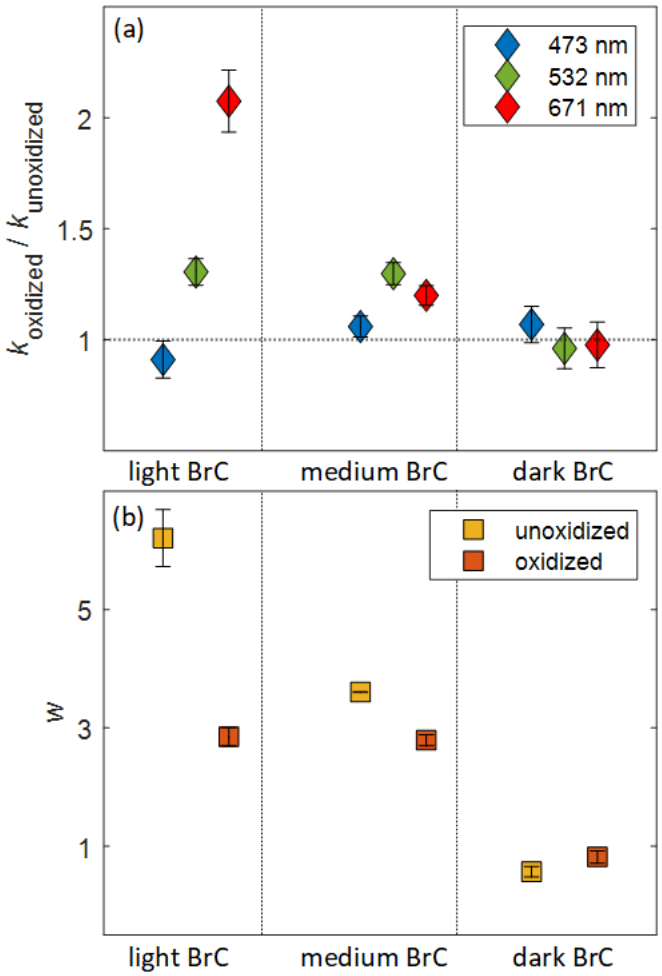


**Figure 3.2:** (a) Evolution of the imaginary part of refractive index ($k$) at $\lambda$ = 473, 532, and 671 nm of light, medium, and dark BrC, quantified as the ratio of $k$ of the oxidized BrC ($k_{oxidized}$), to $k$ of the unoxidized BrC ($k_{unoxidized}$). (b) The corresponding evolution of the wavelength dependence

(*w*). Smaller *w* is indicative of darker BrC. Error bars represent standard deviations over time for one experiment. Numerical values of $k_{\text{unoxidized}}$, $k_{\text{oxidized}}$, and *w* are given in Table S3.1.

### 3.3.2. Evolution of aerosol chemical composition

#### 3.3.2.1. AMS and SP-AMS measurements of unoxidized and oxidized BrC

As described in Section 3.2.4, we characterized the aerosol chemical composition using an AMS and an SP-AMS. The AMS detected non-refractory components of the aerosol that flash-vaporized at ~ 600 °C, whereas the SP-AMS detected components that absorbed the 1064 nm laser as well as components internally mixed with these strong absorbers. Figure 3.3 compares the normalized AMS (Figure 3.3a) and SP-AMS (Figure 3.3b) spectra of the unoxidized light and dark BrC aerosols. There are two points to make. First, the dark BrC spectra detected by both the AMS and SP-AMS contain organics with larger *m/z* compared to the light BrC spectra. This is in agreement with our previous results showing an association between BrC darkness and molecular size (Saleh et al. 2018). Second, for the same BrC (i.e., light or dark), the SP-AMS spectra are skewed to larger *m/z* compared to the AMS spectra. This can be interpreted based on the association between BrC molecular size, volatility, and light absorption (Saleh et al. 2018), and how these properties affect the detection efficiency of the two instruments. Specifically, the small-molecular-size BrC components have moderate volatilities and can readily flash-vaporize at 600 °C and be detected by the AMS. However, they are weakly absorbing and therefore do not efficiently absorb the 1064 nm laser, leading to low detection efficiency by the SP-AMS. On the other hand, the large-molecular-size BrC components have extremely low volatilities and do not readily flash-vaporize at 600 °C, leading to low detection efficiency by the AMS. However, they are strongly absorbing and can therefore efficiently absorb the 1064 nm laser (along with BC), leading to higher detection

efficiency by the SP-AMS. However, BC is likely a minor component of the particles that were generated, for two reasons. First, as shown in Figure S3.1, the SMPS volume distribution is unimodal with a relatively small mode diameter (~60 nm). The presence of BC would manifest as a second larger mode. Second SEM images of particles formed at similar combustion conditions in a previous study revealed near-spherical particles, indicative of pure OA, where BC-containing particles exhibited irregular shapes (Saleh et al. 2018).

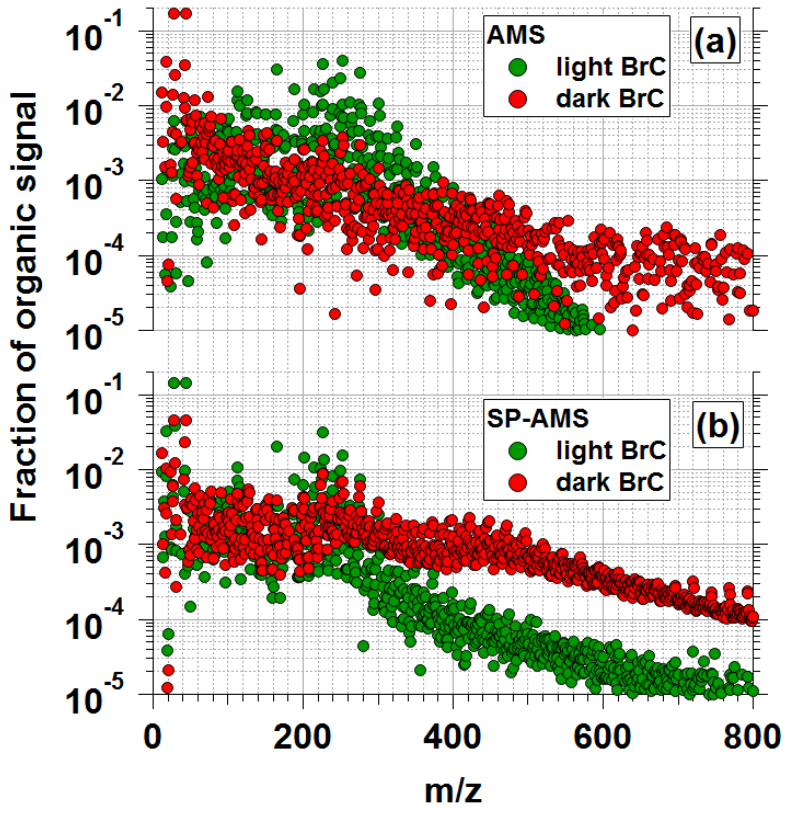


**Figure 3.3.** AMS and SP-AMS UMR spectra of organic aerosol components in unoxidized light BrC and dark BrC aerosols.

We observed a difference between the total OA concentrations detected by the AMS and SP-AMS for the light and dark BrC. For the light BrC, the OA concentration detected by the AMS was

approximately a factor of 20 larger than the SP-AMS (Table S3.1). On the other hand, for the dark BrC the OA concentration detected by the SP-AMS was approximately a factor of 6 larger than the OA concentration detected by the AMS (Table S3.1). In addition to the large-molecular-size organic species shown in Figure 3.3, the SP-AMS spectra of the dark BrC also contained signals at m/z = 12x that represent carbon clusters ($C_x$, where x = 1 to 9) typically associated with BC and a series of signals at m/z = 720 + 24x that represent trace fullerenes ($C_{60+2x}$) present in the aerosols and/or formed in the laser (Onasch et al. 2015). These components likely also contributed to the absorption of the 1064 nm laser by the aerosol and overall increase in the SP-AMS detection efficiency.

This picture changed dramatically after oxidation. Due to the significant increase in light absorption induced by oxidation with $NO_3$ (Section 3.3.1 and Figure 3.2), the oxidized light BrC was significantly more efficient at absorbing the SP-AMS 1064 nm laser than the parent molecules (i.e., unoxidized light BrC) resulting in more than an order-of-magnitude increase in detection efficiency by the SP-AMS. Consequently, the ratio of AMS OA to SP-AMS OA dropped from 20 to 2 after oxidation (Table S3.1). Results and discussion in the subsequent sections are based on AMS measurements of light and medium BrC and SP-AMS measurements of dark BrC.

Figure 3.4 reveals additional noteworthy changes in the AMS and SP-AMS spectra of BrC following exposure to $NO_3$ radicals in the OFR. First, $NO_3$ exposure led to an increase in signals at *m/z* = 30 and 46 ($NO^+$ and $NO_2^+$) and m/z = 44 ($CO_2^+$). Because negligible $NH_4^+$ is present, and because the $NO^+$:$NO_2^+$ ratio in oxidized BrC (1.6-2.1) was higher than the $NO^+$:$NO_2^+$ ratio in ammonium nitrate measured by the same AMS instrument (1.2), these signals can be attributed to PAH + $NO_3$ oxidation products such as nitro-PAHs rather than particulate inorganic nitrates.

However, we note that $NO^+$:$NO_2^+$ values measured in this work are different from $NO^+$:$NO_2^+$ of particulate organic nitrates studied previously (Bruns et al. 2010; Farmer et al. 2010), perhaps indicating different behavior of nitroaromatics in the AMS. The $CO_2^+$ signal is associated with decarboxylation of organic acids in the AMS (Canagaratna et al. 2015). Second, the organic mass per particle measured by the AMS increased following $NO_3$ exposure, indicating OA enhancement by SOA formation or heterogeneous oxidation. Third, the oxidized BrC spectra (Figures 4b and 4d) were shifted towards smaller carbon-number fragment ions than the corresponding unoxidized BrC spectra (Figures 4a and 4c). These changes may be due to condensation of gas-phase PAH + $NO_3$ oxidation products and/or functionalization of condensed-phase PAHs following heterogeneous oxidation by $NO_3$. The potential contributions of these processes are discussed in more detail in Section 3.3.2.3. Corresponding high-resolution AMS and SP-AMS spectra colored by $C_xH_y$, $C_xH_yO_z$, $C_xH_yO_zN$, $C_xH_yN$ ion families are shown in Figures S3-S6 in the SI.

**3.3.2.2. Evolution of elemental composition**

The evolution of O/C, H/C, and N/C of the light, medium, and dark BrC due to oxidation with $NO_3$ is depicted in the van Krevelen diagram (Heald et al. 2010) in Figure 3.5. We calculated H/C and O/C ratio using the improved-ambient method (Canagaratna et al. 2015) and N/C ratio using the method of Aiken et al. (2007). $NO_3$ exposure resulted in an increase in H/C, O/C, and N/C for all PAHs. The increase in nitrogen content is associated with the addition of nitro ($-NO_2$) groups (Figure 3.4), either by heterogeneous oxidation or gas-phase oxidation followed by condensation. On the other hand, approximately half of the increase in oxygen content is associated with the addition of nitro groups and half was associated with the addition of other functional groups including carboxylic acids, carbonyls, and alcohols.

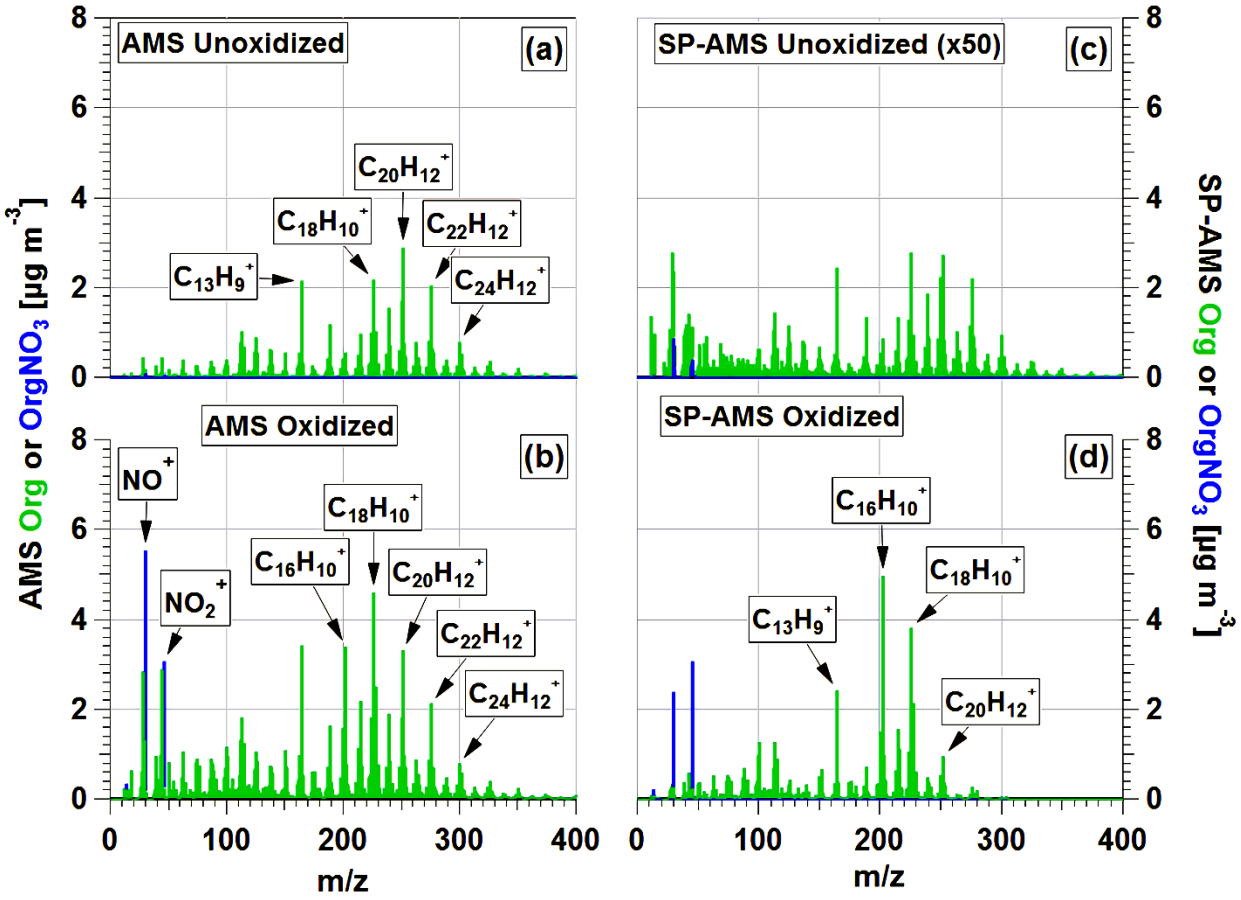


**Figure 3.4.** (a) AMS and (b) SP-AMS HR spectra of organic and nitrate signals in the unoxidized light BrC, and (c) AMS and (d) SP-AMS HR spectra of organic and nitrate signals in the oxidized light BrC (exposed to $NO_3$ radicals at 2.4 nights of equivalent atmospheric $NO_3$ exposure).

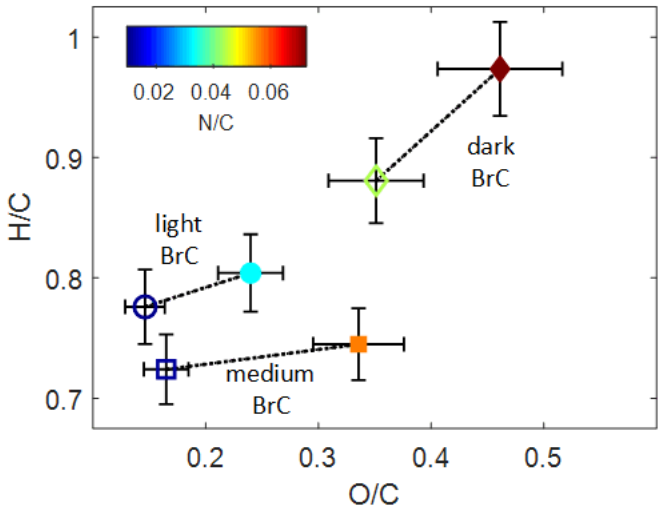


**Figure 3.5:** Van Krevelen diagram showing the H/C versus O/C for unoxidized (open symbols) and oxidized (solid symbols) BrC. Symbols are colored by N/C. Error bars represent ±12% uncertainty in O/C and ±4% uncertainty in H/C (Canagaratna et al. 2015).

#### 3.3.2.3. SOA formation versus heterogeneous oxidation

The combustion emissions were passed through an activated carbon denuder (Figure 3.1) to remove residual toluene as well as gas-phase combustion products in order to minimize the effect of SOA formation relative to heterogeneous oxidation on the evolution of light-absorption properties of the BrC. The fractional removal of toluene and $C_{10}$-$C_{13}$ gas-phase PAHs was greater than 0.98, 0.99, 0.83, 0.92, and 0.13 for toluene, naphthalene ($C_{10}H_8$), acenaphthylene ($C_{12}H_8$), acenaphthene ($C_{12}H_{10}$), and fluorene ($C_{13}H_{10}$), respectively (Figure S3.2). Furthermore, after stripping semi-volatile PAHs from the gas phase, these species were expected to partition from the particle phase to the gas phase to maintain thermodynamic equilibrium, as appeared to be the case for phenanthrene/anthracene ($C_{14}H_{10}$), whose signal increased after denuding. Therefore, some

SOA formation due to gas-phase $NO_3$ oxidation and subsequent condensation of these semi-volatile PAHs is expected to occur.

To estimate the relative contribution of SOA formation versus heterogeneous oxidation to the increase in OA mass concentration after oxidation with $NO_3$, we performed elemental (C, N, O) mass balance on the OA measured by the AMS and SP-AMS before and after oxidation. The functional groups that can potentially be added to the condensed phase by heterogeneous oxidation contain only nitrogen or oxygen. Therefore, any increase in carbon after oxidation was attributed to SOA formation. The carbon mass balance showed that SOA formation constituted 8%, 15%, and 37% of the carbon mass of the oxidized particles for the light, medium, and dark BrC, respectively. The relatively high SOA fraction in the dark BrC experiments may have been a consequence of semivolatile PAHs that evaporated inside the thermodenuder used to isolate the dark BrC (Section 2.1) and were subsequently oxidized in the OFR to generate SOA. As discussed in Section 3.3.3, the difference in the fractional contribution of SOA formation for the different BrC samples played a key role in the observed evolution in light-absorption properties (Figure 3.2).

While the increase in carbon mass was clearly related to SOA formation, the increase in oxygen and nitrogen mass was potentially contributed from both SOA formation and/or heterogeneous oxidation processes. To estimate the relative contributions of each process, we applied the following constraints:

1. We assumed that condensable molecules formed from gas-phase PAH + $NO_3$ reactions contained carbon numbers ($C_\#$) ranging from 10 (e.g., naphthalene) to 18 (e.g., chrysene). Known oxidation products of naphthalene (e.g., nitro-naphthalene) have saturation vapor

pressures ($P_{sat}$) > $10^{-2}$ Pa (Bandowe and Meusel 2017), corresponding to saturation concentration ($m_{sat}$) > $10^3$ μg $m^{-3}$, which is at the upper limit of what could significantly partition to the particle phase in our experiments, where typical OA mass concentrations ($m_{OA}$) were 100-200 μg $m^{-3}$. On the other hand, species with $C_{\#}$ > 18 have $P_{sat}$ < $10^{-5}$ Pa ($m_{sat}$ < 1 μg $m^{-3}$ ) (Keyte et al. 2013) and are therefore expected to exist almost exclusively in the condensed phase.

2. We assumed that each condensing molecule contained nitrogen numbers ($N_{\#}$) ranging from 0 to 1 and oxygen numbers ($O_{\#}$) ranging from 2 to 4 (Sasaki et al. 1997; Zielinska et al. 1989; Atkinson et al. 1990). We did not impose upper limits on $N_{\#}$ and $O_{\#}$ contributed from heterogeneous oxidation processes (Liu et al. 2012).

Based on these constraints, we obtained possible ranges of the amounts of nitrogen and oxygen that can be brought into the particles via SOA formation ($\Delta N_{cond}$ and $\Delta O_{cond}$) as a function of $C_{\#}$ of the condensing molecules. We then subtracted these values from the total amounts of added nitrogen and oxygen ($\Delta N_{tot}$ and $\Delta O_{tot}$) obtained from the mass balance to calculate the amounts of nitrogen and oxygen added via heterogeneous oxidation ($\Delta N_{het}$ and $\Delta O_{het}$).

The results of these calculations are shown in Figure 3.6 for light, medium, and dark BrC. As expected, the contribution of heterogeneous oxidation to adding nitrogen ($\Delta N_{het}$ / $\Delta N_{tot}$) and oxygen ($\Delta O_{het}$ / $\Delta O_{tot}$) is inversely proportional to the assumed nitrogen and oxygen content of the SOA molecules. For the light and medium BrC, heterogeneous oxidation is expected to be the dominant mechanism in adding nitrogen and oxygen to the particles, with $\Delta N_{het}$ / $\Delta N_{tot}$ ranging from 0.7 to 1 and $\Delta O_{het}$ / $\Delta O_{tot}$ ranging from 0.6 to 0.9 as a function of $C_{\#}$ for all assumed cases. On the other hand, the contribution of heterogeneous oxidation to dark BrC was more sensitive to

the assumed composition of the condensing molecules, with $\Delta N_{het} / \Delta N_{tot}$ and $\Delta O_{het} / \Delta O_{tot}$ ranging from 0.2 to 1. While these calculations are speculative, they suggest that SOA formation may have a more prominent role in the chemical evolution of the dark BrC than for the light and medium BrC in our experiments, which is relevant to explaining the discrepancy in the evolution of light-absorption properties described in the next section.

### 3.3.3. The competing effects of SOA formation and heterogeneous oxidation on the evolution of light-absorption properties

As described in Section 3.3.1 and shown in Figure 3.2, $NO_3$-induced oxidation led to a relatively significant increase in darkness of the light BrC, a moderate increase in darkness of the medium BrC, and a minor decrease in darkness of the dark BrC. The different trends can be understood as:

1. The light-absorption properties of the oxidized BrC are average properties of the heterogeneously oxidized PAHs and the condensed oxidized PAHs (SOA).
2. The contribution of SOA to the average light-absorption properties is proportional to the relative amount of SOA, which is most significant for the dark BrC, followed by the medium BrC, then the light BrC (Section 3.2.3).
3. The molecular sizes of the gas-phase precursors of SOA are much smaller than the average molecular size of the unoxidized particulate PAHs and are therefore much less absorptive in the visible spectrum (Saleh et al. 2018). While the SOA generated from $NO_3$ oxidation is more absorptive than its gas-phase precursors, it is expected to be significantly less absorptive than the unoxidized particulate PAHs if our $N\# \leq 1$ assumption is justified (Section 3.2.3). Therefore, SOA presumably decreases the overall absorption of oxidized BrC.

4. Heterogeneous oxidation with $NO_3$ is expected to add chromophoric functional groups to the parent particulate PAHs (Lu et al. 2011; Zimmermann et al. 2013; Zhang et al. 2013; Jariyasopit et al. 2014) thus increasing the overall absorption by the oxidized BrC, especially if multiple nitrogen-containing functional groups are added (Liu et al. 2012).

To illustrate the competing effects of SOA formation and heterogeneous oxidation, we performed simplified calculations to isolate the effect of heterogeneous oxidation on the evolution of the light-absorption properties of the BrC particles. To do so, we represented the evolution of the BrC in the OFR in two phenomena: a heterogeneous oxidation step that changes the $k$ of the BrC from $k_{unoxidized}$ to $k_{het}$, and an SOA formation step that "dilutes" $k_{het}$ by adding the weakly absorbing SOA molecules to the BrC. To retrieve $k_{het}$, we assumed that the $k$ of the oxidized BrC ($k_{oxidized}$) is a mass-weighted average of $k_{het}$ and $k_{SOA}$:

$$k_{oxidized} = y_{SOA}\, k_{SOA} + y_{het}\, k_{het} \quad (3.3)$$

Where $y_{SOA}$ and $y_{het}$ are the corresponding mass fractions obtained from the mass balance (Section 3.2.3).

For the light BrC, SOA constituted only 8% of the carbon mass of the oxidized BrC. Therefore, addition of chromophoric functional groups via $NO_3$-induced heterogeneous oxidation dominated the overall evolution of the light-absorption properties of the oxidized BrC because $k_{het}$ and $k_{oxidized}$ were similar (Figure 3.7). On the other hand, SOA constituted 37% of the carbon mass of the oxidized dark BrC and therefore had a more significant influence on its light-absorption properties. Assuming that the SOA was significantly less absorptive than the unoxidized particulate PAHs, it effectively "diluted" the overall absorption and led to the observed small decrease in absorption at

the mid- and long-visible wavelengths (Figure 3.2 and Figure 3.7). However, isolating the effect of heterogeneous oxidation reveals that, similar to the light BrC, reaction with $NO_3$ also added chromophoric functional groups to the dark PAHs as manifested in an enhanced $k_{het}$ relative to $k_{unoxidized}$ (Figure 3.7).

With the absence of knowledge of actual $k_{SOA}$ values, the calculations presented in Figure 3.7 are not meant to be quantitative. However, they indicate that heterogeneous oxidation with $NO_3$ led to a similar increase in light absorption (i.e., similar $k_{het}$ / $k_{unoxidized}$) for the light, medium, and dark BrC, and that the observed differences in the evolution of their light-absorption properties ($k_{oxidized}$ / $k_{unoxidized}$) may have been due to the difference in SOA contribution to the particle mass and overall absorption.

Our results are qualitatively consistent with the recent findings of Li, He, Hettiyadura et al. (2019). That study reported an increase in $k$ of wood-tar BrC of approximately a factor of 2 in the visible wavelengths and 40% in the UV wavelengths after 13.3 hours of equivalent atmospheric $NO_3$ oxidation in an OFR. The atmospheric-equivalent $NO_3$ exposure in Li, He, Hettiyadura et al. (2019) was significantly shorter than our study (13.3 hours vs 2.4 nights), yet their absorption enhancements are on the high end of ours. This could possibly be due to differences in experimental conditions, or BrC chemical structure. Nevertheless, both studies indicate that heterogeneous $NO_3$ oxidation is an important mechanism for enhancing BrC absorption that should be further investigated using more diverse BrC systems and $NO_3$ exposure conditions.

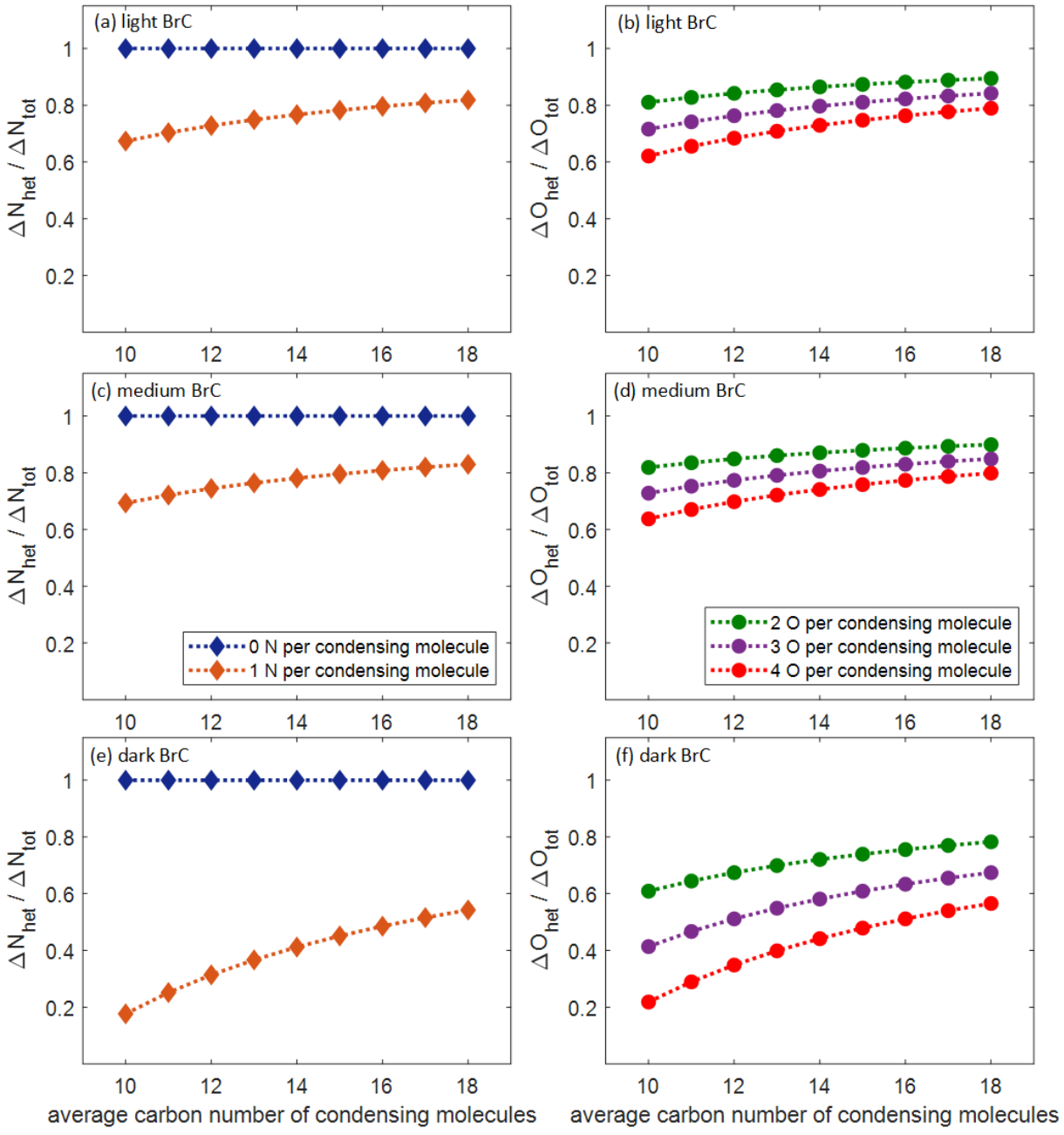


**Figure 3.6.** Calculated relative contribution of heterogeneous oxidation to adding nitrogen ($\Delta N_{het}$ / $\Delta N_{tot}$) and oxygen ($\Delta O_{het}$ / $\Delta O_{tot}$) to the condensed phase as a function of assumed average carbon number of the condensing SOA molecules for (a, b) light, (c, d) medium, and (e, f) dark BrC.

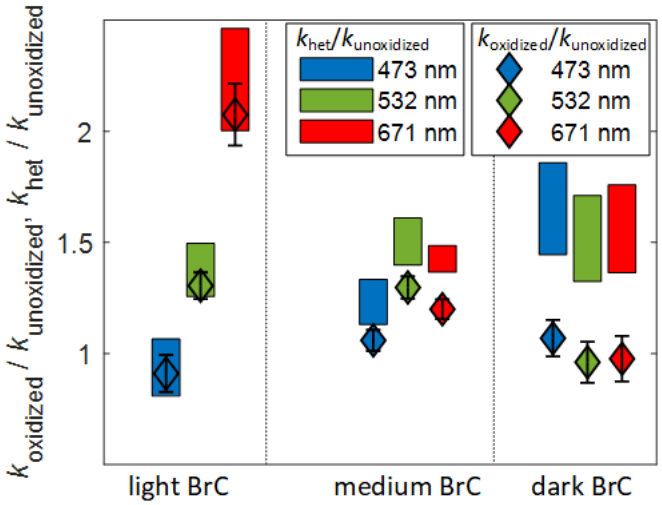


**Figure 3.7.** Effect of heterogeneous oxidation on light-absorption properties of the light, medium, and dark BrC. The bars represent ranges of $k_{het}$ / $k_{unoxidized}$ calculated based on equation 3.3. They reflect the assumed range of $k_{SOA}$ as well as the uncertainty in $k_{oxidized}$ and $k_{unoxidized}$ (Table S3.1). The diamonds represent $k_{oxidized}$ / $k_{unoxidized}$ (the same as in Figure 3.2), added here for reference to compare the effect of heterogeneous oxidation to the overall observed oxidation. Error bars represent standard deviations over time for one

### 3.3.4. Atmospheric implications

Our results suggest that light absorption by BrC is enhanced following $NO_3$-induced heterogenous oxidation, while condensable products of gas-phase PAH + $NO_3$ reactions may partially offset this enhancement. The majority of studies on atmospheric evolution of BrC have focused on daytime aging, leading to the large body of evidence on the bleaching of BrC due to oxidative destruction of BrC chromophores driven by OH oxidation or photolysis (e.g., Browne et al. 2019; Sumlin et al. 2017; Zhao et al. 2015; Wong, Nenes, and Weber 2017; Wong et al. 2019; Satish et al. 2017; Dasari et al. 2019; Forrister et al. 2015; Sarkar et al. 2019). On the other hand, observations of

nighttime atmospheric evolution of BrC are scarce. Two complementary studies (Lin et al. 2017; Bluvshtein et al. 2017) performed optical and chemical speciation measurements of atmospheric BrC at night following a large-scale bonfire event. Bluvshtein et al. (2017) reported an increase in *k* values of the (biomass-burning dominated) atmospheric BrC in the mid-visible range in the night hours following the bonfire event, suggesting enhanced BrC absorption due to nighttime aging. Lin et al. (2017) reported that unlike fresh biomass-burning BrC chromophores which were dominated by aromatic compounds with no nitro groups (Lin et al. 2016), the nighttime aged BrC chromophores were dominated by nitroaromatic species that were formed from $NO_3$ oxidation of aromatic precursors. The evidence from these two studies points to the importance of the enhancement of BrC absorption due to nighttime reactions with $NO_3$. Our controlled combustion and $NO_3$ oxidation experiments provide support for these atmospheric observations and motivate the need for further systematic atmospheric measurements that target the nighttime aging of BrC.

### 3.4. Conclusions

We performed toluene-combustion experiments controlled at different combustion conditions to produce BrC with varying light-absorption properties, which we categorized as light, medium, and dark BrC. By exposing the BrC to $NO_3$ in an OFR, we investigated the evolution of the BrC chemical composition and light-absorption properties due to $NO_3$-induced oxidation. The BrC evolved chemically due to both heterogeneous oxidation of the particulate PAHs as well as SOA formation driven by gas-phase oxidation and subsequent condensation of PAH vapors. We performed calculations to decouple the effects of heterogeneous oxidation and SOA formation on the evolution of the light-absorption properties of the BrC and showed that heterogeneous oxidation adds chromophoric functional groups that significantly increased light absorption by all

the 3 BrC types. On the other hand, the oxidized PAHs that contributed to SOA were likely less absorbing than the particulate PAHs, thereby reducing the overall light absorption of the oxidized BrC. Unlike with the light and medium BrC experiments, SOA formation was prominent in the dark BrC experiments, which was manifested as a slight decrease in overall absorption upon oxidation with $NO_3$. However, this effect may have been specific to experimental conditions that suppressed the relative importance of heterogenous oxidation processes because of the short OFR residence time. $NO_3$-induced heterogeneous reactions are expected to be more important than gas-phase reactions at atmospheric conditions. Therefore, night-time oxidation with $NO_3$ is expected to enhance the light absorption of some atmospheric BrC species.

**Acknowledgments**

The authors gratefully thank Manjula Canagaratna, Philip Croteau, Douglas Worsnop, John Jayne, Joseph Roscioli, and David Nelson (ARI) for helpful discussions.

**Funding**

Financial support was provided by the National Science Foundation, Division of Atmospheric and Geospace Sciences (AGS-1748080).

## References


Adachi, K., A. J. Sedlacek III, L. Kleinman, D. Chand, M. John, P. R. Buseck, K. Adachi, et al. 2018. Volume Changes upon Heating of Aerosol Particles from Biomass Burning Using Transmission Electron Microscopy. *Aerosol Science and Technology* 52 (1): 46–56. doi.org/10.1080/02786826.2017.1373181.

Adler, G., N. L. Wagner, K. D. Lamb, K. M. Manfred, J. P. Schwarz, A. Franchin, A. M. Middlebrook, et al. 2019. Evidence in Biomass Burning Smoke for a Light- Absorbing Aerosol with Properties Intermediate between Brown and Black Carbon. *Aerosol Science and Technology* 53 (9): 976–89. doi.org/10.1080/02786826.2019.1617832.

Aiken, A. C., P. F. Decarlo, and J. L. Jimenez. 2007. Elemental Analysis of Organic Species with Electron Ionization High-Resolution Mass Spectrometry. *Anal. Chem.* 79 (21): 8350–58. doi.org/10.1021/ac071150w.

Atkinson, R. 1991. Kinetics and Mechanisms of the Gas-Phase Reactions of the $NO_3$ Radical with Organic Compounds. *J. Phys. Chem. Ref. Data 20,* 20 (3): 459–506. doi.org/10.1063/1.555887.

Atkinson, R., J. Arey, B. Zielinska, and S. M. Aschmann. 1990. Kinetics and Nitro-Products of the Gas-Phase OH and $NO_3$ Radical-Initiated Reactions of Naphthalene-D8 Fluoranthene-D10, and Pyrene. *International Journal of Chemical Kinetics* 22: 999–1014.

doi.org/10.1002/kin.550220910.

Bandowe, B. A. M., and H. Meusel. 2017. Nitrated Polycyclic Aromatic Hydrocarbons (Nitro-PAHs) in the Environment – A Review. *Science of the Total Environment* 581–582: 237–57. doi.org/10.1016/j.scitotenv.2016.12.115.

Bluvshtein, N., P. Lin, J. M. Flores, L. Segev, Y. Mazar, E. Tas, G. Snider, et al. 2017. Broadband Optical Properties of Biomass-Burning Aerosol and Identification of Brown Carbon Chromophores. *J. Geophys. Res. Atmos.* 122: 5441–56. doi.org/10.1002/2016JD026230.

Brown, H., X. Liu, Y. Feng, Y. Jiang, M. Wu, Z. Lu, and C. Wu. 2018. Radiative Effect and Climate Impacts of Brown Carbon with the Community Atmosphere Model (CAM5). *Atmos. Chem. Phys.* 18: 17745–68.

Browne, E. C., X. Zhang, J. P. Franklin, K. J. Ridley, T. W. Kirchstetter, K. R. Wilson, C. D. Cappa, et al. 2019. Effect of Heterogeneous Oxidative Aging on Light Absorption by Biomass Burning Organic Aerosol. *Aerosol Science and Technology* 53 (6): 663–74. doi.org/10.1080/02786826.2019.1599321.

Bruns, E. A., A. Zelenyuk, M. J. Ezell, S. N. Johnson, Y. Yu, and D. A. N. Imre. 2010. Comparison of FTIR and Particle Mass Spectrometry for the Measurement of Particulate Organic Nitrates. *Environ. Sci. Technol.* 44 (3): 1056–61.

Canagaratna, M. R., J. L. Jimenez, J. H. Kroll, Q. Chen, S. H. Kessler, P. Massoli, L. H. Ruiz, et al. 2015. Elemental Ratio Measurements of Organic Compounds Using Aerosol Mass Spectrometry: Characterization, Improved Calibration, and Implications. *Atmos. Chem. Phys.*

15: 253–72. doi.org/10.5194/acp-15-253-2015.

Cheng, Z., K. Atwi, T. Onyima, and R. Saleh. 2019. Investigating the Dependence of Light-Absorption Properties of Combustion Carbonaceous Aerosols on Combustion Conditions. *Aerosol Science and Technology* 53 (4): 419–34. doi.org/10.1080/02786826.2019.1566593.

Claeys, M., R. Vermeylen, F. Yasmeen, Y. Gómez-González, X. Chi, W. Maenhaut, T. Mészáros, and I. Salma. 2012. Chemical Characterisation of Humic-like Substances from Urban, Rural and Tropical Biomass Burning Environments Using Liquid Chromatography with UV/Vis Photodiode Array Detection and Electrospray Ionisation Mass Spectrometry. *Environmental Chemistry* 9 (3): 273–84. doi.org/10.1071/EN11163.

Dasari, S., A. Andersson, S. Bikkina, H. Holmstrand, K. Budhavant, S. Satheesh, E. Asmi, et al. 2019. Photochemical Degradation Affects the Light Absorption of Water-Soluble Brown Carbon in the South Asian Outflow. *Sci. Adv.* 5 (1): eaau8066.

Decarlo, P. F., J. R. Kimmel, A. Trimborn, M. J. Northway, J. T. Jayne, A. C. Aiken, M. Gonin, et al. 2006. Field-Deployable, High-Resolution, Time-of-Flight Aerosol Mass Spectrometer. *Anal. Chem.* 78 (24): 8281–89. doi.org/10.1021/ac061249n.

Desyaterik, Y., Y. Sun, X. Shen, T. Lee, X. Wang, T. Wang, and J. L. C. Jr. 2013. Speciation of "Brown" Carbon in Cloud Water Impacted by Agricultural Biomass Burning in Eastern China. *J. Geophys. Res. Atmos.* 118: 7389–99. doi.org/10.1002/jgrd.50561.

Farmer, D. K., A. Matsunaga, K. S. Docherty, J. D. Surratt, J. H. Seinfeld, P. J. Ziemann, and J. L. Jimenez. 2010. Response of an Aerosol Mass Spectrometer to Organonitrates and

Organosulfates and Implications for Atmospheric Chemistry. *PNAS* 107 (15): 6670–75. doi.org/10.1073/pnas.0912340107.

Feng, Y., V. Ramanathan, and V. R. Kotamarthi. 2013. Brown Carbon: A Significant Atmospheric Absorber of Solar Radiation? *Atmos. Chem. Phys.* 13 (17): 8607–21. doi.org/10.5194/acp-13-8607-2013.

Forrister, H., J. Liu, E. Scheuer, J. Dibb, L. Ziemba, K. L. Thornhill, B. Anderson, et al. 2015. Evolution of Brown Carbon in Wildfire Plumes. *Geophys. Res. Lett.* 42: 4623–30. doi.org/10.1002/2015GL063897.Received.

Hammer, M. S., R. V Martin, A. Van Donkelaar, V. Buchard, O. Torres, D. A. Ridley, and R. J. D. Spurr. 2016. Interpreting the Ultraviolet Aerosol Index Observed with the OMI Satellite Instrument to Understand Absorption by Organic Aerosols: Implications for Atmospheric Oxidation and Direct Radiative Effects. *Atmos. Chem. Phys.* 16: 2507–23. doi.org/10.5194/acp-16-2507-2016.

Heald, C. L., J. H. Kroll, J. L. Jimenez, K. S. Docherty, P. F. Decarlo, A. C. Aiken, Q. Chen, S. T. Martin, D. K. Farmer, and P. Artaxo. 2010. A Simplified Description of the Evolution of Organic Aerosol Composition in the Atmosphere. *Geophys. Res. Lett.* 37: L08803. doi.org/10.1029/2010GL042737.

Hoffer, A., A. Tóth, I. NyirÅ'-Kósa, M. Pósfai, and A. Gelencsér. 2016. Light Absorption Properties of Laboratory-Generated Tar Ball Particles. *Atmos. Chem. Phys.* 16 (1): 239–46. doi.org/10.5194/acp-16-239-2016.

Jariyasopit, N., M. Mcintosh, K. Zimmermann, J. Arey, R. Atkinson, P. H. Cheong, R. G. Carter, T. Yu, R. H. Dashwood, and S. L. M. Simonich. 2014. Novel Nitro-PAH Formation from Heterogeneous Reactions of PAHs with $NO_2$, $NO_3/N_2O_5$, and OH Radicals: Prediction, Laboratory Studies, and Mutagenicity. *Environ. Sci. Technol.* 48: 412−419. doi.org/10.1021/es4043808.

Jethva, H., and O. Torres. 2011. Satellite-Based Evidence of Wavelength-Dependent Aerosol Absorption in Biomass Burning Smoke Inferred from Ozone Monitoring Instrument. *Atmos. Chem. Phys.* 11: 10541–51. doi.org/10.5194/acp-11-10541-2011.

Jo, D. S., R. J. Park, S. Lee, S. Kim, and X. Zhang. 2016. A Global Simulation of Brown Carbon: Implications for Photochemistry and Direct Radiative Effect. *Atmos. Chem. Phys.* 16: 3413–32. doi.org/10.5194/acp-16-3413-2016.

Karavalakis, G., V. Boutsika, S. Stournas, and E. Bakeas. 2011. Biodiesel Emissions Profile in Modern Diesel Vehicles. Part 2: Effect of Biodiesel Origin on Carbonyl, PAH, Nitro-PAH and Oxy-PAH Emissions. *Science of the Total Environment, The* 409 (4): 738–47. doi.org/10.1016/j.scitotenv.2010.11.010.

Keyte, I. J., R. M. Harrisonz, and G. Lammel. 2013. Chemical Reactivity and Long-Range Transport Potential of Polycyclic Aromatic Hydrocarbons – a Review. *Chem. Soc. Rev.* 42: 9333--9391. doi.org/10.1039/c3cs60147a.

Knopf, D. A., S. M. Forrester, and J. H. Slade. 2011. Heterogeneous Oxidation Kinetics of Organic Biomass Burning Aerosol. *Phys. Chem. Chem. Phys* 13: 21050–62. doi.org/10.1039/c1cp22478f.

Krechmer, J., F. Lopez-hilfiker, A. Koss, M. Hutterli, C. Stoermer, B. Deming, J. Kimmel, et al. 2018. Evaluation of a New Reagent-Ion Source and Focusing Ion-Molecule Reactor for Use in Proton-Transfer-Reaction Mass Spectrometry. *Anal. Chem.* 90: 12011−12018. doi.org/10.1021/acs.analchem.8b02641.

Kwamena, N. A., and J. P. D. Abbatt. 2008. Heterogeneous Nitration Reactions of Polycyclic Aromatic Hydrocarbons and N-Hexane Soot by Exposure to $NO_3/NO_2/N_2O_5$. *Atmospheric Environment* 42 (35): 8309–14. doi.org/10.1016/j.atmosenv.2008.07.037.

Kwon, D., M. J. Sovers, V. H. Grassian, P. D. Kleiber, and M. A. Young. 2018. Optical Properties of Humic Material Standards: Solution Phase and Aerosol Measurements. Research-article. *ACS Earth Space Chem.* 2: 1102–11. doi.org/10.1021/acsearthspacechem.8b00097.

Lack, D. A., J. M. Langridge, R. Bahreini, C. D. Cappa, A. M. Middlebrook, and J. P. Schwarz. 2012. Brown Carbon and Internal Mixing in Biomass Burning Particles. *PNAS* 109 (37): 14802–7. doi.org/10.1073/pnas.1206575109.

Lambe, A. T., A. T. Ahern, L. R. Williams, J. G. Slowik, J. P. S. Wong, J. P. D. Abbatt, W. H. Brune, et al. 2011. Characterization of Aerosol Photooxidation Flow Reactors: Heterogeneous Oxidation, Secondary Organic Aerosol Formation and Cloud Condensation Nuclei Activity Measurements. *Atmos. Meas. Tech.* 4: 445–61. doi.org/10.5194/amt-4-445-2011.

Lambe, Andrew T, E. C. Wood, J. E. Krechmer, F. Majluf, L. R. Williams, L. Croteau, M. Cirtog, et al. 2020. Nitrate Radical Generation via Continuous Generation of Dinitrogen Pentoxide in a Laminar Flow Reactor Coupled to an Oxidation Flow Reactor. *Atmos. Meas. Tech. 13,*

*2397–2411. doi.org/10.5194/amt-13-2397-2020.*

Laskin, A., J. Laskin, and S. A. Nizkorodov. 2015. Chemistry of Atmospheric Brown Carbon. *Chemical Reviews* 115 (10): 4335–82. doi.org/10.1021/cr5006167.

Lee, H. J., P. K. Aiona, A. Laskin, J. Laskin, and S. A. Nizkorodov. 2014. Effect of Solar Radiation on the Optical Properties and Molecular Composition of Laboratory Proxies of Atmospheric Brown Carbon. *Environ. Sci. Technol.* 48: 10217−10226. doi.org/10.1021/es502515r.

Li, C., Q. He, A. P. S. Hettiyadura, U. Käfer, G. Shmul, D. Meidan, R. Zimmermann, et al. 2019. Formation of Secondary Brown Carbon in Biomass Burning Aerosol Proxies through $NO_3$ Radical Reactions. *Environ. Sci. Technol. 54 (3): 1395−1405. doi.org/10.1021/acs.est.9b05641*.

Li, C., Q. He, J. Schade, J. Passig, R. Zimmermann, D. Meidan, A. Laskin, and Y. Rudich. 2019. Dynamic Changes in Optical and Chemical Properties of Tar Ball Aerosols by Atmospheric Photochemical Aging. *Atmos. Chem. Phys.* 19: 139–63.

Lin, P., P. K. Aiona, Y. Li, M. Shiraiwa, J. Laskin, S. A. Nizkorodov, and A. Laskin. 2016. Molecular Characterization of Brown Carbon in Biomass Burning Aerosol Particles. *Environ. Sci. Technol.* 50 (21): 11815–24. doi.org/10.1021/acs.est.6b03024.

Lin, P., N. Bluvshtein, Y. Rudich, S. A. Nizkorodov, J. Laskin, and A. Laskin. 2017. Molecular Chemistry of Atmospheric Brown Carbon Inferred from a Nationwide Biomass Burning Event. *Environ. Sci. Technol.* 51: 11561–70. doi.org/10.1021/acs.est.7b02276.

Liu, C., P. Zhang, B. Yang, Y. Wang, and J. Shu. 2012. Kinetic Studies of Heterogeneous

Reactions of Polycyclic Aromatic Hydrocarbon Aerosols with $NO_3$ Radicals. *Environ. Sci. Technol.* 46 (3): 7575−7580. doi.org/10.1021/es301403d.

Liu, D., T. Lin, J. Hussain, C. Zhineng, Y. Xu, K. Li, and Z. Gan. 2017. Concentration, Source Identification, and Exposure Risk Assessment of PM2.5-Bound Parent PAHs and Nitro-PAHs in Atmosphere from Typical Chinese Cities. *Scientific Reports* 7: 10398. doi.org/10.1038/s41598-017-10623-4.

Lu, J. W., J. M. Flores, A. Lavi, A. Abo-riziq, and Y. Rudich. 2011. Changes in the Optical Properties of Benzo[a]Pyrene-Coated Aerosols upon Heterogeneous Reactions with $NO_2$ and $NO_3$. *Phys. Chem. Chem. Phys* 13: 6484–92. doi.org/10.1039/c0cp02114h.

Mak, J., S. Gross, and A. K. Bertram. 2007. Uptake of $NO_3$ on Soot and Pyrene Surfaces. *Geophys. Res. Lett.* 34: L10804. doi.org/10.1029/2007GL029756.

Malloy, Q. G. J., S. Nakao, L. Qi, R. Austin, C. Stothers, H. Hagino, and D. R. Cocker. 2009. Real-Time Aerosol Density Determination Utilizing a Modified Scanning Mobility Particle Sizer Aerosol Particle Mass Analyzer System. *Aerosol Science and Technology* 43 (7): 673–78. doi.org/10.1080/02786820902832960.

Michelsen, H. A. 2017. Probing Soot Formation, Chemical and Physical Evolution, and Oxidation: A Review of in Situ Diagnostic Techniques and Needs. *Proceedings of the Combustion Institute* 36 (1): 717–35. doi.org/10.1016/j.proci.2016.08.027.

Moise, T., J. M. Flores, and Y. Rudich. 2015. Optical prop- erties of secondary organic aerosols and their changes by chemical processes. Chem. Rev. 115:4400–39. doi:10.1021/ cr5005259.

Mukai, H., and Y. Ambe. 1986. Characterization of a Humic Acid-like Brown Substance in Airborne Particulate Matter and Tentative Identification of Its Origin. *Atmospheric Environment* 20 (5): 813–19.

Nakayama, T., K. Sato, Y. Matsumi, T. Imamura, A. Yamazaki, and A. Uchiyama. 2013. Wavelength and NOx Dependent Complex Refractive Index of SOAs Generated from the Photooxidation of Toluene. *Atmos. Chem. Phys.* 13: 531–45. doi.org/10.5194/acp-13-531-2013.

Olson, M. R., M. V. Garcia, M. A. Robinson, P. Van Rooy, M. A. Dietenberger, M. Bergin, and J. J. Schauer. 2015. Investigation of Black and Brown Carbon Multiple-Wavelength-Dependent Light Absorption from Biomass and Fossil Fuel Combustion Source Emissions. *J. Geophys. Res. Atmos* 120: 6682–97. doi.org/10.1002/2014JD022970.Received.

Onasch, T. B., E. C. Fortner, A. M. Trimborn, A. T. Lambe, A. J. Tiwari, L. C. Marr, J. C. Corbin, et al. 2015. Investigations of SP-AMS Carbon Ion Distributions as a Function of Refractory Black Carbon Particle Type Investigations of SP-AMS Carbon Ion Distributions as a Function of Refractory Black Carbon Particle Type. *Aerosol Science and Technology* 49 (6): 409–22. doi.org/10.1080/02786826.2015.1039959.

Onasch, T. B., A. Trimborn, E. C. Fortner, J. T. Jayne, G. L. Kok, L. R. Williams, P. Davidovits, and D. R. Worsnop. 2012. Soot Particle Aerosol Mass Spectrometer: Development, Validation, and Initial Application. *Aerosol Science and Technology* 46:7: 804–17. doi.org/10.1080/02786826.2012.663948.

Phillips, S. M., and G. D. Smith. 2014. Light Absorption by Charge Transfer Complexes in Brown

Carbon Aerosols. *Environ. Sci. Technol. Lett.* 1 (10): 382–86. doi.org/10.1021/ez500263j.

Posfai, M., A. Gelencser, R. Simonics, K. Arato, J. Li, P. V. Hobbs, and P. R. Buseck. 2004. Atmospheric Tar Balls: Particles from Biomass and Biofuel Burning. *J. Geophys. Res.* 109: D06213. doi.org/10.1029/2003JD004169.

Saleh, R., Z. Cheng, and K. Atwi. 2018. The Brown–Black Continuum of Light-Absorbing Combustion Aerosols. Rapid-communication. *Environ. Sci. Technol. Lett.* 5: 508–13. doi.org/10.1021/acs.estlett.8b00305.

Saleh, R., M. Marks, J. Heo, P. J. Adams, N. M. Donahue, and A. L. Robinson. 2015. Contribution of Brown Carbon and Lensing to the Direct Radiative Effect of Carbonaceous Aerosols from Biomass and Biofuel Burning Emissions. *J. Geophys. Res. Atmos* 120 (10): 10,285–10,296. doi.org/10.1002/ 2015JD023697.

Saleh, R., E. S. Robinson, D. S. Tkacik, A. T. Ahern, S. Liu, A. C. Aiken, R. C. Sullivan, et al. 2014. Brownness of Organics in Aerosols from Biomass Burning Linked to Their Black Carbon Content. *Nature Geoscience* 7 (9): 647–50. doi.org/10.1038/ngeo2220.

Sarkar, C., C. Venkataraman, S. Yadav, and H. C. Phuleria. 2019. Origin and Properties of Soluble Brown Carbon in Freshly Emitted and Aged Ambient Aerosols over an Urban Site in India. *Environmental Pollution* 254: 113077. doi.org/10.1016/j.envpol.2019.113077.

Sasaki, J., S. M. Aschmann, E. S. C. Kwok, R. Atkinson, and J. Arey. 1997. Products of the Gas-Phase OH and $NO_3$ Radical-Initiated Reactions of Naphthalene. *Environ. Sci. Technol.* 31 (3): 3173–79. doi.org/10.1021/es9701523.

Satish, R., P. Shamjad, N. Thamban, S. Tripathi, and N. Rastogi. 2017. Temporal Characteristics of Brown Carbon over the Central Indo- Gangetic Plain. *Environ. Sci. Technol.* 51: 6765−6772. doi.org/10.1021/acs.est.7b00734.

Sedlacek III, A. J., P. R. Buseck, K. Adachi, T. B. Onasch, S. R. Springston, and L. Kleinman. 2018. Formation and Evolution of Tar Balls from Northwestern US Wildfires. *Atmos. Chem. Phys.* 18: 11289–301.

Shen, G., S. Tao, S. Wei, Y. Zhang, R. Wang, B. Wang, W. Li, et al. 2012. Emissions of Parent, Nitro, and Oxygenated Polycyclic Aromatic Hydrocarbons from Residential Wood Combustion in Rural China. *Environ. Sci. Technol.* 46: 8123−8130. doi.org/10.1021/es301146v.

Sumlin, B. J., A. Pandey, M. J. Walker, R. S. Pattison, B. J. Williams, and R. K. Chakrabarty. 2017. Atmospheric Photooxidation Diminishes Light Absorption by Primary Brown Carbon Aerosol from Biomass Burning. *Environ. Sci. Technol. Lett* 4: 540−545. doi.org/10.1021/acs.estlett.7b00393.

Tóth, A., A. Hoffer, I. Nyiro-Kósa, M. Pósfai, and A. Gelencsér. 2014. Atmospheric Tar Balls: Aged Primary Droplets from Biomass Burning? *Atmos. Chem. Phys.* 14 (13): 6669–75. doi.org/10.5194/acp-14-6669-2014.

Utry, N., T. Ajtai, ágnes Filep, M. Dániel Pintér, A. Hoffer, Z. Bozoki, and G. Szabó. 2013. Mass Specific Optical Absorption Coefficient of HULIS Aerosol Measured by a Four-Wavelength Photoacoustic Spectrometer at NIR, VIS and UV Wavelengths. *Atmospheric Environment* 69: 321–24. doi.org/10.1016/j.atmosenv.2013.01.003.

Wang, L., Z. Li, Q. Tian, Y. Ma, F. Zhang, Y. Zhang, D. Li, K. Li, and L. Li. 2013. Estimate of Aerosol Absorbing Components of Black Carbon, Brown Carbon, and Dust from Ground-Based Remote Sensing Data of Sun-Sky Radiometers. *J. Geophys. Res.* 118 (12): 6534–43. doi.org/10.1002/jgrd.50356.

Wang, X., C. L. Heald, D. A. Ridley, J. P. Schwarz, J. R. Spackman, A. E. Perring, H. Coe, and D. Liu. 2014. Exploiting Simultaneous Observational Constraints on Mass and Absorption to Estimate the Global Direct Radiative Forcing of Black Carbon and Brown Carbon. *Atmos. Chem. Phys.* 14: 10989–10. doi.org/10.5194/acp-14-10989-2014.

Wang, X., C. L. Heald, A. J. Sedlacek, S. S. De Sá, S. T. Martin, M. L. Alexander, T. B. Watson, A. C. Aiken, S. R. Springston, and P. Artaxo. 2016. Deriving Brown Carbon from Multiwavelength Absorption Measurements: Method and Application to AERONET and Aethalometer Observations. *Atmos. Chem. Phys.* 16: 12733–52. doi.org/10.5194/acp-16-12733-2016.

Wang, Y., P. L. Ma, J. Peng, R. Zhang, J. H. Jiang, R. C. Easter, and Y. L. Yung. 2018. Constraining Aging Processes of Black Carbon in the Community Atmosphere Model Using Environmental Chamber Measurements. *Journal of Advances in Modeling Earth Systems* 10 (10): 2514–26. doi.org/10.1029/2018MS001387.

Wang, Y., M. Hu, P. Lin, T. Tan, M. Li, N. Xu, J. Zheng, et al. 2019. Enhancement in Particulate Organic Nitrogen and Light Absorption of Humic-Like Substances over Tibetan Plateau Due to Long-Range Transported Biomass Burning Emissions. Research-article. *Environ. Sci. Technol.* 53: 14222–32. doi.org/10.1021/acs.est.9b06152.

Wong, J. P. S., A. Nenes, and R. J. Weber. 2017. Changes in Light Absorptivity of Molecular Weight Separated Brown Carbon Due to Photolytic Aging. *Environ. Sci. Technol.* 51: 8414−8421. doi.org/10.1021/acs.est.7b01739.

Wong, J. P. S., M. Tsagkaraki, I. Tsiodra, N. Mihalopoulos, K. Violaki, M. Kanakidou, J. Sciare, A. Nenes, and R. J. Weber. 2019. Atmospheric Evolution of Molecular-Weight-Separated Brown Carbon from Biomass Burning. *Atmos. Chem. Phys.* 19: 7319–34.

You, R., J. G. Radney, M. R. Zachariah, and C. D. Zangmeister. 2016. Measured Wavelength-Dependent Absorption Enhancement of Internally Mixed Black Carbon with Absorbing and Nonabsorbing Materials. *Environ Sci Technol.* 50 (15): 7982–90. doi.org/10.1021/acs.est.6b01473.Measured.

Yu, Z., G. Magoon, J. Assif, W. Brown, and R. Miake-Lye. 2019. A Single-Pass RGB Differential Photoacoustic Spectrometer (RGB-DPAS) for Aerosol Absorption Measurement at 473, 532, and 671 Nm. *Aerosol Science and Technology* 53 (1): 94–105. doi.org/10.1080/02786826.2018.1551611.

Zhang, Y., J. Shu, C. Liu, Y. Zhang, B. Yang, and J. Gan. 2013. Heterogeneous Reaction of Particle-Associated Triphenylene with $NO_3$ Radicals. *Atmospheric Environment* 68 (3): 114–19. doi.org/10.1016/j.atmosenv.2012.11.052.

Zhang, Y., H. Forrister, J. Liu, J. Dibb, B. Anderson, J. P. Schwarz, A. E. Perring, et al. 2017. Top-of-Atmosphere Radiative Forcing Affected by Brown Carbon in the Upper Troposphere. *Nature Geoscience* 10: 486. doi.org/10.1038/NGEO2960.

Zhao, R., A. K. Y. Lee, L. Huang, X. Li, F. Yang, and J. P. D. Abbatt. 2015. Photochemical Processing of Aqueous Atmospheric Brown Carbon. *Atmos. Chem. Phys.* 15: 6087–6100. doi.org/10.5194/acp-15-6087-2015.

Zhong, M., and M. Jang. 2014. Dynamic Light Absorption of Biomass-Burning Organic Carbon Photochemically Aged under Natural Sunlight. *Atmos. Chem. Phys.* 14: 1517–25. doi.org/10.5194/acp-14-1517-2014.

Zielinska, B., J. Arey, R. Atkinson, and P. A. McElroy. 1989. Formation of Methylnitronaphthalenes from the Gas-Phase Reactions of 1- and 2-Methylnaphthalene with OH Radicals and N205 and Their Occurrence in Ambient Air. *Environ. Sci. Technol.* 23 (6): 723–29. doi.org/10.1021/es00064a011.

Zimmermann, K., N. Jariyasopit, S. L. M. Simonich, S. Tao, R. Atkinson, and J. Arey. 2013. Formation of Nitro-PAHs from the Heterogeneous Reaction of Ambient Particle-Bound PAHs with $N_2O_5/NO_3/NO_2$. *Environ. Sci. Technol. 2013,* 47 (3): 8434−8442. doi.org/10.1021/es401789x.

# CHAPTER 4

# DISCREPANCIES BETWEEN BRWON CARBON LIGHT-ABSORPTION PROPERTIES RETRIEVED USING ONLINE AND OFFLINE METHODS[3]

[3] Cheng, Z., K. M. Atwi, O.E. Hajj, I. Ijeli, D.A. Fischer, G. Smith, and R. Saleh. Submitted to Aerosol Science and Technology.

**Abstract**

We compared the imaginary part of the refractive indices (*k*) of brown carbon (BrC) retrieved from online and solvent-extraction offline light-absorption measurements. BrC with variable light-absorption properties was generated from the controlled combustion of three structurally different fuels: toluene (aromatic), isooctane (branched alkane), and cyclohexane (cyclic alkane). The online retrieval method involved combining real-time measurements of aerosol absorption coefficients (at 422 nm, 532 nm, and 781 nm) and size distributions with Mie calculations. The offline method involved extracting BrC samples with two organic solvents, methanol and dichloromethane, followed by light-absorption measurements of the extracts using a UV-vis spectrophotometer. For the least absorbing BrC, *k* values of the extracts in both solvents, retrieved using the offline method, were similar to those of the aerosol, retrieved using the online method. However, for darker BrC, *k* values of the BrC extracts in dichloromethane were smaller than those of the BrC aerosol, and *k* values of the BrC extracts in methanol were the smallest, with the discrepancy among the three increasing with increasing BrC darkness. These results indicate that BrC produced in this study was more soluble in dichloromethane than methanol, and the BrC solubility in both solvents decreased with increasing BrC darkness. Finally, *k* of BrC produced from all fuels, for both BrC aerosol and extracts, followed the same trend of decreasing wavelength dependence (flatter absorption spectra) with increasing *k* as previous data, further supporting the brown-black continuum of light-absorption properties.

## 4.1. Introduction

Light-absorbing organic aerosol (OA), or brown carbon (BrC), absorbs incoming solar radiation in the visible and ultra-violet wavelengths (Andreae and Gelencsér 2006). BrC absorption has an important yet uncertain effect on atmospheric radiative balance, with estimates of its global radiative effect ranging over an order of magnitude, between +0.03 W/m$^2$ and +0.57 W/m$^2$ (Saleh 2020). This large uncertainty is in part a result of persistent gaps in the fundamental understanding of the BrC chemical composition and optical properties. BrC absorption has been linked to various species including polycyclic aromatic hydrocarbons (PAHs) (Saleh et al. 2018; Cheng et al. 2020; Adler et al. 2019), oxygenated and nitrated aromatics (Li, He, Hettiyadura, et al. 2019; Li, He, Schade, et al. 2019; Liu et al. 2016; Liu et al. 2017; Desyaterik et al. 2013; Cheng et al. 2020), nitrogen heterocyclic compounds (Kampf et al. 2016; Marrero-Ortiz et al. 2019), as well as interaction of chromophores with charge transfer complexes (Phillips and Smith 2014, 2015). The diversity in BrC chromophores is manifested as a wide variability in BrC light-absorption properties, which can be quantified using the wavelength-dependent imaginary part of the refractive index ($k$). BrC absorption spectra exhibit an increase toward short-visible and UV wavelengths (Laskin, Laskin, and Nizkorodov 2015; Moise, Flores, and Rudich 2015), which can be mathematically represented with a power-law functional dependence on wavelength (i.e., $k(\lambda) \sim \lambda^{-w}$). Based on a compilation of light-absorption data of BrC from various sources reported in the literature, Saleh (2020) proposed an optical classification of BrC based on its $k$ at 550 nm ($k_{550}$) and $w$: very weakly absorbing BrC (VW-BrC) ($k_{550}$=$10^{-4}$-$10^{-3}$, $w$=6-9), weakly absorbing BrC (W-BrC) ($k_{550}$ = $10^{-3}$-$10^{-2}$, $w$ = 4-7), moderately absorbing BrC (M-BrC) ($k_{550}$ = $10^{-2}$-$10^{-1}$, $w$ = 1.5-4), and strongly absorbing BrC (S-BrC) ($k_{550} > 10^{-1}$, $w$ = 0.5-1.5). It is noteworthy that $k_{550}$ of VW-BrC and S-BrC are separated by 3 orders of magnitude and that the more absorptive BrC (larger

$k_{550}$) is characterized by flatter absorption spectra (smaller $w$). Furthermore, there is a correlation between BrC sources and optical classes, with the more absorptive BrC (M-BrC and S-BrC) mostly associated with biomass combustion.

In addition to the true variability outlined above, discrepancies between BrC light-absorption properties reported in the literature arise from differences in measurement techniques and the associated biases and uncertainties. Retrieval of $k$ and $w$ of BrC can be achieved via online aerosol optical measurements coupled with optical (e.g., Mie theory) calculations (Chakrabarty et al. 2010; Saleh et al. 2013; Saleh et al. 2014; Lack et al. 2012) or offline methods involving filter collection and extraction with water or organic solvents followed by light-absorption measurements using ultraviolet-visible (UV-vis) spectrophotometry (Chen and Bond 2010; Li, Chen, and Bond 2016). The main advantage of the online methods is the ability to retrieve the optical properties of the BrC aerosol while airborne. However, the retrieval process is relatively complex. The presence of BC, which is often co-emitted with BrC, induces relatively large uncertainty because retrieval calculations require knowledge of the poorly constrained BC mixing state and morphology (Saleh 2020; Stevens and Dastoor 2019). Since BC is insoluble in water and organic solvents (Bond et al. 2013), the offline methods have the advantage of isolating the BrC via solvent extraction. However, not all types of BrC are efficiently extracted in water and organic solvents (Corbin et al. 2019). Different types of BrC exhibit variable extraction efficiencies in different solvents, leading to retrieved light-absorption properties that are solvent-dependent (Chen and Bond 2010; Liu et al. 2013; Shetty et al. 2019).

Traditionally, the most widely used solvent to extract organic aerosol (OA) in atmospheric science research is water (Hecobian et al. 2010; Claeys et al. 2012; Zhang et al. 2013). Realizing that a

significant fraction of OA is not water soluble, methanol has also been used as a solvent in more recent studies (Fuzzi and Decesari 2016; Xie et al. 2017; Xie, Hays, and Holder 2017; Phillips and Smith 2017). Methanol has been shown to be more effective at extracting OA in fresh combustion emissions (Chen and Bond 2010; Sengupta et al. 2018), which are relatively non-polar. Consequently, for the same combustion emissions, *k* values retrieved for methanol-extracted BrC are larger than those for water-extracted BrC (Chen and Bond 2010; Wu et al. 2016). Although relatively uncommon in atmospheric aerosol studies, dichloromethane (DCM) is frequently used as a solvent in combustion soot-formation research due to its efficacy at extracting the large-molecular-size polycyclic aromatic hydrocarbons (PAHs) that constitute nascent soot (Alfè et al. 2008; Apicella et al. 2007; Russo et al. 2013), which are important BrC components (Saleh et al. 2018; Cheng et al. 2020). BrC absorption (i.e., *k*) increases with increasing molecular size (Saleh et al. 2018) while its solubility decreases with increasing molecular size (Corbin et al. 2019). Therefore, offline solvent-extraction techniques are expected to underestimate BrC absorption as they miss the large-molecular-size S-BrC (Saleh 2020), which is poorly soluble or insoluble in organic solvents (Corbin et al. 2019). This is supported by the findings of Shetty et al. (2019) who reported that the extraction efficiency of biomass-burning BrC decreased with the increasing of BC/OA ratio, which is correlated with an increase in production of S-BrC (Cheng et al. 2019; Saleh 2020; Saleh et al. 2014).

In this study, we investigated the discrepancies in BrC light-absorption properties that arise from retrieval methods (online versus offline) and the choice of solvent in offline methods. We produced BrC with variable light-absorption properties from the controlled combustion of three structurally different fuels: toluene (aromatic), isooctane (branched alkane), and cyclohexane (cyclic alkane).

We compared the BrC light-absorption properties retrieved from online measurements to those retrieved from offline solvent-extraction measurements using methanol and DCM as solvents.

## 4.2. Methods

### 4.2.1. Approach

We performed a systematic comparison between the light-absorption properties (*k* and *w*) of BrC retrieved from online light-absorption and aerosol size-distribution measurements and those retrieved from solvent-extraction followed by offline UV-vis spectrophotometry. We isolated three key effects:

1) Light-absorption properties of the suspended BrC particles: There is an association between BrC light-absorption properties and its physicochemical properties, such as solubility in organic solvents (Saleh 2020; Corbin et al. 2019). Therefore, it is important to assess the dependence of solvent-extraction bias on BrC light-absorption properties. To this effect, we generated BrC with variable *k* values that span the range observed for combustion BrC, including weakly absorbing BrC (W-BrC), moderately absorbing BrC (M-BrC), and strongly absorbing BrC (S-BrC) (Saleh 2020).

2) Fuel type: We used three structurally different fuels: toluene (aromatic), isooctane (branched alkane), and cyclohexane (cyclic alkane). For each fuel, we generated BrC spanning the optical classes described above and compared the solvent-extraction bias for BrC within the same optical class but produced from the different fuels.

3) Solvent type: We used two organic solvents: methanol and DCM. Methanol is recently becoming the most used organic solvent in atmospheric aerosol research and is often assumed to extract most or all of the OA, including BrC (Fuzzi and Decesari 2016; Sengupta et al. 2018; Xie, Hays, and Holder 2017; Cheng et al. 2016; Liu et al. 2013). On the other hand, DCM is commonly used in studies of organic nascent soot formation in combustion (Alfè et al. 2008; Apicella et al. 2007; Russo et al. 2013) due to its efficacy at extracting the PAHs that comprise the nascent soot. We have previously shown that these PAHs constitute an important fraction of combustion BrC (Saleh et al. 2018); therefore, DCM can potentially be an appropriate solvent for atmospheric BrC research.

Details of the combustion experiments and the online and offline techniques employed to retrieved *k* and *w* of the generated BrC are described in the subsequent subsections.

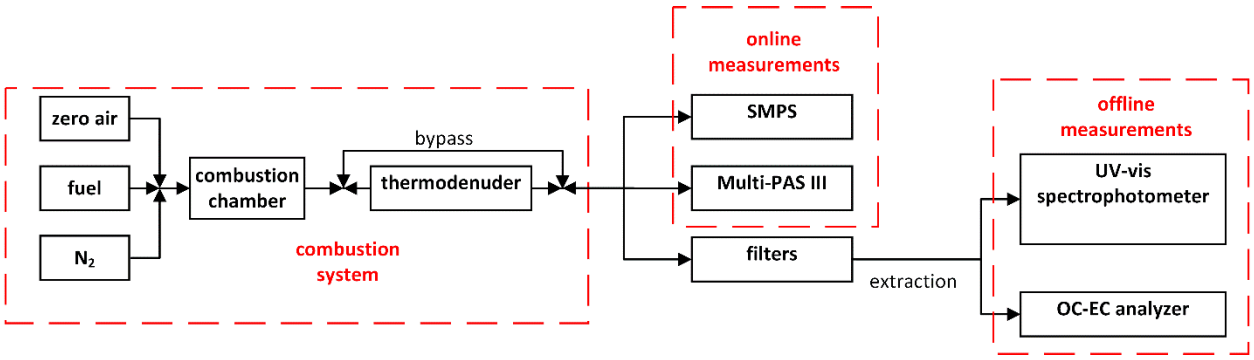


**Figure 4.1.** Schematic of the experimental setup.

### 4.2.2. Combustion experiments and online measurements

The combustion system utilized in this study is described in detail in Cheng et al. (2019). Briefly, controlled steady flows of fuel, clean air, and additional nitrogen (used as a passive diluent) were introduced into a temperature-controlled quartz combustion chamber. The temperature of the

combustion chamber was controlled at either 950 °C or 1000 °C in these experiments. The fuel was introduced in vapor form using a bubbler at a flowrate dictated by the saturation vapor pressure of the fuel (3.4, 5.3, and 10.7 kPa for toluene, cyclohexane, and isooctane, respectively). The equivalence ratios in the experiments ranged between 1.1 and 4.7, and the nitrogen/oxygen ratio ranged between 1.9 and 80.5. By tuning the combustion conditions, we generated BrC with widely variable and well-controlled optical properties. In specific, increasing the combustion temperature, decreasing the equivalence ratio, and/or decreasing the nitrogen/oxygen ratio produces darker BrC (larger *k* and smaller *w*) (Saleh et al. 2018). In two experiments (one for cyclohexane and one for isooctane), dark BrC was further isolated by passing the emissions through a thermodenuder controlled at 120 ˚C. This process relies on the established association between volatility and BrC optical properties, namely that the residual (less volatile) fraction is darker than the evaporated (more volatile) fraction (Saleh et al. 2018, Saleh 2020). Details of the combustion conditions for each experiment are given in Table S4.1 in the Supplementary Information (SI).

In order to tune the combustion conditions to produce BrC of certain desired light-absorption properties, we relied on real-time calculations of the wavelength-dependent mass absorption cross-section (MAC, $m^2\ g^{-1}$) and absorption Ångström exponent (AAE). Those could be readily obtained from the real-time measurements of the absorption coefficients ($b_{abs}$, $Mm^{-1}$) and total aerosol mass concentrations ($m_p$):

$$\mathrm{MAC}(\lambda) = b_{abs}(\lambda)/m_p \qquad (4.1)$$

AAE was obtained by fitting a power-law function to Equation (4.1). We measured $b_{abs}$ at $\lambda$ = 422, 532, and 781 nm using a 3-wavelength Multi-pass Photoacoustic Spectrophotometer Spectrometer (Multi-PAS III) (Fischer and Smith 2018). $m_p$ was calculated by integrating the size distribution

within the size range 10–550 nm measured using a scanning mobility particle sizer (SMPS, TSI) with a density value of 1.2 g $cm^{-3}$, which was measured using the tandem differential mobility analyzer – aerosol particle mass analyzer (tandem DMA-APM) technique (Malloy et al. 2009). We classified the aerosols based on their electricity mobility diameter ($d_m$) using a differential mobility analyzer (DMA, TSI) and then measured the mass of the selected particles ($m$) using an aerosol particle mass (APM, Kanomax) analyzer. The mobility effective density ($\rho_{eff}$) was calculated as (McMurry et al. 2002):

$$\rho_{eff} = \frac{m}{\frac{\pi d_m^3}{6}} \quad (4.2)$$

We have previously confirmed that BrC particles formed at similar conditions were near-spherical particles based on scanning electron microscopy (SEM) images (Saleh et al. 2018). Thus, the mobility-equivalent volume of BrC particles in Equation (4.2) is equal to the true volume of the particles and $\rho_{eff}$ measured by the tandem DMA-APM technique is equal to the true density.

For each experiment, we processed the light-absorption (Multi-PAS III) and size-distribution (SMPS) data to retrieve the BrC $k$ at 422 nm, 532 nm, and 781 nm using optical closure (Saleh et al. 2018). The procedure involved optimizing a Mie code to reproduce the measured $b_{abs}$ at each wavelength using the size distribution as input and $k$ as a free parameter. We assumed a real part of the refractive index of 1.6 in the calculations (Saleh 2020). We then calculated $w$ as the exponent of a power-law fit to the retrieved $k$ values versus wavelengths. Hereafter, we refer to the $k$ and $w$ values retrieved for the airborne particles as $k_{aerosol}$ and $w_{aerosol}$ to distinguish them from the $k$ and $w$ values retrieved from UV-vis measurements of extracts ($k_{extracts}$ and $w_{extracts}$).

### 4.2.3 Filter collection and extraction

For each experiment, we collected BrC samples at a flow rate of 10 lpm on 47 mm polytetrafluoroethylene (PTFE, Teflon) filters (Whatman, TE 35, 0.2 µm pore size). To ensure we had enough BrC for clear UV-vis signals, we collected ~0.75 mg of BrC under each combustion condition, requiring approximately 3 hours of sampling time per condition. The combustion conditions and BrC optical properties were uniform during the sampling time, which is one of the main advantages of the combustion system employed in this study. In preliminary experiments, we noticed that the filters start clogging when loadings exceed ~0.3 mg. Thus, for each experiment, we collected three filters, each with a loading of ~0.25 mg.

The filter extraction procedure was similar to Hecobian et al. (2010) and Phillips and Smith (2017). We divided each of the three filters into two pieces and sonicated one piece of each filter in a glass vial (Fisherbrand, 03-339-22F) for 20 minutes with 10 ml of either methanol (Macron fine chemicals, 3016-16, ≥ 99.8% purity) or DCM (SIGMA-ALDRICH, 270997-2L, ≥ 99.8% purity). Preliminary experiments showed that sonication for longer than 20 minutes did not affect the results. After sonication, we filtered the solution using 0.2 µm PTFE filters (STERLITECH Corporation, PTU021350, 13 mm diameter) to remove undissolved particles, which cause bias in the UV-vis absorption measurements due to scattering (Phillips and Smith 2017).

We estimated the BrC concentration in the solution ($C_{BrC}$) following a procedure similar to Li, Chen, and Bond (2016). We pipetted 300 µl from each solution using silicon-coated tips onto a blank prebaked 1.5 $cm^2$ quartz filter punch (Pall Inc., Tissuquartz 2500). We then evaporated the solvent using a 10 lpm stream of clean, dry air for 10 minutes. The BrC is orders of magnitude less volatile than the solvents, and therefore the amount of BrC evaporated in this procedure is

negligible. The total mass of carbon on the filter punches ($m_{TC}$) was measured using an OC-EC analyzer (Sunset Laboratory Inc, Portland, OR, USA, Model 5L), and $C_{BrC}$ was calculated as $m_{TC}$ divided by the pipetted solution volume (300 µl). To validate the accuracy of this method, we prepared solutions with known concentrations of pyrene in DCM and methanol and were able to retrieve the concentrations with less than 7% error (see Table S4.2 in SI). With the absence of information on the elemental composition of the BrC, we assumed that the BrC concentration was equal to the carbon concentration. Based on previous chemical speciation measurements of BrC produced under similar conditions (Cheng et al. 2020), we expect OA/OC (or BrC/OC) to be close to 1 for the lightest BrC samples and less than 1.4 for the darkest BrC samples (Section 3.2).

It is important to note that control experiments that involved quantifying $m_{TC}$ in solutions of extracted clean filters revealed that both methanol and DCM dissolved plastics (e.g., Polyvinyl chloride (PVC), polycarbonate (PC), polyethylene (PE)), which showed as an OC signal on the OCEC analyzer. To minimize the contact of the solvents with plastic, we used either metal or glass tools/containers in the extraction process and covered each vial with aluminum foil before sealing with the PVC cap. We verified that none of the tools/containers used in this extraction process caused any bias in the measured $C_{BrC}$ (see SI). However, DCM still dissolved organic matter in the PTFE filters leading to ~ 0.026 g/l bias in $C_{BrC}$ (see SI). Therefore, $C_{BrC}$ in the DCM solutions was corrected by subtracting 0.026 g/l from the measured concentrations. We verified that the dissolved organic matter from the filters did not exhibit any UV-vis absorption.

#### 4.2.4. Retrieving light-absorption properties of BrC extracts

The UV-vis absorbance (A) of the BrC extracts was measured in the range 200 nm to 800 nm at a 1 nm resolution using a UV-vis Spectrophotometer (Agilent, Cary 60). We retrieved the

wavelength-dependent imaginary part of the refractive index of the extracts ($k_{extracts}$) from the measured absorbance following the method of Sun et al. (2007). $k_{extracts}$ is related to the absorption coefficient of the BrC extracts (α, $cm^{-1}$):

$$k_{\text{extracts}}(\lambda) = \frac{\lambda}{4\pi}\alpha(\lambda) \quad (4.3)$$

Note that even though α and $b_{abs}$ have the same dimensions ($L^{-1}$), they have different physical meanings and should not be confused. While α is a material property, as evident in Equation (4.3), $b_{abs}$ represents the total absorption cross-section of an aerosol per unit volume of air and therefore depends on the aerosol concentration. α is obtained from absorbance measurements as:

$$\alpha(\lambda) = ln10\ \frac{A(\lambda)\rho}{C_{\text{BrC}}\ L} \quad (4.4)$$

Where $L$ is the optical path length (1 cm), $C_{BrC}$ is the concentration of BrC extracts (Section 2.3), and $\rho$ is the density of the extracted BrC, assumed to be 1.2 g $cm^{-3}$ (the density we obtained for the suspended aerosol; Section 4.2.2). The derivation of Equations (4.3) and (4.4) are given in the SI.

The wavelength dependence of $k_{exctracts}$ ($w_{extracts}$) was obtained as the exponent of a power-law fit of $k_{exctracts}$ versus wavelength. For direct comparison between $w_{aerosol}$ and $w_{extracts}$, the fit was limited to the wavelength range of the Multi-PAS III (422 nm – 781 nm). Note that since α is proportional to $k_{extracts}(\lambda)$ (Equation 4.3) and the wavelength dependence of α is AAE, it follows that $AAE_{extracts}$ = $w_{exrtacts}$ + 1, which is the expected relation for the small-particle limit. Furthermore, unlike $k_{extracts}$, the retrieval of $w_{extracts}$ is independent of $\rho$ and $C_{BrC}$ and is thus not subject to the biases associated with the assumptions outlined above.

### 4.2.5. Validation of the online and offline methods using nigrosin

In order to quantify the bias in $k_{exrtacts}$ and $w_{extracts}$ associated with extraction efficiency, we need first to assess any inconsistency between the online (aerosol) and offline (extracts) retrieval methods that is not associated with extraction efficiency. To that effect, we compared $k_{aerosol}$ and $k_{extracts}$ of nigrosin (Sigma Aldrich, CAS# 8005-03-6), a water-soluble organic dye. Nigrosin has been widely used as a model material of light-absorbing aerosol to validate PAS measurements (Lack et al. 2006; Wiegand, Mathews, and Smith 2014; Bluvshtein et al. 2017). We prepared an aqueous solution of nigrosin and used a constant output atomizer (TSI 3076) followed by diffusion drying to generate nigrosin aerosol. We retrieved $k_{aerosol}$ following the procedure described in Section 4.2.2 using a real part of the refractive index of 1.7 (Dinar et al. 2007). We retrieved $k_{extracts}$ following the procedure described in Section 4.2.4 using a density of 1.5 g $cm^{-3}$, which was obtained using the tandem DMA-APM technique.

## 4.3. Results and discussion

### 4.3.1. Light-absorption properties of nigrosin

Figure 4.2 shows $k_{extracts}$ as a function of wavelength between 400 nm and 800 nm and $k_{aerosol}$ at 422 nm, 532 nm, and 781 nm. Both online and offline retrievals show that $k$ of nigrosin exhibits a peak in the mid-visible wavelengths and drops to smaller values towards the long-visible and short-visible wavelengths. This wavelength dependence of $k$ is consistent with nigrosin's dark "midnight purple" appearance. At 532 nm, $k_{aerosol}$ and $k_{extracts}$ are 0.282 ± 0.009 and 0.270 ± 0.004, respectively, which are in good agreement, and within the range reported in the literature (Dinar et al. 2007; Garvey and Pinnick 1983; Bluvshtein et al. 2012; Lang-Yona et al. 2009; Bluvshtein

et al. 2017) (Figure 4.2). The differences are larger at 422 nm ($k_{aerosol}$ = 0.165 ± 0.004, $k_{extracts}$ = 0.132 ± 0.004) and 781 nm ($k_{aerosol}$ = 0.1894 ± 0.011, $k_{extracts}$ = 0.161 ± 0.002). Nevertheless, these results indicate that the light absorption properties obtained using online and offline methods are consistent, and any significant differences (> ~20%) in $k_{aerosol}$ and $k_{extracts}$ of BrC could be attributed to extraction efficiency.

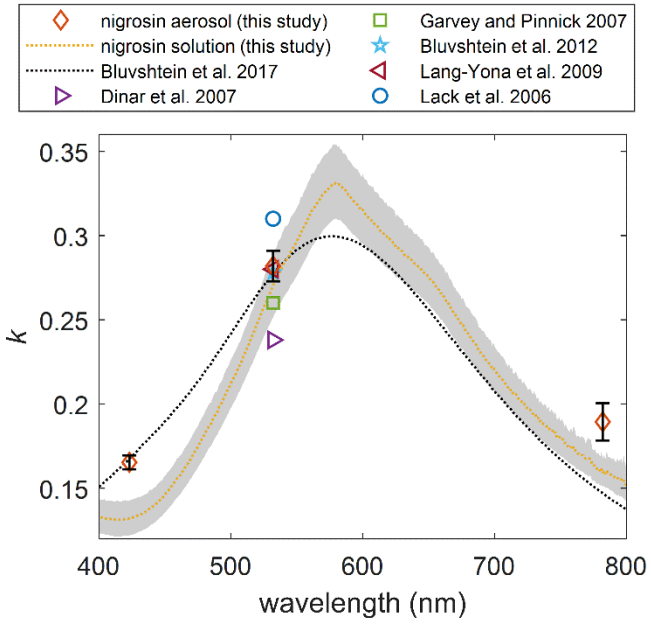


**Figure 4.2.** Imaginary part of the refractive index ($k$) of nigrosin retrieved from online and offline measurements. The range of the shaded area is the uncertainty of UV-vis measurements (~5%), which is a combination of the variances of the absorption measurements and uncertainty in the concentration measurements (see uncertainty analysis in SI).

### 4.3.2 Comparison of the light-absorption properties of BrC aerosol and extracts

The BrC generated from the controlled combustion of toluene, cyclohexane, and isooctane had $k_{aerosol}$ at 532 nm ($k_{aerosol,532}$) values ranging over approximately two orders of magnitude (0.005 to

0.127). These values cover the range for combustion BrC reported in the literature, and fall under the weakly absorbing (W-BrC), moderately absorbing (M-BrC), and strongly absorbing (S-BrC) optical-based classes introduced by Saleh (2020). $w_{aerosol}$ and $k_{aerosol,532}$ exhibit an inverse relation, where darker BrC is characterized by larger $k_{aerosol,532}$ and smaller $w_{aerosol}$ (Saleh et al. 2018). The corresponding $w_{aerosol}$ ranged between 3.0 and 9.2 for the darkest and lightest BrC, respectively. The numerical values of $k_{aerosol}$ and $w_{aerosol}$ from all experiments are given in Table S4.1 in the SI.

The BrC concentrations ($C_{BrC}$) and UV-vis absorbance of BrC extracts in the two solvents are plotted against $k_{aerosol,532}$ in Figure 4.3. As shown in Figure 4.3a, with the exception of the lightest BrC sample (smallest $k_{aerosol,532}$), $C_{BrC}$ of the DCM extracts was larger than $C_{BrC}$ of the methanol extracts, indicating that DCM had a better extraction efficiency than methanol based on carbon mass. The significance of the difference in extraction efficiency between the two solvents is more evident in Figure 4.3b, which shows relatively close absorbances of DCM and methanol extracts for the light BrC samples (small $k_{aerosol,532}$) but a significantly steeper increase in the absorbance of DCM extracts with increasing $k_{aerosol,532}$ compared to methanol extracts. Absorbance is a consequence of both abundance (i.e., $C_{BrC}$) and intrinsic absorption (i.e., $k$), as evident in Equation (4.3) and Equation (4.4). Therefore, these results indicate that for the same BrC aerosol, the DCM extracts did not only have higher BrC mass concentrations, but the BrC in DCM extracts was also more absorbing (darker) than the BrC in methanol extracts. We note that since the DCM extracts are darker and are thus expected to exhibit larger molecular sizes than methanol extracts (Saleh, Cheng, and Atwi 2018), the better carbon-mass-based extraction efficiency of DCM might not necessarily translate to better extraction efficiency in terms of number of molecules.

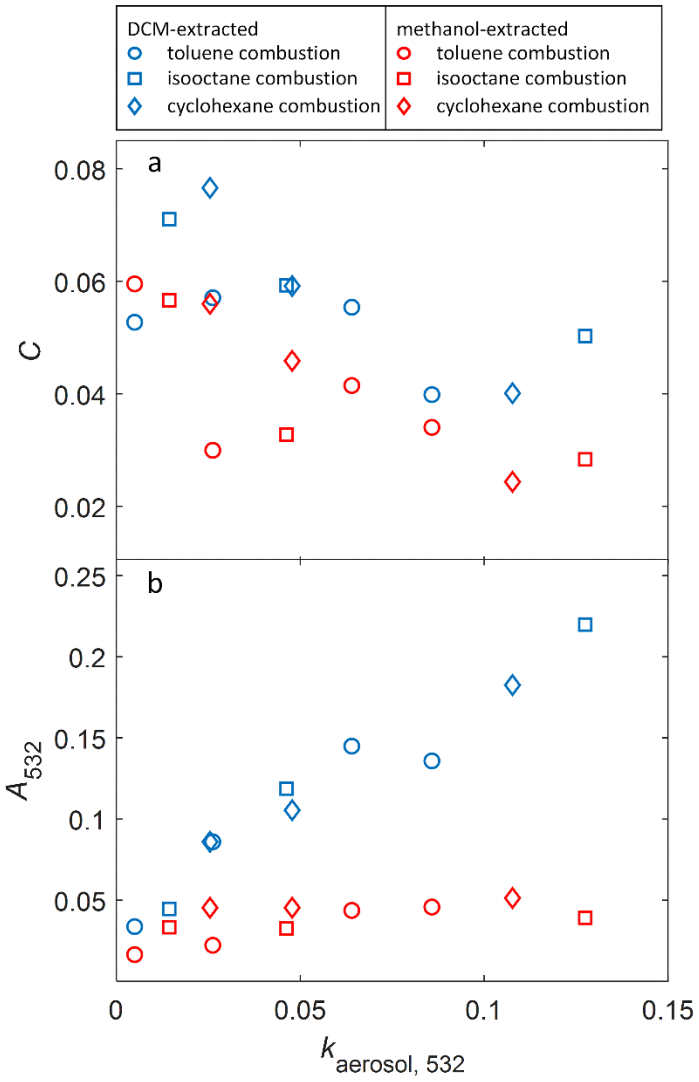


**Figure 4.3.** Comparisons of (a) concentrations ($C_{BrC}$) and (b) absorbance at 532 nm ($A_{532}$) of DCM-extracted and methanol-extracted BrC as a function of the imaginary part of the refractive index of BrC aerosol at 532 nm $k_{aerosol,532}$. BrC was generated from the combustion of toluene, cyclohexane, and isooctane.

This is further illustrated in Figure 4.4, which depicts $k_{extracts,532}$ and $w_{extracts}$ obtained from the offline solvent-extraction measurements using methanol and DCM plotted against $k_{aerosol,532}$ and $w_{aerosol}$. The numerical values of $k_{extracts,532}$ and $w_{extracts}$ from all experiments are given in Table S4.1

in the SI. We note that even though the combustion conditions are controlled in this study and the BrC produced at each condition is relatively uniform compared to real-life uncontrolled combustion, the BrC at each condition still comprises species with a continuum of molecular sizes and light-absorption properties. As evident in Figure 4.4, the DCM-extracted BrC was darker (larger $k_{extracts,532}$ and smaller $w_{extracts}$) than the methanol-extracted BrC, indicating that DCM was more efficient at extracting the larger-molecular-size, more light-absorbing fraction of the BrC. There is no apparent fuel dependence of the difference in light-absorption properties between methanol-extracted and DCM-extracted BrC, suggesting that there is no significant fuel dependence of the difference in extraction efficiency between methanol and DCM. These results indicate that DCM is a more potent solvent than methanol in extracting combustion BrC, particularly the darker fraction. Given that the absorbances (Figure 4.3) and light-absorption properties (Figure 4.4) of the DCM and methanol extracts are similar for W-BrC and diverge as BrC becomes darker, we expect the methanol extracts are a subset of DCM extracts. However, it is possible that some molecules are extracted by methanol and not DCM, in which case sequential extraction in both solvents would lead to better BrC quantification.

With the exception of the lightest BrC data point (Figure 4.4), the BrC from all fuels and combustion conditions had $k_{exrtacts} < k_{aerosol}$ and $w_{extracts} > w_{aerosol}$ for both solvents, signifying that, even with DCM, the extraction efficiency of each BrC sample was lower for the darker fraction of the sample. This is expected because, for some classes of molecules, solubility decreases with increasing molecular size (Corbin et al. 2019), while BrC absorption increases with molecular size (Saleh et al. 2018). These results are consistent with the findings of Shetty et al. (2019) who compared light absorption by biomass-burning BrC aerosol to light absorption by BrC extracts using water, methanol and acetone. They reported that, for all solvents, the ratio of extracts

absorption to aerosol absorption decreased with increasing BC/OA of the emissions, which is correlated with increasing BrC darkness (Saleh et al. 2014; Cheng et al. 2019; McClure et al. 2020).

In general, the results shown in Figure 4.4 show that solvent-extraction techniques can substantially underestimate BrC light absorption. For methanol-extracted BrC, $k_{\text{exctracts},532}$ was smaller than 0.025 and $w_{\text{extracts}}$ was larger than 7 for all samples, suggesting that the majority of methanol-extracted BrC was weakly absorbing (W-BrC). On the other hand, DCM also extracted a significant fraction of the moderately absorbing BrC (M-BrC), but the strongly absorbing BrC (S-BrC) remained largely unextracted. Real-life uncontrolled combustion (e.g., biomass burning) produces BrC components that exhibit wide distributions within different optical classes, with the fraction of components in each class being dependent on the general combustion regime. Smoldering combustion would feature more of the W-BrC class, while flaming combustion would feature more of the M-BrC and S-BrC classes (Saleh 2020). Therefore, as can be inferred from Figure 4.4, the bias in BrC light-absorption properties retrieved from solvent-extraction methods is expected to become more prominent as the combustion approaches flaming conditions and the emitted BrC becomes darker.

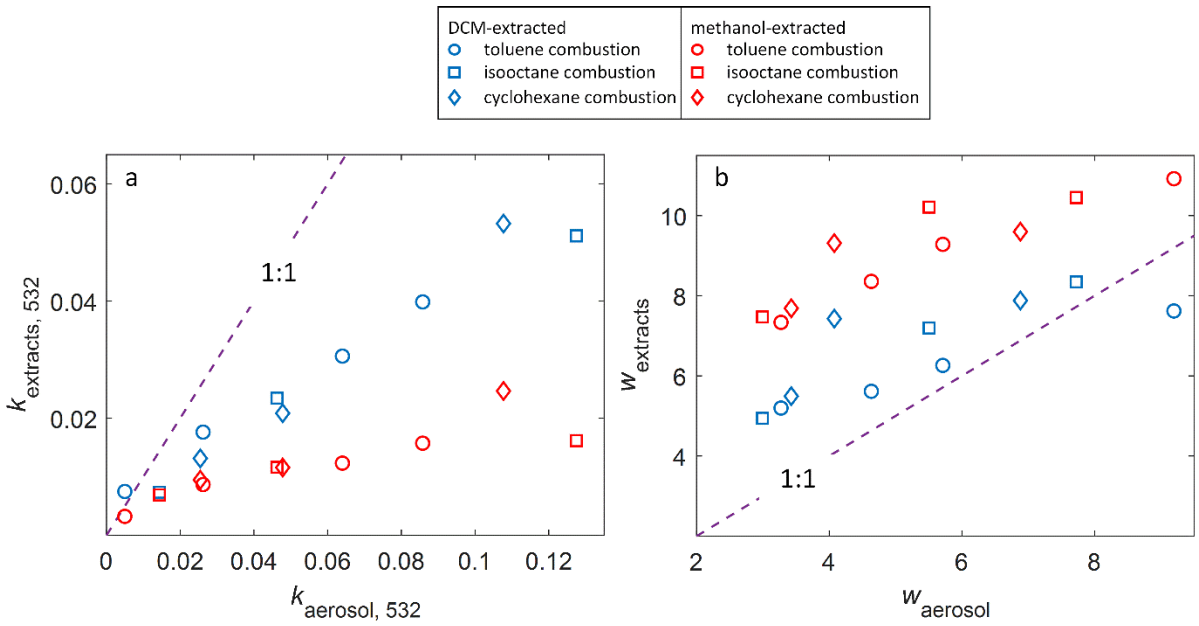


**Figure 4.4.** Comparison of BrC light-absorption properties retrieved from online measurements (aerosol) and offline measurements (extracts) using methanol and DCM as solvents. For clarity, uncertainty bounds (given in Table S4.1) are not shown in the figures. a) Imaginary part of the refractive indices at 532 nm. b) Wavelength dependence of the imaginary part of the refractive indices.

### 4.3.3 The continuum of light-absorption properties

We have previously established that BrC exhibits a continuum of light-absorption properties characterized by pairs of inversely correlated mid-visible $k$ (e.g., $k$ at 550 nm, $k_{550}$) and its wavelength dependence ($w$), where $k_{550}$ and $w$ approach those of BC for the darkest BrC on the continuum (Saleh et al. 2018). In that study, we generated BrC from the combustion of benzene and toluene and retrieved the light-absorption properties from online measurements (same procedure as Section 4.2.2). In this study, we further expanded the data set by 1) generating BrC from two additional structurally different fuels (cyclohexane and isooctane) and 2) retrieving $k_{550}$

and $w$ of BrC extracts using methanol and DCM as solvents in addition to $k_{550}$ and $w$ of the aerosol. All the $w$ versus $k_{550}$ data points from this study and Saleh et al. (2018) are plotted in Figure 4.5. The $k_{550}$ values from this study were calculated from the $k_{532}$ (retrieved from the online $b_{abs}$ measurements at 532 nm) and $w$ values plotted in Figure 4.4 as $k_{550} = k_{532}\,(532/550)^{w}$.

As shown in Figure 4.5, regardless of structural difference (branched alkane, cycloalkane, aromatic), BrC from all three fuels reproduced the brown-black continuum introduced by Saleh et al. (2018) with well-correlated $k_{550}$ and $w$. This result further confirms that BrC production and its light-absorption properties are not tied to certain fuel types, but are governed by combustion conditions (Saleh et al. 2018; Saleh 2020; Cheng et al. 2019). The combustion of any hydrocarbon fuel can produce BrC at any location along the brown-black continuum if combusted at the "right" combustion conditions (temperature, equivalence ratio). However, these right conditions are different for different fuels (Cheng et al. 2019; Saleh 2020).

Even though the solvents, especially methanol, only extracted the less-absorbing fraction of the BrC samples, the $k_{550}$ and $w$ of the extracts still fall on the same continuum as those of the BrC aerosol. This provides further evidence for the inverse relation between $k_{550}$ and $w$ of BrC. Furthermore, these results provide support for the conclusion that the differences observed between $k_{aerosol}$ and $k_{extracts}$ (Figure 4.4) are due to the inefficiency of solvent extraction and not due to intrinsic differences between the online and offline methods.

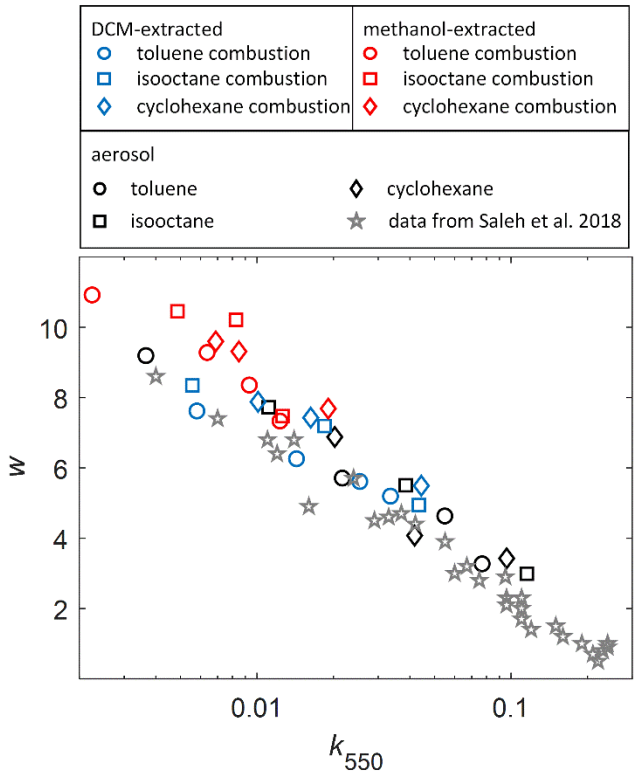


**Figure 4.5.** Wavelength dependence of the imaginary part of the refractive index ($w$) versus the imaginary part of the refractive index at 550 nm ($k_{550}$) of BrC generated from controlled-combustion of toluene, isooctane, and cyclohexane. The $k_{550}$ and $w$ values include those retrieved from online measurements (aerosol) and offline measurements using solvent-extraction by DCM and methanol (extracts). Uncertainty bounds (given in Table S4.1 in SI) are not shown for clarity. Also shown are $k_{550}$ and $w$ values from Saleh et al. (2018) for BrC aerosol produced from the combustion of toluene and benzene.

### 4.4. Conclusions

The experiments performed in this study revealed significant discrepancies between BrC light-absorption properties retrieved using online methods and offline solvent-extraction methods. These discrepancies are mainly associated with extraction inefficiency, which is more prominent

for darker BrC. For the BrC produced in this study from the combustion of toluene, cyclohexane, and isooctane, DCM exhibited better extraction efficiency, and thus less bias in retrieved light-absorption properties, than methanol, indicating that DCM is a more powerful solvent for extracting combustion BrC. However, even with DCM, the imaginary part of the refractive indices of the extracts were significantly smaller than those of the aerosol, with the difference increasing with increasing BrC darkness. Therefore, it should be noted that BrC light-absorption properties obtained using offline solvent-extraction techniques are those of the extracted fraction and are not necessarily representative of the whole BrC. The results obtained in this study also provide further evidence that BrC exhibits a continuum of light-absorption properties characterized by pairs of inversely correlated mid-visible imaginary part of the refractive indices (e.g., at 550 nm, $k_{550}$) and their wavelength dependence ($w$). The inverse correlation between $k_{550}$ and $w$ applies for BrC produced from the combustion of structurally different fuels and for $k_{550}$ and $w$ obtained from both online and offline solvent-extraction techniques.

**Funding**

Financial support was provided by the National Science Foundation, Division of Atmospheric and Geospace Sciences (AGS-1748080) and the University of Georgia Interdisciplinary Seed Grant Initiative.

## References

Adler, G., N. L. Wagner, K. D. Lamb, K. M. Manfred, J. P. Schwarz, A. Franchin, A. M. Middlebrook, et al. 2019. Evidence in Biomass Burning Smoke for a Light- Absorbing Aerosol with Properties Intermediate between Brown and Black Carbon. *Aerosol Science and Technology* 53 (9): 976–89. doi.org/10.1080/02786826.2019.1617832.

Alfè, M., B. Apicella, A. Tregrossi, and A. Ciajolo. 2008. Identification of Large Polycyclic Aromatic Hydrocarbons in Carbon Particulates Formed in a Fuel-Rich Premixed Ethylene Flame. *Carbon* 46 (15): 2059–66. doi.org/10.1016/j.carbon.2008.08.019.

Andreae, M. O., and A. Gelencsér. 2006. Black Carbon or Brown Carbon? The Nature of Light-Absorbing Carbonaceous Aerosols. *Atmos. Chem. Phys.* 6 (10): 3131–48. doi.org/10.5194/acp-6-3131-2006.

Apicella, B., A. Carpentieri, M. Alfè, R. Barbella, A. Tregrossi, P. Pucci, and A. Ciajolo. 2007. Mass Spectrometric Analysis of Large PAH in a Fuel-Rich Ethylene Flame. *Proceedings of the Combustion Institute* 31: 547–53. doi.org/10.1016/j.proci.2006.08.014.

Bluvshtein, N., J. M. Flores, A. A. Riziq, Y. Rudich, N. Bluvshtein, J. M. Flores, A. A. Riziq, and Y. Rudich. 2012. An Approach for Faster Retrieval of Aerosols ' Complex Refractive Index Using Cavity Ring-Down Spectroscopy An Approach for Faster Retrieval of Aerosols ' Complex Refractive Index Using Cavity Ring-Down Spectroscopy. *Aerosol Science and*

*Technology* 46: 1140–1150. doi.org/10.1080/02786826.2012.700141.

Bluvshtein, N., J. M. Flores, Q. He, E. Segre, L. Segev, N. Hong, A. Donohue, J. N. Hilfiker, and Y. Rudich. 2017. Calibration of a Multi-Pass Photoacoustic Spectrometer Cell Using Light-Absorbing Aerosols. *Atmos. Meas. Tech.* 10: 1203–13. doi.org/10.5194/amt-10-1203-2017.

Bond, T. C., S. J. Doherty, D. W. Fahey, P. M. Forster, T. Berntsen, B. J. Deangelo, M. G. Flanner, et al. 2013. Bounding the Role of Black Carbon in the Climate System: A Scientific Assessment. *Geophysical Research Atmospheres* 118 (11): 5380–5552. doi.org/10.1002/jgrd.50171.

Chakrabarty, R. K., H. Moosmüller, L. W. A. Chen, K. Lewis, W. P. Arnott, C. Mazzoleni, M. K. Dubey, et al. 2010. Brown Carbon in Tar Balls from Smoldering Biomass Combustion. *Atmos. Chem. Phys.* 10 (13): 6363–70. doi.org/10.5194/acp-10-6363-2010.

Chen, Y., and T. C. Bond. 2010. Light Absorption by Organic Carbon from Wood Combustion. *Atmos. Chem. Phys.* 9 (2001): 20471–513. doi.org/10.5194/acpd-9-20471-2009.

Cheng, Y., K. He, Z. Du, G. Engling, J. Liu, Y. Ma, M. Zheng, and R. J. Weber. 2016. The Characteristics of Brown Carbon Aerosol during Winter in Beijing. *Atmospheric Environment* 127: 355–64. doi.org/10.1016/j.atmosenv.2015.12.035.

Cheng, Z., K. M. Atwi, Z. Yu, A. Avery, C. Fortner, L. Williams, F. Majluf, J. E. Krechmer, and A. T. Lambe. 2020. Evolution of the Light-Absorption Properties of Combustion Brown Carbon Aerosols Following Reaction with Nitrate Radicals. *Aerosol Science and Technology* 0 (0): 1–15. doi.org/10.1080/02786826.2020.1726867.

Cheng, Z., K. Atwi, T. Onyima, and R. Saleh. 2019. Investigating the Dependence of Light-Absorption Properties of Combustion Carbonaceous Aerosols on Combustion Conditions. *Aerosol Science and Technology* 53 (4): 419–34. doi.org/10.1080/02786826.2019.1566593.

Claeys, M., R. Vermeylen, F. Yasmeen, Y. Gómez-González, X. Chi, W. Maenhaut, T. Mészáros, and I. Salma. 2012. Chemical Characterisation of Humic-like Substances from Urban, Rural and Tropical Biomass Burning Environments Using Liquid Chromatography with UV/Vis Photodiode Array Detection and Electrospray Ionisation Mass Spectrometry. *Environ. Chem.* 9 (3): 273–84. doi.org/10.1071/EN11163.

Corbin, J. C., H. Czech, D. Massabò, F. B. de Mongeot, G. Jakobi, F. Liu, P. Lobo, et al. 2019. Infrared-Absorbing Carbonaceous Tar Can Dominate Light Absorption by Marine-Engine Exhaust. *Npj Climate and Atmospheric Science* 2 (1). doi.org/10.1038/s41612-019-0069-5.

Desyaterik, Y., Y. Sun, X. Shen, T. Lee, X. Wang, T. Wang, and J. L. C. Jr. 2013. Speciation of "Brown" Carbon in Cloud Water Impacted by Agricultural Biomass Burning in Eastern China. *J. Geophys. Res. Atmos.* 118: 7389–99. doi.org/10.1002/jgrd.50561.

Dinar, E., A. Abo Riziq, C. Spindler, C. Erlick, G. Kiss, and Y. Rudich. 2007. The Complex Refractive Index of Atmospheric and Model Humic-like Substances (HULIS) Retrieved by a Cavity Ring down Aerosol Spectrometer (CRD-AS). *The Royal Society of Chemistry* 137: 279–95. doi.org/10.1039/b703111d.

Fischer, D. A., and G. D. Smith. 2018. A Portable, Four-Wavelength, Single-Cell Photoacoustic Spectrometer for Ambient Aerosol Absorption. *Aerosol Science and Technology* 52 (4): 393–406. doi.org/10.1080/02786826.2017.1413231.

Fuzzi, S., and S. Decesari. 2016. Light Absorption Properties of Brown Carbon in the High Himalayas. *J. Geophys. Res. Atmos.* 121: 9621–39. doi.org/10.1002/2016JD025030.Received.

Garvey, D. M., and R. G. Pinnick. 1983. Response Characteristics of the Particle Measuring Systems Active Scattering Aerosol Spectrometer Probe (ASASP–X). *Aerosol Science and Technology* 2 (4): 477–88. doi.org/10.1080/02786828308958651.

Hecobian, A., X. Zhang, M. Zheng, N. Frank, E. S. Edgerton, R. J. Weber, A. Sciences, T. Park, and N. Carolina. 2010. Water-Soluble Organic Aerosol Material and the Light-Absorption Characteristics of Aque- Ous Extracts Measured Over the Southeastern United States. Atmos. *Atmos. Chem. Phys.* 10: 5965–77. doi.org/10.5194/acp-10-5965-2010.

Kampf, C. J., A. Filippi, C. Zuth, T. Hoffmann, and T. Opatz. 2016. Secondary Brown Carbon Formation via the Dicarbonyl Imine Pathway: Nitrogen Heterocycle Formation and Synergistic Effect. *Phys.Chem.Chem.Phys* 18: 18353–64. doi.org/10.1039/c6cp03029g.

Lack, D. A., J. M. Langridge, R. Bahreini, C. D. Cappa, A. M. Middlebrook, and J. P. Schwarz. 2012. Brown Carbon and Internal Mixing in Biomass Burning Particles. *PNAS* 109 (37): 14802–7. doi.org/10.1073/pnas.1206575109.

Lack, D. A., E. R. Lovejoy, T. Baynard, A. Pettersson, and A. R. Ravishankara. 2006. Aerosol Absorption Measurement Using Photoacoustic Spectroscopy: Sensitivity, Calibration, and Uncertainty Developments. *Aerosol Science and Technology* 40 (9): 697–708. doi.org/10.1080/02786820600803917.

Lang-Yona, N., Y. Rudich, E. Segre, E. Dinar, and A. Abo-Riziq. 2009. Complex Refractive Indices of Aerosols Retrieved by Continuous Wave-Cavity Ring Down Aerosol. *Anal. Chem.* 81 (16): 1762–69.

Laskin, A., J. Laskin, and S. A. Nizkorodov. 2015. Chemistry of Atmospheric Brown Carbon. *Chemical Reviews* 115 (10): 4335–82. doi.org/10.1021/cr5006167.

Li, C., Q. He, A. P. S. Hettiyadura, U. Käfer, G. Shmul, D. Meidan, R. Zimmermann, et al. 2019. Formation of Secondary Brown Carbon in Biomass Burning Aerosol Proxies through NO3 Radical Reactions. *Environ. Sci. Technol.* 54 (3): 1395−1405. doi.org/10.1021/acs.est.9b05641.

Li, C., Q. He, J. Schade, J. Passig, R. Zimmermann, D. Meidan, A. Laskin, and Y. Rudich. 2019. Dynamic Changes in Optical and Chemical Properties of Tar Ball Aerosols by Atmospheric Photochemical Aging. *Atmos. Chem. Phys.* 19: 139–63.

Li, X., Y. Chen, and T. C. Bond. 2016. Light Absorption of Organic Aerosol from Pyrolysis of Corn Stalk. *Atmospheric Environment* 144: 249–56. doi.org/10.1016/j.atmosenv.2016.09.006.

Liu, D., J. Whitehead, M. R. Alfarra, E. Reyes-Villegas, D. V. Spracklen, C. L. Reddington, S. Kong, et al. 2017. Black-Carbon Absorption Enhancement in the Atmosphere Determined by Particle Mixing State. *Nature Geoscience* 10 (3): 184–88. doi.org/10.1038/ngeo2901.

Liu, J, M. Bergin, H. Guo, L. King, N. Kotra, E. Edgerton, and R. J. Weber. 2013. Size-Resolved Measurements of Brown Carbon in Water and Methanol Extracts and Estimates of Their

Contribution to Ambient Fine-Particle Light Absorption. *Atmos. Chem. Phys.* 13: 12389–404. doi.org/10.5194/acp-13-12389-2013.

Liu, J., P. Lin, A. Laskin, J. Laskin, S. M. Kathmann, M. Wise, R. Caylor, et al. 2016. Optical Properties and Aging of Light-Absorbing Secondary Organic Aerosol. *Atmos. Chem. Phys.* 16 (19): 12815–27. doi.org/10.5194/acp-16-12815-2016.

Malloy, Q. G. J., S. Nakao, L. Qi, R. Austin, C. Stothers, H. Hagino, and D. R. Cocker. 2009. Real-Time Aerosol Density Determination Utilizing a Modified Scanning Mobility Particle Sizer Aerosol Particle Mass Analyzer System. *Aerosol Science and Technology* 43 (7): 673–78. doi.org/10.1080/02786820902832960.

Marrero-Ortiz, W., M. Hu, Z. Du, Y. Ji, Y. Wang, S. Guo, Y. Lin, et al. 2019. Formation and Optical Properties of Brown Carbon from Small α-Dicarbonyls and Amines. *Environ. Sci. Technol.* 53 (1): 117–26. doi.org/10.1021/acs.est.8b03995.

McClure, C. D., C. Y. Lim, D. H. Hagan, J. H. Kroll, and C. D. Cappa. 2020. Biomass-Burning-Derived Particles from a Wide Variety of Fuels - Part 1: Properties of Primary Particles. *Atmospheric Chemistry and Physics* 20 (3): 1531–47. doi.org/10.5194/acp-20-1531-2020.

McMurry, P. H., X. Wang, K. Park, and K. Ehara. 2002. The Relationship between Mass and Mobility for Atmospheric Particles: A New Technique for Measuring Particle Density. *Aerosol Science and Technology* 36 (2): 227–38. doi.org/10.1080/027868202753504083.

Moise, T., J. M. Flores, and Y. Rudich. 2015. Optical Properties of Secondary Organic Aerosols and Their Changes by Chemical Processes. *Chem. Rev.* 115: 4400−4439.

doi.org/10.1021/cr5005259.

Phillips, S. M., and G. D. Smith. 2014. Light Absorption by Charge Transfer Complexes in Brown Carbon Aerosols. *Environ. Sci. Technol. Lett.* 1 (10): 382–86. doi.org/10.1021/ez500263j.

———. 2015. Further Evidence for Charge Transfer Complexes in Brown Carbon Aerosols from Excitation-Emission Matrix Fluorescence Spectroscopy. *J. Phys. Chem.* 119 (19): 4545–51. doi.org/10.1021/jp510709e.

Phillips, S. M., and G. D. Smith. 2017. Spectroscopic Comparison of Water- and Methanol-Soluble Brown Carbon Particulate Matter. *Aerosol Science and Technology* 51 (9): 1113–1121. doi.org/10.1080/02786826.2017.1334109.

Russo, C., M. Alfe, J. N. Rouzaud, F. Stanzione, A. Tregrossi, and A. Ciajolo. 2013. Probing Structures of Soot Formed in Premixed Flames of Methane, Ethylene and Benzene. *Proceedings of the Combustion Institute* 34 (1): 1885–92. doi.org/10.1016/j.proci.2012.06.127.

Saleh, R., C. J. Hennigan, G. R. McMeeking, W. K. Chuang, E. S. Robinson, H. Coe, N. M. Donahue, and A. L. Robinson. 2013. Absorptivity of Brown Carbon in Fresh and Photo-Chemically Aged Biomass-Burning Emissions. *Atmos. Chem. Phys.* 13: 7683–93. doi.org/10.5194/acp-13-7683-2013.

Saleh, R. 2020. From Measurements to Models: Toward Accurate Representation of Brown Carbon in Climate Calculations. *Curr Pollution Rep,* no. 706. doi.org/doi.org/10.1007/s40726-020-00139-3.

Saleh, R., Z. Cheng, and K. Atwi. 2018. The Brown–Black Continuum of Light-Absorbing Combustion Aerosols. Rapid-communication. *Environ. Sci. Technol. Lett.* 5: 508–13. doi.org/10.1021/acs.estlett.8b00305.

Saleh, R., E. S. Robinson, D. S. Tkacik, A. T. Ahern, S. Liu, A. C. Aiken, R. C. Sullivan, et al. 2014. Brownness of Organics in Aerosols from Biomass Burning Linked to Their Black Carbon Content. *Nature Geoscience* 7 (9): 647–50. doi.org/10.1038/ngeo2220.

Sengupta, D., V. Samburova, C. Bhattarai, E. Kirillova, L. Mazzoleni, M. Iaukea-Lum, A. Watts, H. Moosmüller, and A. Khlystov. 2018. Light Absorption by Polar and Non-Polar Aerosol Compounds from Laboratory Biomass Combustion. *Atmospheric Chemistry and Physics* 18 (15): 10849–67. doi.org/10.5194/acp-18-10849-2018.

Shetty, N. J., A. Pandey, S. Baker, W. M. Hao, and R. K. Chakrabarty. 2019. Measuring Light Absorption by Freshly Emitted Organic Aerosols: Optical Artifacts in Traditional Solvent-Extraction-Based Methods. *Atmos. Chem. Phys.* 19: 8817–30.

Stevens, R., and A. Dastoor. 2019. A Review of the Representation of Aerosol Mixing State in Atmospheric Models. *Atmosphere* 10 (4). doi.org/10.3390/atmos10040168.

Sun, H., L. Biedermann, and T. C. Bond. 2007. Color of Brown Carbon: A Model for Ultraviolet and Visible Light Absorption by Organic Carbon Aerosol. *Geophys. Res. Lett.* 34: L17813. doi.org/10.1029/2007GL029797.

Wiegand, J. R., L. D. Mathews, and G. D. Smith. 2014. A UV-Vis Photoacoustic Spectrophotometer. *Anal. Chem.* 86 (12): 6049–56. doi.org/10.1021/ac501196u.

Wu, G. M., Z. Y. Cong, S. C. Kang, K. Kawamura, P. Q. Fu, Y. L. Zhang, X. Wan, S. P. Gao, and B. Liu. 2016. Brown Carbon in the Cryosphere: Current Knowledge and Perspective. *Advances in Climate Change Research* 7 (1–2): 82–89. doi.org/10.1016/j.accre.2016.06.002.

Xie, M., X. Chen, M. D. Hays, M. Lewandowski, O. John, T. E. Kleindienst, and A. L. Holder. 2017. Light Absorption of Secondary Organic Aerosol: Composition and Contribution of Nitroaromatic Compounds. *Environ. Sci. Technol.* 51: 11607−11616. doi.org/10.1021/acs.est.7b03263.

Xie, M., M. D. Hays, and A. L. Holder. 2017. Light-Absorbing Organic Carbon from Prescribed and Laboratory Biomass Burning and Gasoline Vehicle Emissions. *Scientific Reports* 7 (1): 1–9. doi.org/10.1038/s41598-017-06981-8.

Zhang, X., Y. H. Lin, J. D. Surratt, and R. J. Weber. 2013. Sources, Composition and Absorption Ångström Exponent of Light-Absorbing Organic Components in Aerosol Extracts from the Los Angeles Basin. *Environ. Sci. Technol.* 47 (8): 3685–93. doi.org/10.1021/es305047b.

# CHAPTER 5

# CONCLUSION

The central goal of this dissertation is to fill some of the important knowledge gaps of the optical properties of BrC, which will enable better representation of BrC in climate models. The main objectives of this dissertation are to 1) design controlled-combustion experiments where combustion conditions (relative flowrates of $O_2$, $N_2$, and fuel and combustion temperature) are varied systematically; 2) perform measurements to constrain the light-absorption properties of the combustion BrC and BrC-BC mixtures at different combustion conditions; 3) investigate the evolution of BrC light-absorption properties due to nighttime oxidation with $NO_3$; and 4) assess the bias associated with quantifying the light-absorption properties BrC using the solvent extraction method.

In the controlled-combustion experiments, we used benzene and toluene as model fuels to generate combustion carbonaceous aerosols that span both pure BrC ae well as mixed BrC+BC. We showed that the light-absorption properties of carbonaceous aerosols follow the brown-black continuum that the BrC and BC produced by both fuels fall on the same light-absorption continuum, which can be characterized by pairs of increasing MAC at 532 nm ($MAC_{532}$) and decreasing AAE. For both the pure BrC and mixed BrC+BC regimes, $MAC_{532}$ increases and AAE decreases with increasing EC/OC regardless of fuel type, which indicates that light-absorption properties of carbonaceous aerosols do not depend on the fuel type, and more efficient combustion can generate progressively darker BrC as well as increase BC fraction. This finding provides a fundamental basis for previous reports on the observed dependence of light-absorption properties on EC/OC. It

also suggests that a unified framework can potentially be implemented to parameterize the light-absorption properties of carbonaceous aerosols produced through the soot-formation route in both the pure-organic (e.g., smoldering) and BC-forming (e.g., flaming) combustion regimes.

In the collaborative project with Aerodyne Research, Inc., we investigated the evolution of chemical composition and light-absorption properties of BrC due to heterogeneous reaction with $NO_3$. We performed controlled-combustion with toluene to generated BrC with varying light-absorption properties, which we categorized as light, medium, and dark BrC. Then we investigated the light-absorption properties and chemical composition of these BrC before and after exposure to $NO_3$ in an OFR. We found that exposure to $NO_3$ in the OFR can generate nitro-PAHs from both heterogeneous oxidation of the particulate PAHs as well as SOA formation from gas-phase oxidation and subsequent condensation of PAH vapors. Based on this mechanism, we found that heterogeneous oxidation could significantly enhance the light-absorption properties of all three types of BrC. On the other hand, the SOA formation would counterbalance this enhancement since SOA was likely less absorbing than the particulate PAHs, thereby reducing the overall light absorption of the oxidized BrC.

In the last project, we compared the *k* and *w* value of BrC retrieved using online and offline methods. We generated BrC with variable light-absorption properties by performing controlled-combustion experiments with three structurally different fuels: toluene (aromatic), isooctane (branched alkane), and cyclohexane (cyclic alkane). We used an online retrieval method with Mie calculations to retrieve the *k* value of BrC aerosols at 422 nm, 532 nm, and 782 nm. Then we use an offline method to retrieve the light-absorption properties of these BrC aerosol extracted by methanol and DCM. We found that the *k* values of extracts in both solvents were similar to those

of the aerosol. However, for darker BrC, *k* values of the BrC extracts in DCM were smaller than those of the BrC aerosol, but larger than *k* values of the BrC extracts in methanol, with the discrepancy among the three increasing with increasing BrC darkness. These results indicate that DCM has a higher extraction efficiency of BrC produced in this study than methanol, and the BrC solubility in both solvents decreased with increasing BrC darkness. Finally, *k* of BrC produced from all fuels, for both BrC aerosol and extracts, followed the same trend of decreasing wavelength dependence (flatter absorption spectra) with increasing *k* as previous data, further supporting the brown-black continuum of light-absorption properties.

The results obtained in this study also provide further evidence that BrC exhibits a continuum of light-absorption properties characterized by pairs of inversely correlated pairs mid-visible imaginary part of the refractive indices (e.g., at 550 nm, $k_{550}$) and their wavelength dependence (*w*). The inverse correlation between $k_{550}$ and *w* applies for BrC produced from the combustion of structurally different fuels and for $k_{550}$ and *w* obtained from both online and offline solvent-extraction techniques.

# APPENDIX A

# SUPPLEMENTAL INFORMATION FOR CHAPTER 2

# INVESTIGATING THE DEPENDENCE OF LIGHT-ABSORPTION PROPERTIES OF COMBUSTION CARBONACEOUS AEROSOLS ON COMBUSTION CONDITIONS

**S2.1. Calculation of fuel concentration in bubbler output flow:**

As described in the main text section 2.2.1, the fuel is delivered to the combustion chamber by flowing air through a bubbler containing the fuel. Here, we perform calculations to confirm that the air exits the bubbler saturated with the fuel, and thus the fuel vapor concentration is equal to the saturation concentration.

For an air bubble rising in the fuel column, the change in the average concentration of the fuel vapor inside the bubbler can be calculated as:

$$V \times \frac{\mathrm{dC}}{\mathrm{d}t} = A \times K_{\mathrm{L}} \times (C_{\mathrm{sat}} - C) \quad \text{(S2.1)}$$

Where $V$ is the volume of the bubble, $A$ is the surface area of the bubble, $C$ is the average molar concentration of the fuel vapor in the bubble, $C_{\mathrm{sat}}$ is the molar saturation concentration of the fuel (the boundary condition at the air-liquid interface), and $K_{\mathrm{C}}$ is the mass transfer coefficient at the air-liquid interface:

$$K_{\mathrm{C}} = Sh \times D_{\mathrm{AB}}/d \quad \text{(S2.2)}$$

Where $d$ is the bubble diameter (observed to be approximately 1cm), $D_{\mathrm{AB}}$ is the diffusion coefficient of the fuel in air calculated from the EPA online tool (https://www3.epa.gov/ceampubl/learn2model/part-two/onsite/estdiffusion.html) ($8.94\times10^{-2}$ $\mathrm{cm}^2/\mathrm{s}$ for benzene and $8.04\times10^{-2}$ $\mathrm{cm}^2/\mathrm{s}$ for toluene), and Sh is the Sherwood number calculated using the Ranz-Marshall Correlation:

$$\mathrm{Sh} = 2 + 0.6 \times \mathrm{Re}^{0.5}\mathrm{Sc}^{0.33} \quad \text{(S2.3)}$$

Where Re is Reynolds number (Re = $U\,d/v$), and Sc is Schmidt number (Sc = $v/D_{AB}$). $U$ is the average rising velocity of the bubble in the fuel column (observed to be approximately 30 cm/s) and $v$ is the kinematic viscosity of the liquid fuel ($6.94\times10^{-3}$ cm$^2$/s for benzene and $6.50\times10^{-3}$ cm$^2$/s for toluene). Hence, $K_L$ for both benzene and toluene is approximately 1.2 cm/s.

Equation (S2.1) can be written in normalized form as:

$$\frac{\mathrm{dSR}}{\mathrm{d}t} = \frac{6}{\mathrm{d}} K_C (1 - SR) \qquad \text{(S2.4)}$$

Where $SR = \frac{C}{C_{\mathrm{sat}}}$ is the saturation ratio.

Solving equation S2.4, the time-dependent SR can be expressed as:

$$\mathrm{SR} = 1 - \exp\left(-\frac{t}{\tau}\right) \qquad \text{(S2.5)}$$

Equation S2.5 is a first-order dynamic response with a time constant $\tau = d/6K_C = 0.14$ s (for $d$ = 1cm and $K_C$ = 1.2 cm/s).

Equilibrium is usually assumed to be achieved at $t_{eq} = 3\tau$. In our experiments, $t_{eq}$ = 0.42 s, which is smaller than the bubble rising time in our experiments (larger than 1 s). Therefore, we are confident that air exits the bubbler saturated with the fuel.

**S2. Uncertainty analysis:**

Uncertainties of the measured mass loadings of OC, EC, and TC by the OC-EC analyzer were calculated based on the manufacturer's specifications as:

$$m_{\mathrm{OC,unc}} = \pm(0.20\ \mu\mathrm{g} + 0.05\ m_{OC}) \qquad \text{(S2.6)}$$

$$m_{\mathrm{EC,unc}} = \pm(0.20\ \mu g + 0.05\ m_{EC}) \quad \text{(S2.7)}$$

$$m_{\mathrm{TC,unc}} = \pm(0.30\ \mu g + 0.05\ m_{TC}) \quad \text{(S2.8)}$$

Where $m_{OC}$, $m_{EC}$, and $m_{TC}$ are the mass loading of OC, EC, and TC, respectively.

The uncertainty in EC/OC was calculated by propagating the uncertainties in OC and EC:

$$\mathrm{EC/OC_{unc}} = \mathrm{EC/OC}\sqrt{(m_{\mathrm{EC,unc}}/m_{EC})^2 + (m_{\mathrm{OC,unc}}/m_{OC})^2} \quad \text{(S2.9)}$$

The uncertainty of the aerosol mass concentration ($C_{\mathrm{p,\ unc}}$) was calculated as:

$$C_{\mathrm{p,unc}} = \frac{m_{\mathrm{TC,unc}}}{t \cdot Q} \quad \text{(S2.10)}$$

Where $Q$ is the sample collection flow rate, and $t$ is the sample collection time.

The uncertainty in the effective density ($\rho_{\mathrm{eff,\ unc}}$) was calculated as:

$$\rho_{\mathrm{eff,unc}} = \rho_{\mathrm{eff}}\sqrt{(C_{\mathrm{p,unc}}/C_{\mathrm{p}})^2 + (\sigma_{\mathrm{V_p}}/V_{\mathrm{p}})^2} \quad \text{(S2.11)}$$

Where $\rho_{\mathrm{eff}}$ is the mean value of particle effective density, $C_{\mathrm{p}}$ is the particle mass concentration, $V_{\mathrm{p}}$ is the average SMPS integrated volume concentration over the sampling period, and $\sigma_{\mathrm{Vp}}$ is the standard deviation of the SMPS integrated volume concentration over the sampling period.

The uncertainty in the material density of the aerosol ($\rho_{\mathrm{p,\ unc}}$) was calculated by:

$$\rho_{\mathrm{p,unc}} = \sqrt{{\rho_{\mathrm{BrC,unc}}}^2 + (\rho_{\mathrm{BC}} - \rho_{\mathrm{BrC}})[\frac{({\rho_{\mathrm{BrC,unc}}}^2 - {\rho_{\mathrm{BC,unc}}}^2)}{(\rho_{\mathrm{BC}} - \rho_{\mathrm{BrC}})^2} + (\frac{\mathrm{EC/TC}_{unc}}{\mathrm{EC/TC}})^2]} \quad \text{(S2.12)}$$

where $\rho_{BrC}$ and $\rho_{BC}$ are the density of BrC and BC respectively, $\rho_{BrC,unc}$ and $\rho_{BC,unc}$ are the uncertainty of the density of BrC and BC respectively, and $EC/TC_{unc}$ is the uncertainty of EC/TC calculated as:

$$\mathrm{EC/TC_{unc}} = \mathrm{EC/TC}\sqrt{(m_{\mathrm{EC,unc}}/m_{EC})^2 + (m_{\mathrm{TC,unc}}/m_{TC})^2} \quad \text{(S2.13)}$$

Hence, the uncertainty in the shape factor was calculated as:

$$\chi_{unc} = \frac{\chi}{3}\sqrt{(\rho_{\mathrm{p,unc}}/\rho_{\mathrm{p}})^2 + (\rho_{\mathrm{eff,unc}}/\rho_{\mathrm{eff}})^2} \quad \text{(S2.14)}$$

The uncertainty in $MAC_{532}$ ($MAC_{532,\,unc}$) was calculated as:

$$\mathrm{MAC_{532,unc}} = \mathrm{MAC_{532}}\sqrt{(\sigma_{b_{\mathrm{abs,532}}}/b_{\mathrm{abs,532}})^2 + (C_{\mathrm{p,unc}}/C_{\mathrm{p}})^2} \quad \text{(S2.15)}$$

Where $b_{abs,\,532}$ is the average absorption coefficient at 532 nm over the course of an experiment and $\sigma_{babs,532}$ is the standard deviation of $b_{abs,\,532}$.

## Table S2.1. Summary of experimental conditions and data

| Fuel | Combustion temperature (˚C) | Equivalence ratio | Modified equivalence ratio | Mass concentration (μg/cm$^3$) | EC/OC | Effective density (g/cm$^3$) | Shape factor | MAC at 532 nm (m$^2$/g) | AAE |
|---|---|---|---|---|---|---|---|---|---|
| Benzene | 1050 | 1.23 | 2.09 | 173±13 | 2.55±0.20 | 0.46±0.05 | 1.53±0.06 | 5.69±0.47 | 1.5±0.07 |
| | 1050 | 1.24 | 2.11 | 226±16 | 1.75±0.14 | 0.72±0.10 | 1.31±0.07 | 4.36±0.49 | 1.7±0.09 |
| | 1050 | 1.22 | 2.30 | 325±25 | 1.34±0.11 | 1.24±0.14 | 1.09±0.05 | 2.91±0.27 | 2.2±0.09 |
| | 1050 | 1.17 | 3.29 | 425±31 | 0.23±0.02 | 1.20±0.10 | 1.05±0.04 | 1.91±0.16 | 3.3±0.09 |
| | 1050 | 1.21 | 3.65 | 361±28 | 0.05±0.01 | 1.23±0.16 | 1.02±0.07 | 0.78±0.08 | 5.6±019 |
| | 1050 | 1.17 | 3.76 | 234±18 | 0.02±0.01 | 1.44±0.12 | 0.97±0.12 | 0.29±0.03 | 7.3±0.15 |
| | 950 | 1.22 | 2.08 | 80±10 | 3.14±0.30 | 0.09±0.02 | 2.63±0.15 | 6.43±0.88 | 1.7±0.03 |
| | 950 | 1.28 | 2.20 | 123±12 | 0.88±0.09 | 0.27±0.04 | 1.77±0.10 | 4.59±0.55 | 2.0±0.04 |
| | 950 | 1.47 | 2.53 | 416±28 | 0.25±0.02 | 1.33±0.18 | 1.02±0.05 | 2.09±0.25 | 3.1±0.18 |
| | 950 | 1.42 | 2.65 | 431±29 | 0.11±0.01 | 1.32±0.10 | 1.01±0.04 | 1.19±0.11 | 4.3±0.22 |
| | 950 | 1.42 | 2.78 | 436±30 | 0.04±0.01 | 1.33±0.11 | 1.00±0.05 | 0.60±0.07 | 6.3±0.38 |
| | 950 | 1.43 | 3.06 | 464±31 | 0.01±0.01 | 1.54±0.11 | 0.95±0.12 | 0.23±0.02 | 8.5±0.83 |
| Toluene | 1050 | 0.89 | 1.61 | 103±11 | 2.76±0.26 | 0.15±0.06 | 2.25±0.23 | 5.41±1.09 | 1.4±0.04 |
| | 1050 | 0.95 | 2.82 | 331±23 | 1.00±0.08 | 0.82±0.15 | 1.24±0.08 | 2.83±0.40 | 2.1±0.07 |
| | 1050 | 0.99 | 3.15 | 363±29 | 0.19±0.02 | 1.14±0.10 | 1.07±0.05 | 1.88±0.17 | 3.3±0.11 |
| | 1050 | 1.01 | 3.25 | 363±27 | 0.04±0.01 | 1.17±0.13 | 1.04±0.07 | 0.68±0.17 | 5.7±0.18 |
| | 1050 | 1.07 | 3.51 | 397±28 | 0.01±0.01 | 1.42±0.15 | 0.97±0.12 | 0.24±0.03 | 8.6±0.13 |
| | 950 | 1.00 | 1.72 | 132±11 | 3.57±0.29 | 0.20±0.03 | 2.03±0.09 | 7.66±0.86 | 1.5±0.05 |
| | 950 | 0.97 | 1.92 | 267±19 | 1.39±0.10 | 0.55±0.05 | 1.42±0.06 | 4.83±0.36 | 2.0±0.13 |
| | 950 | 0.99 | 1.94 | 468±32 | 0.42±0.04 | 1.08±0.08 | 1.10±0.04 | 2.39±0.18 | 2.8±0.12 |
| | 950 | 0.97 | 2.10 | 334±26 | 0.18±0.02 | 1.06±0.12 | 1.09±0.05 | 1.58±0.17 | 3.5±0.38 |
| | 950 | 0.98 | 2.22 | 424±30 | 0.05±0.01 | 1.29±0.18 | 1.01±0.06 | 0.79±0.20 | 5.7±0.66 |
| | 950 | 1.05 | 2.51 | 358±25 | 0.02±0.01 | 1.40±0.11 | 0.98±0.10 | 0.28±0.02 | 8.0±0.15 |

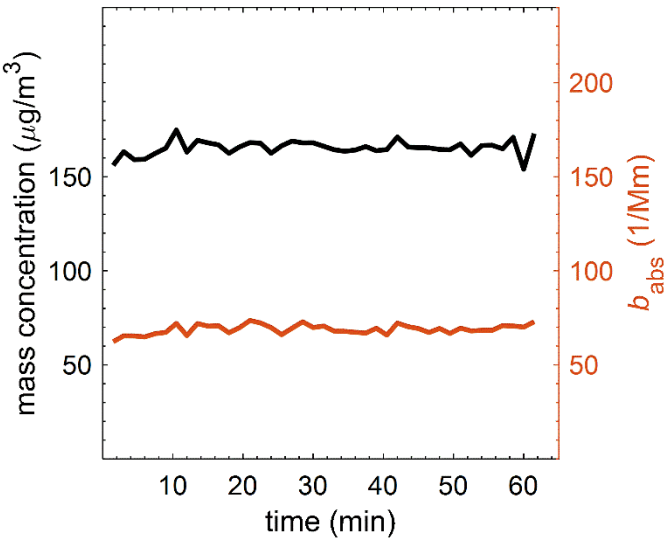


**Figure S2.1.** Typical time series of integrated SMPS mass concentrations (assuming a density of 1 g/cm$^3$) and absorption coefficients at 532 nm ($b_{abs,532}$) measured using the Multi-PAS III over a typical sampling period.

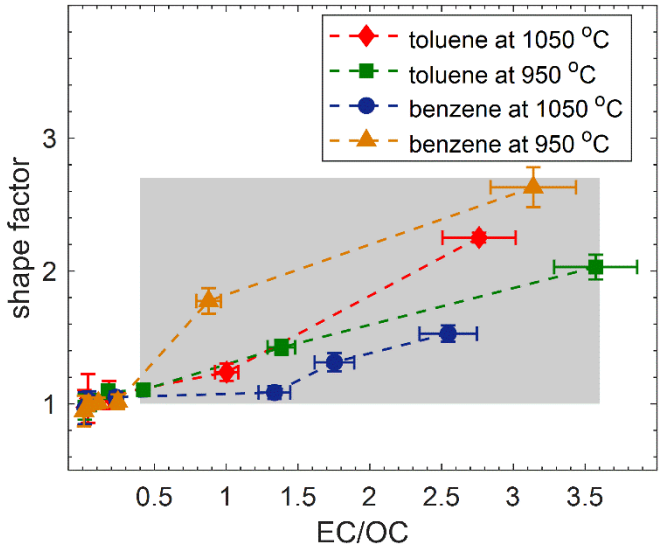


**Figure S2.2.** The dependence of the shape factor of the carbonaceous aerosols emitted from benzene and toluene combustion on EC/OC. The EC/OC reported here is corrected for adsorbed VOCs (see the VOCs correction in section 2.3). The shaded regions correspond to combustion

conditions that produced mixed BrC+BC particles, and the non-shaded regions correspond to conditions that produced pure BrC particles. Error bars represent measurement uncertainty.

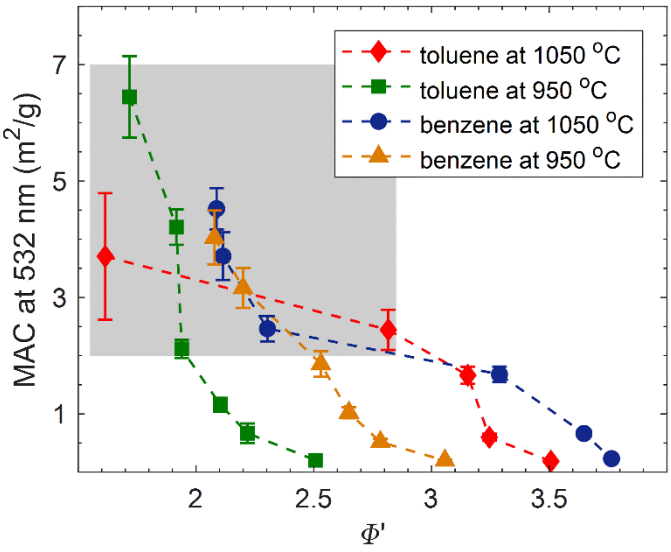


**Figure S2.3.** The dependence of the mass absorption cross-section at 532 nm ($MAC_{532}$) of the carbonaceous aerosols emitted from benzene and toluene combustion on the modified equivalence ratio ($\Phi$' – see derivation in section 2.2.1) for combustion temperatures of 950 °C and 1050°C. The shaded regions correspond to combustion conditions that produced mixed BrC+BC particles, and the non-shaded regions correspond to conditions that produced pure BrC particles. Error bars represent measurement uncertainty. The MAC reported here is not corrected for adsorbed VOCs. The MAC corrected for adsorbed VOCs is shown in the main text Figure 2.3.

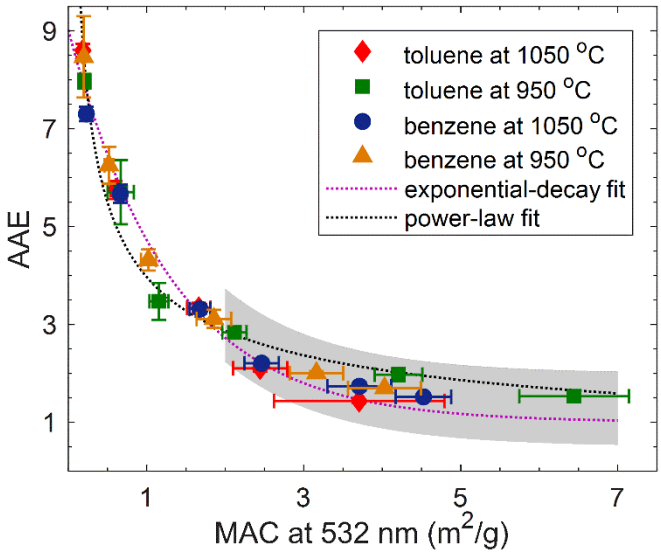


**Figure S2.4**. The mass absorption cross-section at 532 nm ($MAC_{532}$) versus the absorption Ånsgström exponent (AAE) for all the data points in Figure 2.3. The shaded region corresponds to mixed BrC+BC particles. The dotted magenta line is an exponential-decay fit (AAE = (8.03±0.27) exp ((-0.77±0.10) $MAC_{532}$) +1, $R^2$=0.9709). The dotted black line is a power-law fit (AAE = (3.98±0.22) $MAC_{532}^{-0.47\pm0.05}$, $R^2$=0.9686). Error bars represent measurement uncertainty. The MAC reported here is not corrected for adsorbed VOCs. The MAC corrected for adsorbed VOCs is shown in the main text Figure 2.4.

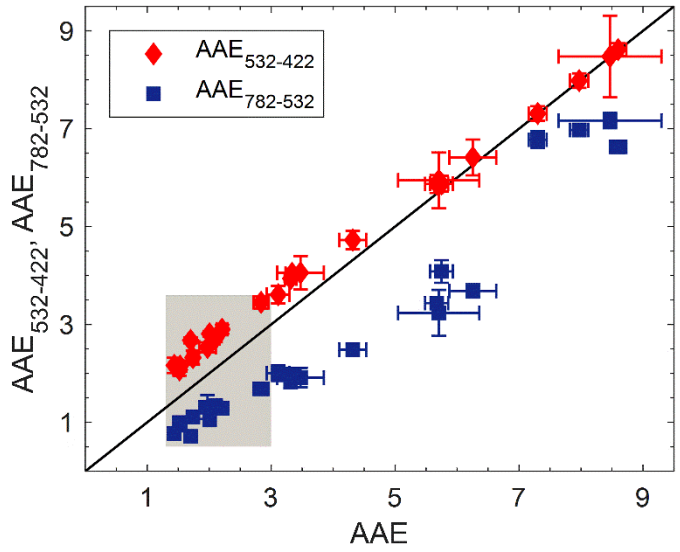


**Figure S2.5.** Absorption Ångström exponents (AAE) retrieved using the 3 wavelengths of the Multi-PAS III (422, 532, and 782 nm) versus AAE between 532 nm and 422 nm ($AAE_{532-422}$) and AAE between 782 nm and 532 nm ($AAE_{782-532}$). The black solid line is the 1:1 line. Error bars represent measurement uncertainty.

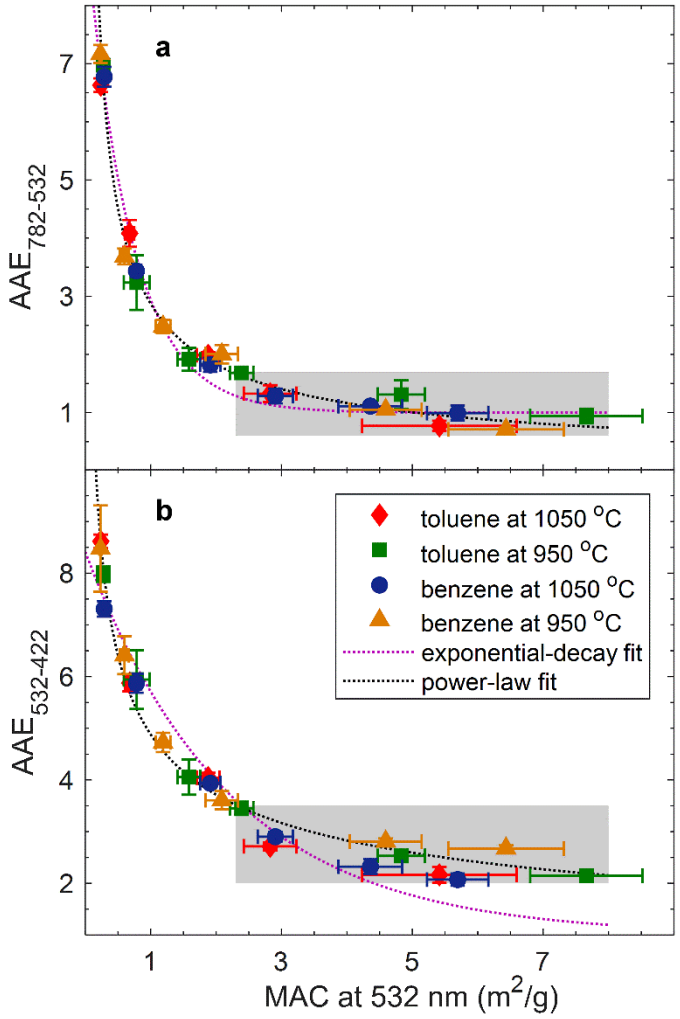


**Figure S2.6**. The mass absorption cross-section at 532 nm ($MAC_{532}$) versus the absorption Ångström exponent (AAE). The shaded regions correspond to mixed BrC+BC particles and the non-shaded regions correspond to pure BrC particles. The $MAC_{532}$ reported here is calculated based on the correction for adsorbed VOCs as described in section 2.2.2. a) $MAC_{532}$ versus AAE between 782 nm and 532 nm ($AAE_{782-532}$). The dotted magenta line is an exponential-decay fit ($AAE = (8.41\pm0.85) \exp((-1.47\pm0.23) MAC_{532}) +1$, $R^2=0.9793$). The dotted black line is a power-law fit ($AAE = (2.87\pm0.14) MAC_{532}^{-0.65\pm0.04}$, $R^2=0.9863$). and b) $MAC_{532}$ versus AAE between 532 nm and 422 nm ($AAE_{532-422}$). The dotted magenta line is an exponential-decay fit (AAE =

(7.42±0.73) exp ((-0.45±0.09) $MAC_{532}$) +1, $R^2$=0.9115). The dotted black line is a power-law fit (AAE = (4.88±0.17) $MAC_{532}^{-0.39\pm0.03}$, $R^2$=0.9713). Error bars represent measurement uncertainty.

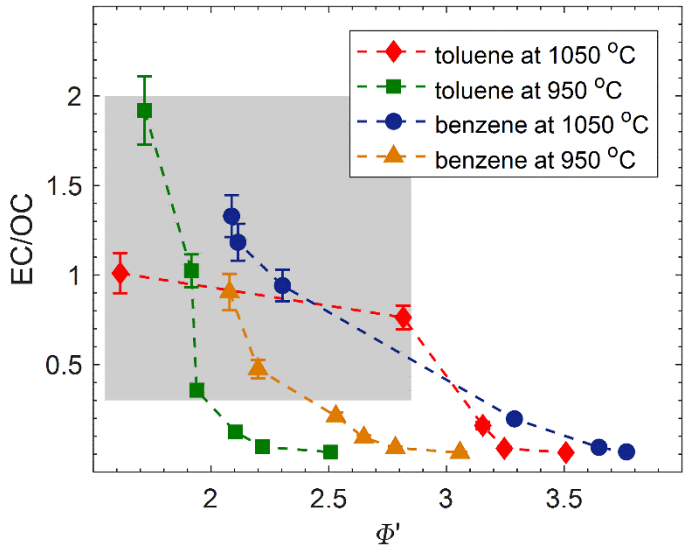


**Figure S2.7.** Elemental carbon-to-organic-carbon ratio (EC/OC) versus modified equivalence ratio (*Φ*') for all experiments. Error bars represent measurement uncertainty. The shaded region corresponds to mixed BrC+BC particles, and the non-shaded region corresponds to pure BrC particles. Error bars represent measurement uncertainty. The EC/OC reported here is not corrected for adsorbed VOCs. The EC/OC corrected for adsorbed VOCs is shown in the main text Figure 2.5.

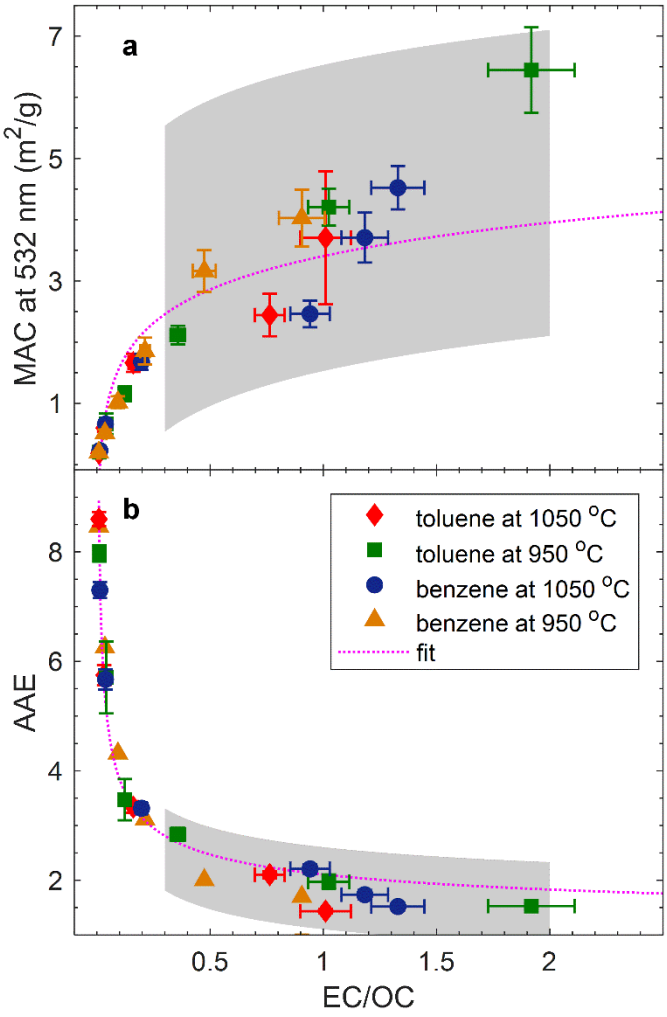


**Figure S2.8.** Parameterizing the light-absorption properties of combustion carbonaceous aerosols as a function of EC/OC. The MAC reported here is not corrected for adsorbed VOCs. The MAC corrected for adsorbed VOCs is shown in the main text Figure 2.6. Error bars represent measurement uncertainty, and dotted magenta lines are power-law fits. **a)** mass absorption cross-section at 532 nm ($MAC_{532}$) versus EC/OC. The fit logarithmic fit equation is $MAC_{532}$ = (0.83±0.17) log (EC/OC) +(3.53±0.44), $R^2$ = 0.8492. **b)** absorption Ångström exponent (AAE) versus EC/OC. The fit power-law fit equation is AAE = (1.11±0.19) $EC/OC^{-0.41\pm0.04}$+1, $R^2$=0.9723.

# APPENDIX B

# SUPPLEMENTAL INFORMATION FOR CHAPTER 3

# EVALUTION OF THE LIGHT-ABSORTPION PROPERTIES OF COMBUSTION BROWN CARBON AEROSOLS FOLLWING REACTION WITH NITRATE RADICALS

**S3.1. Estimation of $NO_3$ exposure levels:**

$NO_3$ exposure levels ($NO_{3,exp}$) were estimated from the decay of two tracers, butanal and thiophene, that were introduced at the oxidation flow reactor (OFR) inlet and detected with a Vocus Proton Transfer Reaction Time-of-Flight Mass Spectrometer (PTR-MS, Tofwerk/Aerodyne) (Krechmer et al. 2018). Assuming first-order reactive loss to $NO_3$, the tracer concentration is expressed as:

$$\frac{\mathrm{d[tracer]}}{\mathrm{d}t} = [\mathrm{tracer}]_o \exp\left(-k_{NO_3}[NO_3]t\right) \quad \text{(S3.1)}$$

Where $[tracer]_o$ and [tracer] are the initial and time-dependent tracer concentrations, respectively, and $[NO_3]$ is the time-independent $NO_3$ concentration. $k_{NO3}$ is the reaction rate constant with $NO_3$ reported in the literature (Atkinson 1991; D'Anna et al. 2001). Integrating equation (S3.1) yields:

$$-\ln\left(\frac{[\mathrm{tracer}]}{[\mathrm{tracer}]_o}\right) = k_{NO_3}[NO_3]\Delta t \quad \text{(S3.2)}$$

$NO_{3,\,exp}$ is the integrated $NO_3$ concentration over time, and can be obtained as

$$NO_{3,exp} = \ln\left(\frac{[\mathrm{tracer}]_o}{[\mathrm{tracer}]}\right)/k_{NO_3} \quad \text{(S3.3)}$$

where $[tracer]_o$ and [tracer] are obtained from the PTR-MS measurements.

**S3.2. Mass balance calculations for main text Section 3.3.2.3:**

We performed elemental (C, N, O) mass balance on the OA measured by the AMS / SP-AMS before and after oxidation to estimate the relative contribution of SOA condensation versus heterogeneous oxidation to the increase in OA mass concentration after oxidation with $NO_3$. To

do so, we converted the O/C, N/C, and H/C obtained from the AMS / SP-AMS measurements (main text Section 3.3.2.2) to a mass basis. By applying the constraint $m_{OA} = m_C + m_N + m_O + m_H$, where $m_{OA}$ is the OA mass concentration, $m_C$ is the carbon mass concentration, etc., we obtained a system of equations and solved for $m_C$, $m_N$, $m_O$, and $m_H$ for the unoxidized and oxidized BrC. We then calculated the increase in the mass concentration of each element after oxidation ($\Delta m_C$, $\Delta m_N$, $\Delta m_O$, $\Delta m_H$). Since heterogeneous oxidation only adds N and O to the particles, $\Delta m_C$ is only associated with SOA condensation.

To apportion the added N- and O-containing functional groups between SOA condensation and heterogeneous oxidation, we assumed that the SOA molecules contained 10-18 carbons, 0-1 nitrogens, and 2-4 oxygens (see main text Section 3.3.2.3 for the rationale behind these assumptions). For each assumed combination of carbon, nitrogen, and oxygen numbers, the oxygen and nitrogen mass contributed by SOA condensation can be calculated as:

$$\Delta m_{\mathrm{N,SOA}} = (\mathrm{N/C})_{\mathrm{SOA}} \times \frac{14\ \mathrm{g}\ mol^{-1}}{12\ \mathrm{g}\ mol^{-1}} \times \Delta m_{\mathrm{C}} \quad \text{(S3.4)}$$

$$\Delta m_{\mathrm{O,SOA}} = (\mathrm{O/C})_{\mathrm{SOA}} \times \frac{16\ \mathrm{g}\ mol^{-1}}{12\ \mathrm{g}\ mol^{-1}} \times \Delta m_{\mathrm{C}} \quad \text{(S3.5)}$$

The contribution of heterogeneous oxidation to the increase in nitrogen and oxygen mass of the oxidized particles can then be calculated as:

$$\Delta m_{\mathrm{N,het}} = \Delta m_{\mathrm{N}} - \Delta m_{\mathrm{N,SOA}} \quad \text{(S3.6)}$$

$$\Delta m_{\mathrm{O,het}} = \Delta m_{\mathrm{O}} - \Delta m_{\mathrm{O,SOA}} \quad \text{(S3.7)}$$

Finally, the ratios in Figure 3.6 in the main text are calculated as:

$$\Delta \mathrm{N}_{\mathrm{het}}/\Delta \mathrm{N}_{\mathrm{tot}} = \Delta m_{\mathrm{N,het}}/\Delta m_{\mathrm{N}} \quad \text{(S3.8)}$$

$$\Delta \mathrm{O}_{\mathrm{het}}/\Delta \mathrm{O}_{\mathrm{tot}} = \Delta m_{\mathrm{O,het}}/\Delta m_{\mathrm{O}} \quad \text{(S3.9)}$$

**Table S3.1. Summary of experimental data**

| | Light BrC | | Medium BrC | | Dark BrC | |
|---|---|---|---|---|---|---|
| | unoxidized | oxidized | unoxidized | oxidized | unoxidized | oxidized |
| $NO_3$ exposure (molec $cm^{-3}$ sec) | 0 | $5.2\times10^{13}$ | 0 | $5.2\times10^{13}$ | 0 | $5.2\times10^{13}$ |
| SMPS mass concentration ($\mu g\ m^{-3}$) | 236 | 324 | 261 | 84 | 109 | 145 |
| AMS OA ($\mu g\ m^{-3}$) | 84.1 | 110.5 | 61.7 | 86.1 | 3.5 | 6.2 |
| AMS nitrates ($\mu g\ m^{-3}$) | 1.3 | 7.9 | 1.2 | 11.1 | 0.8 | 1.8 |
| AMS $NO^+$:$NO_2^+$ | 1.6 | 1.9 | 1.3 | 1.6 | 1.9 | 2.1 |
| AMS O/C [a] | 0.15 | 0.24 | 0.17 | 0.34 | 0.90 | 0.94 |
| AMS H/C [b] | 0.78 | 0.80 | 0.76 | 0.80 | 1.04 | 0.95 |
| AMS N/C [c] | 0.01 | 0.03 | 0.01 | 0.06 | 0.11 | 0.20 |
| SP-AMS OA ($\mu g\ m^{-3}$) | 4 | 48.6 | No data | No data | 17.7 | 31.0 |
| SP-AMS nitrates ($\mu g\ m^{-3}$) | 0.2 | 3.0 | No data | No data | 1.8 | 5.0 |

| | | | | | | |
|---|---|---|---|---|---|---|
| SP-AMS $NO^+$:$NO_2^+$ | 2.1 | 1.2 | No data | No data | 1.4 | 1.3 |
| SP-AMS O/C [a] | 0.59 | 0.26 | No data | No data | 0.35 | 0.46 |
| SP-AMS H/C [b] | 1.04 | 1.00 | No data | No data | 0.88 | 0.97 |
| SP-AMS N/C [c] | 0.02 | 0.02 | No data | No data | 0.04 | 0.07 |
| SP-AMS BC ($\mu g\ m^{-3}$) | 0.2 | 0.4 | No data | No data | 4.3 | 6.4 |
| $MAC_{471}$ ($g\ m^{-2}$) [d] | 0.36 ± 8.3% | 0.33 ± 3.0% | 0.92 ± 5.4% | 1.01 ± 1.6% | 1.70 ± 7.1% | 1.86 ± 2.7% |
| $MAC_{532}$ ($g\ m^{-2}$) [d] | 0.13 ± 7.7% | 0.17 ± 1.8% | 0.41 ± 2.4% | 0.53 ± 2.1% | 1.39 ± 9.4% | 1.34 ± 1.5% |
| $MAC_{671}$ ($g\ m^{-2}$) [d] | 0.04 ± 5.0% | 0.09 ±4.4% | 0.23 ± 4.3% | 0.27 ± 2.0% | 0.95 ± 9.5% | 0.93 ± 2.2% |
| AAE [d] | 8.0 ± 6.3% | 4.4 ± 2.3% | 5.2 ± 3.8% | 4.3 ± 1.2% | 1.7 ± 5.9% | 2.0 ± 5.0% |
| $k_{473}$ [d] | 0.021 ± 9.5% | 0.019 ± 2.1% | 0.053 ± 3.8% | 0.057 ± 3.5% | 0.099 ± 7.1% | 0.106 ± 2.8% |
| $k_{532}$ [d] | 0.008 ± 3.8% | 0.011 ± 1.8% | 0.026 ± 3.8% | 0.034 ± 2.9% | 0.091 ± 9.9% | 0.088 ± 2.3% |
| $k_{671}$ [d] | 0.004 ± 5.0% | 0.008 ± 5.0% | 0.020 ± 5.0% | 0.024 ± 0.4% | 0.081 ± 9.9% | 0.079 ± 2.5% |
| $w$ [d] | 6.2 ± 8.1% | 2.9 ± 6.9% | 3.6 ± 0.3% | 2.8 ± 3.6% | 0.6 ± 15.7% | 0.8 ± 12.9% |

[a] ±12% uncertainty in O/C (Canagaratna et al. 2015).
[b] ±4% uncertainty in H/C (Canagaratna et al. 2015).
[c] ±12% uncertainty in N/C (Aiken, Decarlo, and Jimenez 2007).
[d] uncertainties represent the standard deviations over time for one experiment.

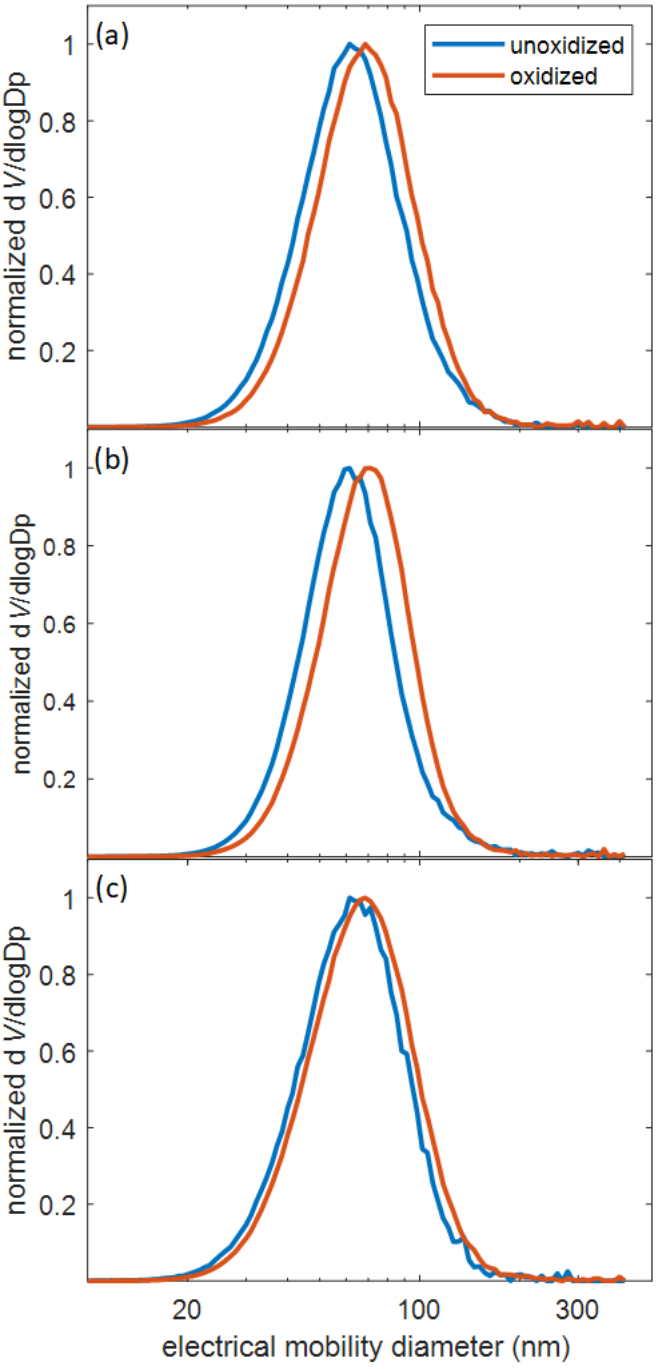


**Figure S3.1.** Typical SMPS relative volume distribution of unoxidized (blue) and oxidized (red). (a) light BrC. (b) medium BrC. (c) dark BrC.

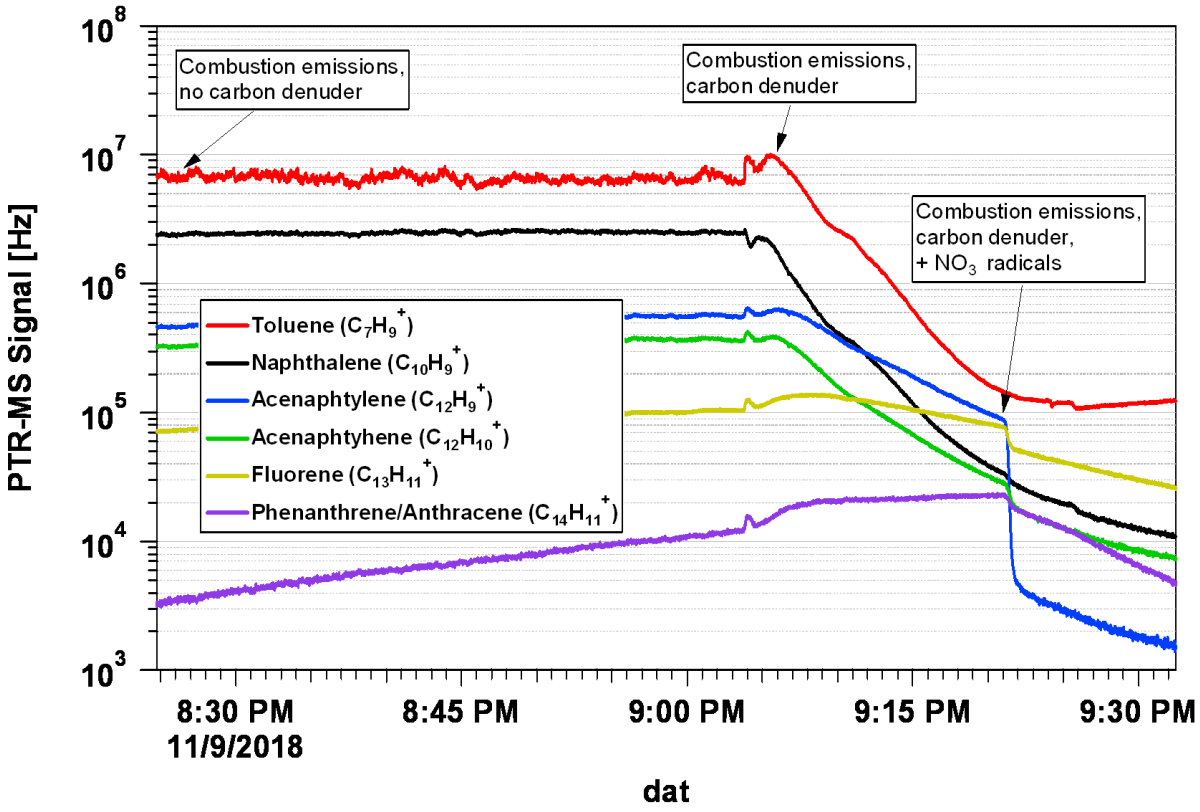


**Figure S3.2.** Time series of toluene and $C_{10}$-$C_{13}$ gas-phase PAHs emitted from the combustion source and measured with Vocus PTR-MS.

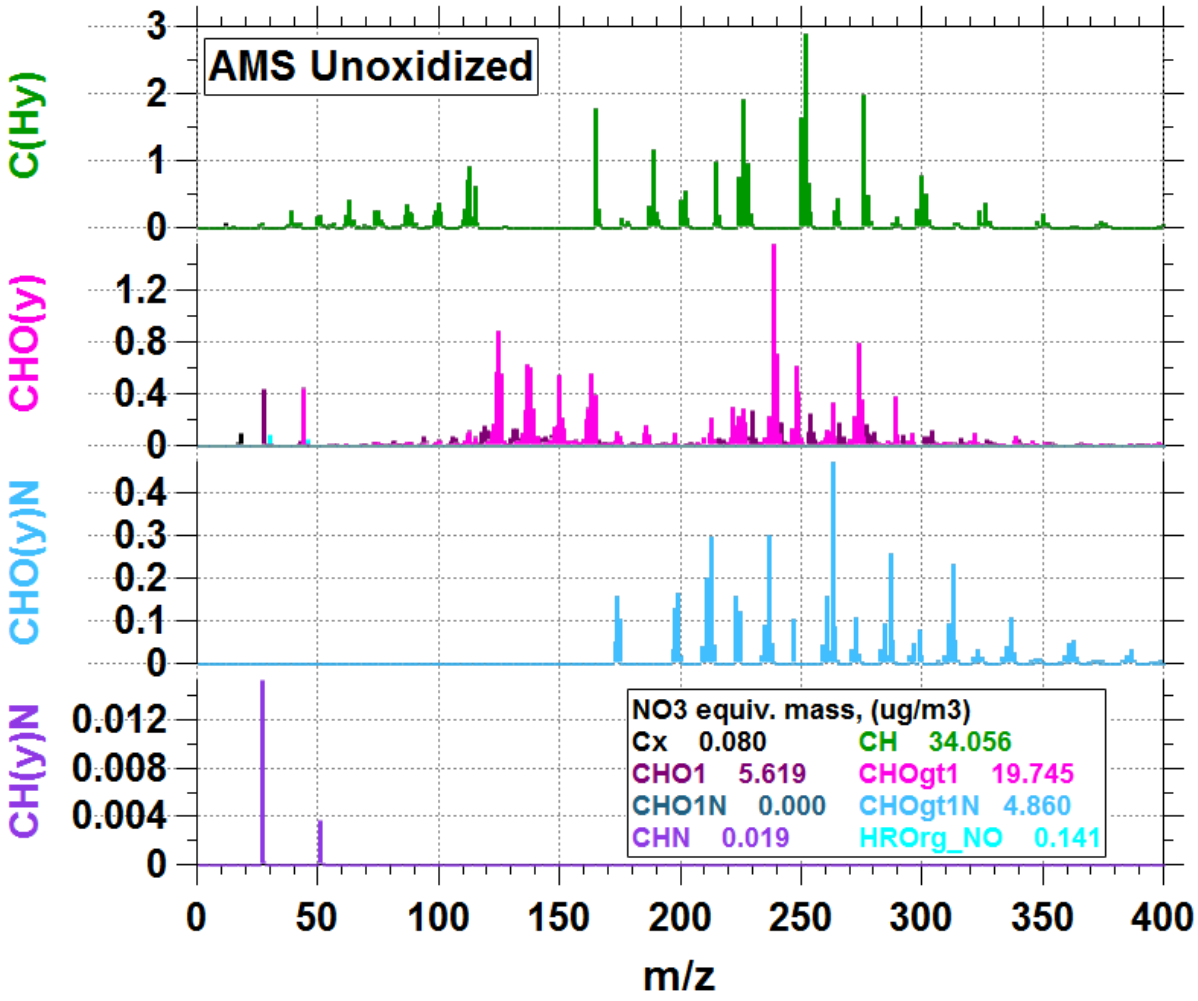


**Figure S3.3.** Expanded AMS HR spectrum of unoxidized light BrC that corresponds to the AMS HR spectrum shown in Figure 3.4a of the main paper.

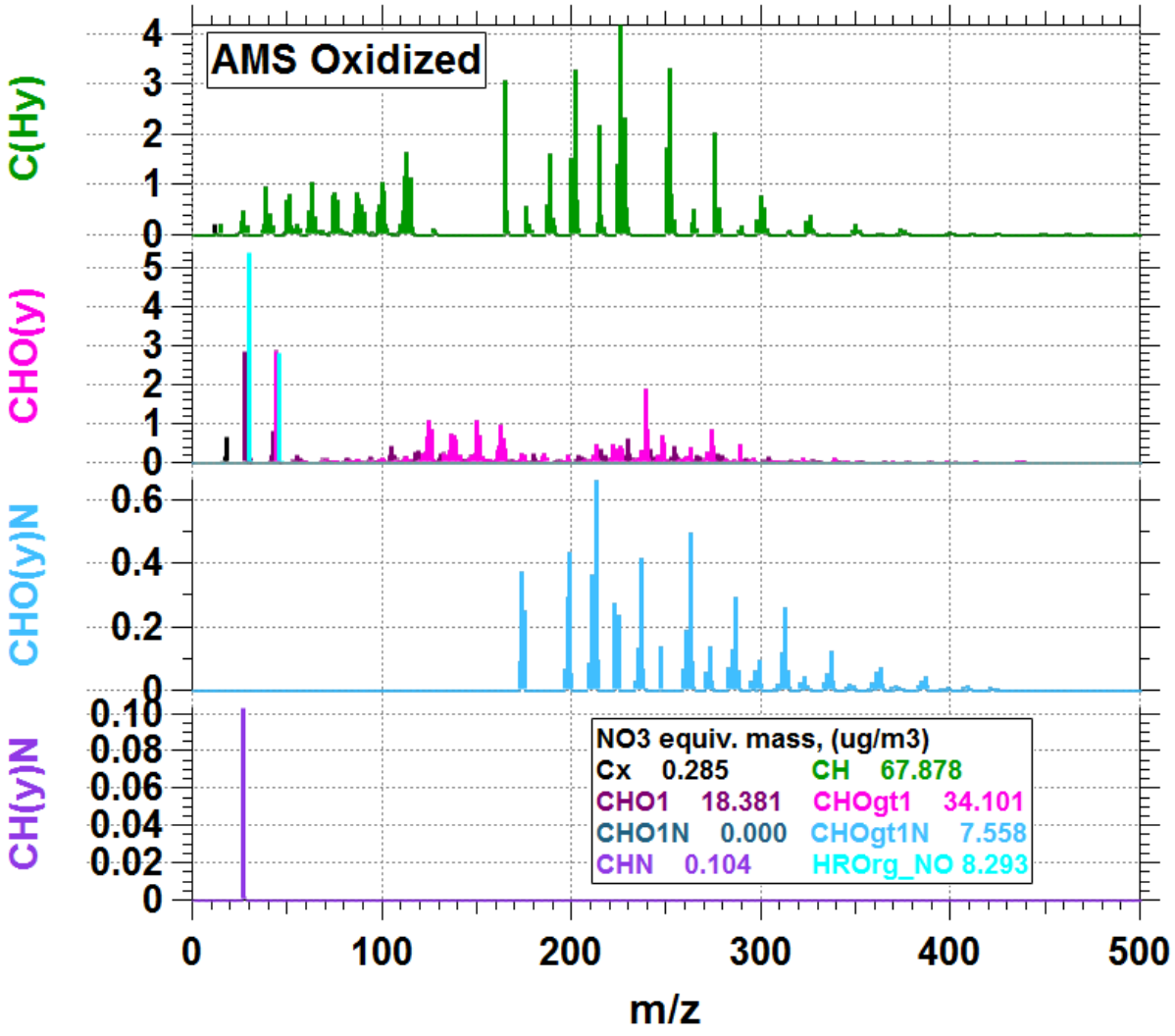


**Figure S3.4.** Expanded AMS HR spectrum of oxidized light BrC that corresponds to the AMS HR spectrum shown in Figure 3.4b of the main paper.

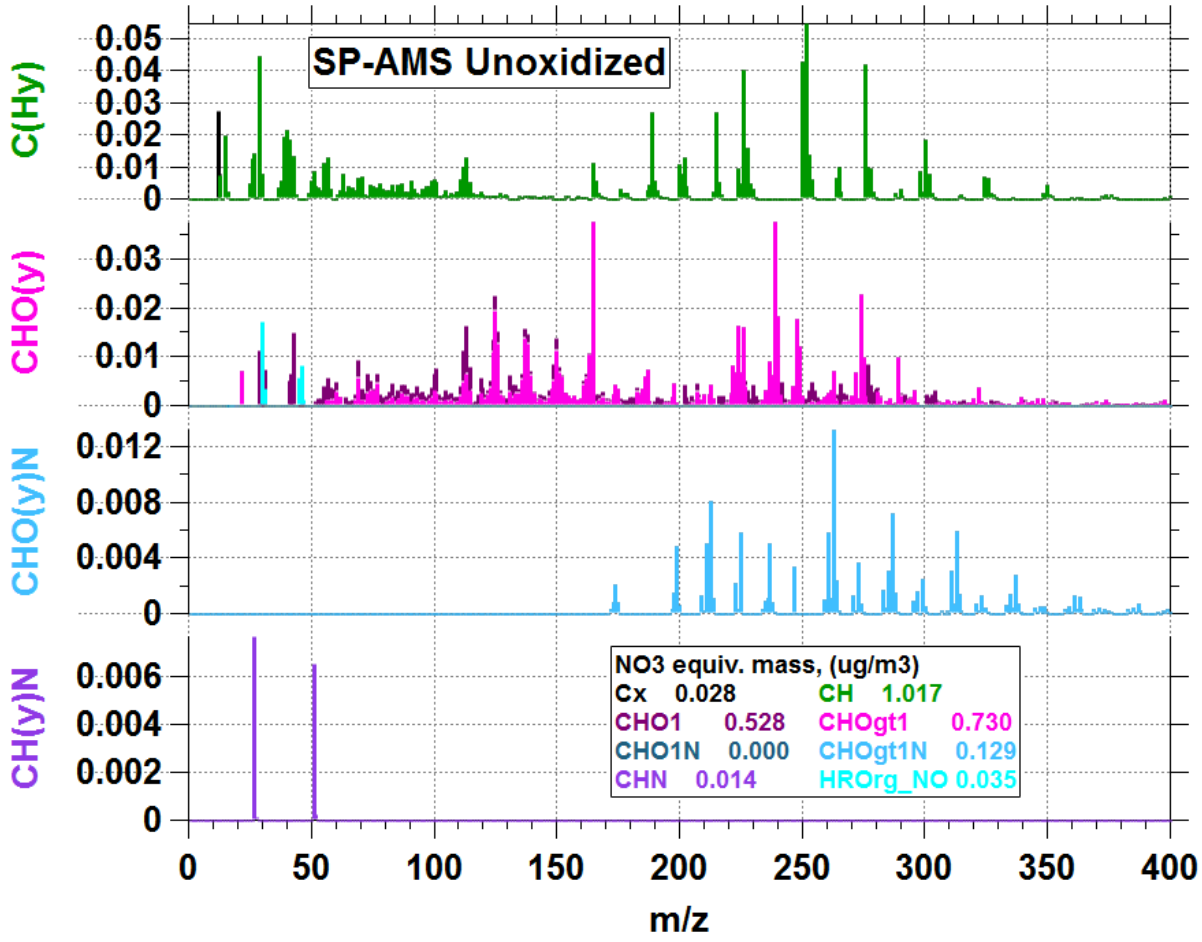


**Figure S3.5.** Expanded SP-AMS HR spectrum of unoxidized light BrC that corresponds to the SP-AMS HR spectrum shown in Figure 3.4c of the main paper.

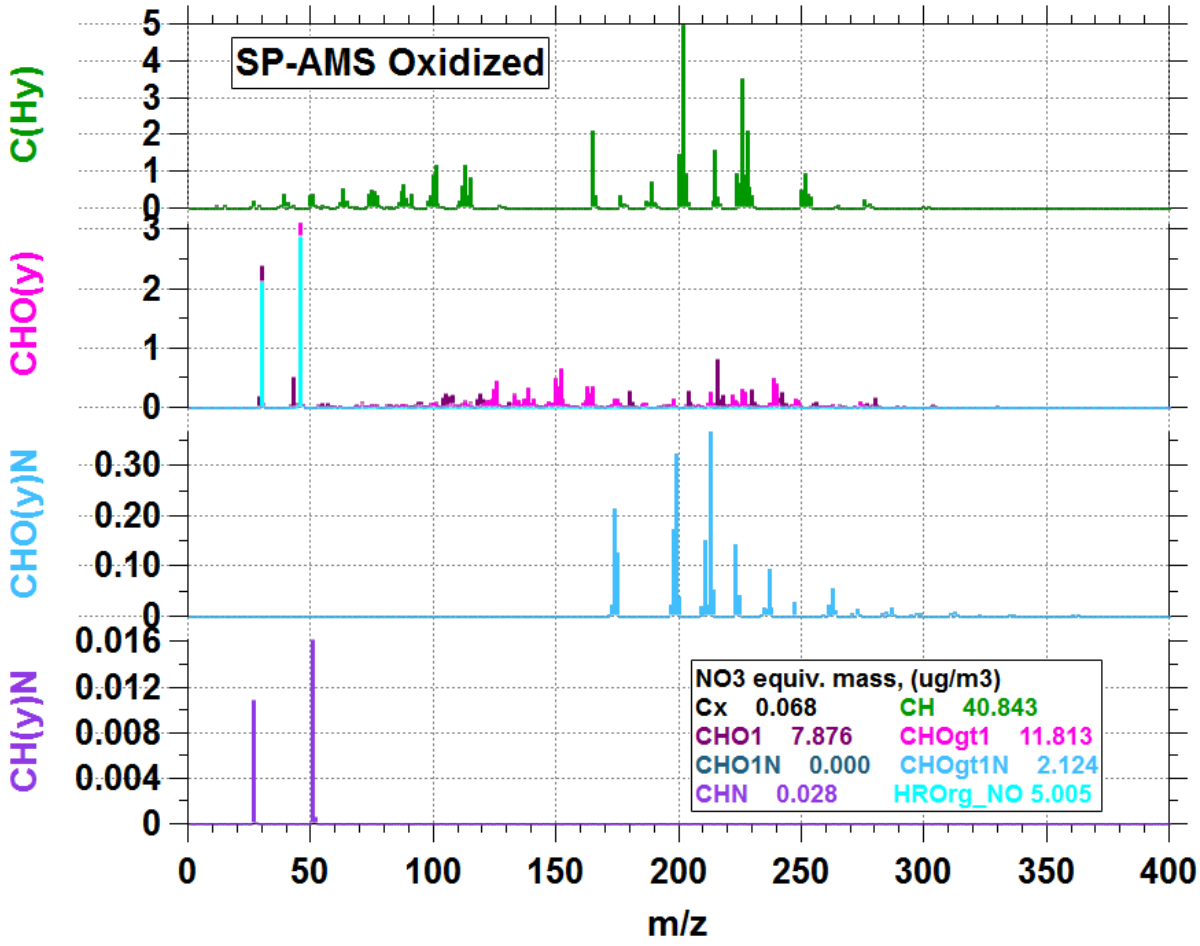


**Figure S3.6.** Expanded SP-AMS HR spectrum of oxidized light BrC that corresponds to the SP-AMS HR spectrum shown in Figure 3.4d of the main paper.

**References**

Aiken, A. C., P. F. Decarlo, and J. L. Jimenez. 2007. Elemental Analysis of Organic Species with Electron Ionization High-Resolution Mass Spectrometry. *Anal. Chem.* 79 (21): 8350–58. doi.org/10.1021/ac071150w.

Atkinson, R. 1991. Kinetics and Mechanisms of the Gas-Phase Reactions of the NO3 Radical with Organic Compounds. *J. Phys. Chem. Ref. Data 20*, 20 (3): 459–506. doi.org/10.1063/1.555887.

Canagaratna, M. R., J. L. Jimenez, J. H. Kroll, Q. Chen, S. H. Kessler, P. Massoli, L. H. Ruiz, et al. 2015. Elemental Ratio Measurements of Organic Compounds Using Aerosol Mass Spectrometry: Characterization, Improved Calibration, and Implications. *Atmos. Chem. Phys.* 15: 253–72. doi.org/10.5194/acp-15-253-2015.

D'Anna, B., Ø. Andresen, Z. Gefen, and C. J. Nielsen. 2001. Kinetic Study of OH and NO3 Radical Reactions with 14 Aliphatic Aldehydes. *Phys. Chem. Chem. Phys.* 3: 3057–63.

Krechmer, J., F. Lopez-hilfiker, A. Koss, M. Hutterli, C. Stoermer, B. Deming, J. Kimmel, et al. 2018. Evaluation of a New Reagent-Ion Source and Focusing Ion− Molecule Reactor for Use in Proton-Transfer-Reaction Mass Spectrometry. *Anal. Chem.* doi.org/10.1021/acs.analchem.8b02641.

# APPENDIX C

# SUPPLEMENTAL INFORMATION FOR CHAPTER 4

# DISCREPANCIES BETWEEN BRWON CARBON LIGHT-ABSORPTION PROPERTIES RETRIEVED USING ONLINE AND OFFLINE SOLVENT-EXTRACTION METHODS

**S4.1. Quantifying the bias in carbon mass concentration of DCM-extracted brown carbon:**

We performed blank experiments (n = 3) and control experiments (n = 10) to quantiafy the amount carbon extracted from the clean PTFE by DCM. In the blank experiments, we sonicated a piece of clean filter in 10 mL DCM for 20 minutes and measured the carbon mass concentration in the solution following the procedure in Section 4.2.3 in the main text. We measured $0.025 \pm 0.001$ g/l carbon in the DCM solution. In the control experiments, we collected 10 filters of BrC with variable light-absorptiob properties, each with a loading of ~0.25 mg. We then cut each filter into two approximately equal pieces and sonicated one piece in 10 ml DCM and the second piece in 10 ml DCM with an additional piece of clean filter. The carbon concentrations in solutions with additional piece of clean filter were $0.026 \pm 0.002$g/l larger than those with no additional filter. We concluded that DCM extracted approximately 0.026 g/l of organic carbon from the PTFE filter, and used this values to correct the concentrations of the DCM-extracted BrC.

**S4.2. Derivation of Equation (4.3) and Equation (4.4) in the main text**

Based on the Beer-Lambert Law:

$$I(\mathrm{x}) = I(0)\exp(-b_{\mathrm{V}}\,L) \tag{S4.1}$$

$$A = \log\left(\frac{I(0)}{I(\mathrm{x})}\right) \tag{S4.2}$$

Where $I$(x) is the intensity at position x on the leaser path, A is the absorbance measured by the UV-Vis spectrometer, L is the laser path length, and $b_V$ is the volume absorption coefficient of the material dissolved in the solution with a unit of $Mm^{-1}$. Therefore, we can rearrange Equation (S4.1) and substituted it into Equation (S4.2) and get:

$$b_V = \frac{A}{l} \ln(10) \quad \text{(S4.3)}$$

Then we can divide both sides by the mass concentration of the material dissolved in the solution ($C$, g cm$^{-3}$)

$$\frac{b_V}{C} = \frac{A}{l\,C} \ln(10) \quad \text{(S4.4)}$$

$b_V$ is given by:

$$b_V = \sigma\, N \quad \text{(S4.5)}$$

Where σ is the absorption cross-section (cm$^2$) of the material dissolved in the solution and $N$ is the molecular concentration of the material dissolved in the solution (molec. m$^{-3}$).

$C$ is given by:

$$C = \frac{N\ \mathrm{MW}}{N_A} \quad \text{(S4.6)}$$

Where MW is the molecular weight of the material dissolved in the solution and $N_A$ is Avogadro's number. we can substitute Equations (S4.5) and (S4.6) into Equation (S4.4) to obtain:

$$\frac{b_V}{C} = \frac{\sigma\, N}{N\ \mathrm{MW}/N_A} = \frac{\sigma\, N_A}{\mathrm{MW}} \quad \text{(S4.7)}$$

The absorption coefficient of the material dissolved in the solution ($\alpha$; cm$^{-1}$) is given by:

$$\alpha = \sigma\, \frac{n}{V}\, N_A \quad \text{(S4.8)}$$

Where $n$ is the number of moles of material dissolved in the solution, and $V$ is the volume of the solution. The density ($\rho$, g cm$^3$) of the dissolved material is given by:

$$\rho = MW\ \frac{n}{V} \tag{S4.9}$$

Substitute Equations (S4.7), (S4.8), and (S4.9) into Equation (S4.4), we get:

$$\frac{\alpha}{\rho} = \frac{\sigma\, \mathrm{N}_A}{\mathrm{MW}} = \ \frac{b_{\mathrm{V}}}{C} = \ \frac{A}{l\, C} \ln\,(10) \tag{S4.10}$$

**S4.3. Uncertainty analysis:**

Uncertainties of the carbon concentration measured by the OC-EC analyzer were calculated based on the manufacturer's specifications as:

$$m_{\mathrm{TC,unc}} = \pm(0.30\ \mu\mathrm{g} + 0.05\ m_{TC}) \tag{S4.11}$$

Where $m_{\mathrm{TC}}$ is the mass loading of TC put on the prebaked quartz filter.

The uncertainty of the aerosol mass concentration ($C_{\mathrm{BrC,\ unc}}$) was calculated as:

$$C_{\mathrm{BrC,unc}} = \ \frac{m_{\mathrm{TC,unc}}}{V} \tag{S4.12}$$

Where $V$ is the pipetted extracts volume.

The uncertainty in the imaginary part of the refractive index retrieved from UV-vis measurement ($k_{\mathrm{UV\text{-}vis,\ unc}}$) was calculated as:

$$k_{\mathrm{UV-vis,unc}} = \frac{\lambda\, \rho\, \ln 10}{4\pi} \sqrt{(A_{\mathrm{unc}}/A)^2 + (C_{\mathrm{BrC,unc}}/C_{\mathrm{BrC}})^2} \tag{S4.13}$$

Where $A$ is the absorbance of extracted BrC, $A_{unc}$ is the uncertainty of absorbance measurement reported from the manufacturer (=0.01), $C_{BrC}$ is the extracted BrC mass concentration, $\rho$ is the estimated density of extracted BrC, and $\lambda$ is the wavelength.

**Table S4.1. Summary of experimental data**

| **Toluene** | | | | | |
|---|---|---|---|---|---|
| Aerosol | Equivalence ratio | 1.3 | 2.5 | 1.1 | 2.2 |
| | $k_{422}$ | 0.200±5.2% | 0.204±10.1% | 0.097±11.3% | 0.042±7.2% |
| | $k_{532}$ | 0.086±7.7% | 0.072±17.8% | 0.026±11.8% | 0.005±7.5% |
| | $k_{550}$ | 0.077±7.8% | 0.055±7.0% | 0.022±11.8% | 0.004±7.5% |
| | $k_{782}$ | 0.037±13.5% | 0.021±35.3% | 0.003±23.0% | 0.0005±11.0% |
| | $w$ | 3.3±6.7% | 4.4±11.0% | 5.7±5.9% | 9.2±1.2% |
| DCM-extracts | $C$ (g $l^{-1}$) | 0.040±11.17% | 0.055±10.7% | 0.057±9.8% | 0.053±9.2% |
| | $k_{422}$ | 0.124±13.4% | 0.104±13.1 | 0.075±12.1% | 0.044±11.3% |
| | $k_{532}$ | 0.040±13.4% | 0.031±13.1% | 0.018±12.1% | 0.007±11.3% |
| | $k_{550}$ | 0.035±13.4% | 0.025±13.1% | 0.014±12.1% | 0.006±11.3% |
| | $k_{782}$ | 0.005±13.4% | 0.003±13.1% | 0.002±12.1% | 0.001±11.3% |
| | $w$ | 5.2±0.4% | 5.6±0.5% | 6.3±0.4% | 7.6±1.7% |

| | | | | | |
|---|---|---|---|---|---|
| Methanol-extracts | $C$ (g l$^{-1}$) | 0.034±10.3% | 0.041±9.3% | 0.030±10.0% | 0.060±8.8% |
| | $k_{422}$ | 0.082±10.3% | 0.084±9.3% | 0.075±10.0% | 0.036±8.8% |
| | $k_{532}$ | 0.016±10.3% | 0.012±9.3% | 0.009±10.0% | 0.003±8.8% |
| | $k_{550}$ | 0.012±10.3% | 0.009±9.4% | 0.006±10.0% | 0.002±8.8% |
| | $k_{782}$ | 0.001±10.3% | 0.001±9.3% | 0.001±10.0% | 0.001±8.8% |
| | $w$ | 7.3±0.7% | 8.4±0.7% | 9.3±0.8% | 10.9±0.6% |
| **Isooctane** | | | | | |
| Aerosol | Equivalence ratio | 4.6 | 3.5 | 3.5 | |
| | $k_{422}$ | 0.246±7.0% | 0.173±7.3% | 0.085±10.7% | |
| | $k_{532}$ | 0.110±12.2% | 0.046±9.4% | 0.014±19.1% | |
| | $k_{550}$ | 0.115±7.6% | 0.039±9.6% | 0.011±19.2% | |
| | $k_{782}$ | 0.041±17.4% | 0.014±18.2% | 0.002±70.4% | |
| | $w$ | 3.3±9.0% | 5.5±7.7% | 7.7±7.7% | |
| DCM-extracts | $C$ (g l$^{-1}$) | 0.050±11.2% | 0.059±6.6% | 0.071±6.5% | |
| | $k_{422}$ | 0.130±13.6% | 0.112±10.5% | 0.048±10.0% | |
| | $k_{532}$ | 0.051±13.6% | 0.023±10.5% | 0.007±10.0% | |

| | | | | |
|---|---|---|---|---|
| | $k_{550}$ | 0.043±13.6% | 0.018±10.5% | 0.006±10.0% |
| | $k_{782}$ | 0.005±13.6% | 0.002±10.5% | 0.001±10.0% |
| | $w$ | 4.9±1.1% | 7.2±1.8% | 8.3±1.9% |
| Methanol-extracts | $C$ (g $l^{-1}$) | 0.028±10.3% | 0.033±9.6% | 0.057±7.7% |
| | $k_{422}$ | 0.089±10.3% | 0.109±9.6% | 0.073±7.7% |
| | $k_{532}$ | 0.016±10.3% | 0.012±9.6% | 0.007±7.7% |
| | $k_{782}$ | 0.002±10.3% | 0.001±9.6% | 0.001±7.7% |
| | $w$ | 7.5±1.0% | 10.2±2.0% | 10.5±1.8% |
| **Cyclohexane** | | | | |
| Aerosol | Equivalence ratio | 3.3 | 3.3 | 3.3 |
| | $k_{423}$ | 0.240±12.6% | 0.145±11.2% | 0.124±14.6% |
| | $k_{532}$ | 0.101±13.6% | 0.048±17.7% | 0.025±17.6% |
| | $k_{550}$ | 0.096±9.0% | 0.042±12.1% | 0.020±17.7% |
| | $k_{782}$ | 0.037±23.9% | 0.026±19.9% | 0.003±41.8% |
| | $w$ | 3.5±12.4% | 4.2±12.5% | 6.9±5.3% |
| DCM-extracts | $C$ (g $l^{-1}$) | 0.040±7.8% | 0.059±6.6% | 0.077±6.1% |

| | | | | |
|---|---|---|---|---|
| | $k_{423}$ | 0.154±12.4% | 0.106±10.5% | 0.077±9.6% |
| | $k_{532}$ | 0.053±12.4% | 0.021±10.5% | 0.013±9.6% |
| | $k_{550}$ | 0.044±12.4% | 0.016±10.5% | 0.010±9.6% |
| | $k_{782}$ | 0.004±12.4% | 0.002±10.5% | 0.001±9.6% |
| | $w$ | 5.5±1.7% | 7.4±1.8% | 7.9±1.6% |
| Methanol-extracts | $C$ (g $l^{-1}$) | 0.024±11.2% | 0.046±8.3% | 0.056±7.7% |
| | $k_{423}$ | 0.141±11.2% | 0.094±8.3% | 0.084±7.7% |
| | $k_{532}$ | 0.025±11.2% | 0.012±8.3% | 0.009±7.7% |
| | $k_{550}$ | 0.019±11.2% | 0.008±8.3% | 0.007±7.2% |
| | $k_{782}$ | 0.001±11.2% | 0.002±8.3% | 0.001±7.7% |
| | $w$ | 7.7±2.0% | 9.3±1.9% | 9.6±1.7% |

**Table S4.2** Validation of the carbon mass concentration measurements (Section 4.2.4 in the main text) using pyrene solutions

| | expected concentration ($g\ l^{-1}$) | measured concentration ($g\ l^{-1}$) | % error |
|---|---|---|---|
| Methanol | 0.950 | 0.938 | 1.3 |
| | 0.059 | 0.056 | 5.1 |
| | 0.086 | 0.083 | 4.2 |
| DCM | 0.941 | 0.929 | 1.3 |
| | 0.059 | 0.055 | 6.6 |
| | 0.086 | 0.083 | 3.2 |